Probing Spin-Independent WIMP-Nucleon Interactions with the PANDAX-I Detector

by

Scott Stephenson

A dissertation submitted in partial fulfillment
of the requirements for the degree of
Doctor of Philosophy
(Physics)
in the University of Michigan
2015

Doctoral Committee:

Professor Wolfgang B. Lorenzon, Chair

Professor Gordon L. Kane

Assistant Professor Christopher J. Miller

Professor Aaron T. Pierce

Professor Gregory Tarle

© Scott Stephenson 2015

DEDICATION

to Dawn and Kerry.

ACKNOWLEDGMENT

I would like to recognize all of those who have contributed advice and encouragement throughout my time at Michigan. I especially thank my advisor Wolfgang Lorenzon and the additional members of my dissertation committee; Gregory Tarle, Aaron Pierce, Gordon Kane, and Christopher Miller. The direction and support given to me by Wolfgang has been key to shaping any success I have found. His example of integrity, leadership, and sense of humor will not be forgotten. Greg has been a wonderful complement in advising, whose playful outlook and quick switch to *serious mode* has influenced me greatly. The encouragement, inquiries on progress, and the occasional blackboard 'pressing' I received from Aaron, Gordy, and Chris were appreciated and helped propel me when I needed it. I am also deeply indebted to Michael Schubnell for the hours spent discussing computing, experiment design, troubleshooting various systems, and experiencing the interesting 'white spirits' in the Gulag with me. The memories of the slop bucket, ant wine, and sweltering underground heat will stay with us.

While in China I met people and experienced much that I will not forget. I benefitted greatly from the friendship, generosity, and scholarship of many other graduate students in the East. Fei, Andi, Mengjiao, Xiang, Qing, and Shaoli; your expertise aided my progress immensely. I hope we see a lot of each other in the future. Xun and Kirill were both excellent sources of knowledge and discussion. Kaixuan Ni, Jianglai Liu, and Xiang Liu; I owe a lot to seeing your vision and work ethic. Thank you for allowing me to lurk in your labs. I owe much to the PandaX PI, Professor Xiangdong Ji, for his confidence in our work and his willingness to take a chance when we needed it. Your support in China was greatly appreciated and thank you for heading the PandaX program. A list of projects I was involved in is provided in Appendix B, outlining in greater detail the effect you all had on the work I participated in.

At Michigan I also had the pleasure of working with numerous people directly on liquid xenon detectors. Curtis, Richard, Jon, and Monica; your technical expertise and advice was invaluable. I especially thank Curtis for his time spent working with me on the intricate details on MiX. Noah, Jonathan, Daran, and Mykola; I enjoyed the time with you and look forward to seeing amazing things. To Dan Levin, Tim Chupp, Tom Schwarz, Myron Campbell, and all of the other labs at UM from which I have *borrowed* items; thank you for the discussion and help with equipment, without which MiX would never have functioned. To my personal friends at Michigan who weren't already mentioned; Jack, Jon, Tom, Haolv, Xuefei, Lulu, Uttam, Yun, Rahul, Seckin; you made it worth getting to the department each day. Thank you.

There are many others at Michigan who were along for the graduate ride and contributed to my research. Without Josh and Adam, I would have never learned to program in any semblance to a proper way. I have always been amazed at your wizardry and appreciate the excellent examples you both set. Josh also was a great partner in crime and friend during the Dark Years of early graduate studies. I wish you luck in the Valley and hope to see you soon. Dan and Yuanyuan kept me company on frequent lab stints with endless and calculated conversation, respectively, on a litany of cosmological topics. Tomasz, my patient office mate, you always offered a calm, collected, conservative balance to my antics and proved your mastery of all things Pythonic time and again. I look forward to enjoying your company soon, but now with a noble element.

Bob Henson, you have been a great mentor. Your sense of humor, patience, perspective, and teaching prowess has affected me greatly. I owe a lot to your careful exposition and guidance while I was in Missouri. I hope our paths cross again soon.

Finally, I thank those who have personally affected me. My mother and father, I dedicate this work to you. Your love and understanding gave me the courage to pursue my endeavors. Lauren, your patience, love, and dedication was undeserved by me. I owe you and the Agne family so much. To family members and friends whom I did not mention, thank you for the love and support.

三人行，必有我师焉。

TABLE OF CONTENTS

LIST OF FIGURES

LIST OF TABLES

LIST OF APPENDICES

Abstract

Probing Spin-Independent WIMP-Nucleon Interactions with the PANDAX-I Detector

by Scott Stephenson

A dark matter relic density remaining from the Big Bang is believed to be permeating our Universe in the form of dark matter particles. It is likely that these relics could be detected in Earth-based experiments, prompting a prolonged search effort by experimental groups looking for the mysterious particle. Recent dark matter searches have received much attention due to several possible positive direct detection results [1–8], with reports putting the dark matter mass near 10 GeV/c^2. This has motivated other direct detection experiments to focus their efforts in the low mass region, which has resulted in several competing null results [9–13].

The PandaX-I detector, located at China JinPing Laboratory in Sichuan Province, China, is a dual-phase liquid xenon time projection chamber with three-dimensional position reconstruction capabilities. The high light yield design allows for a low energy threshold and sizable xenon mass, targeting the low mass WIMP-nucleon cross-section region of parameter space. The detector was designed, constructed, and operated by the international Particle and Astrophysical Xenon (PandaX) collaboration with the goal of probing the alluring low WIMP mass cross-section parameter space.

This dissertation outlines the operation of the deep underground, low background PandaX-I detector utilized for a rare event dark matter search. I discuss dark matter interaction rates in terrestrial detectors and the properties of liquid xenon as a suitable dark matter target. A detailed discussion of the dark matter WIMP search with liquid xenon based

detectors is given, including the design, background simulation, construction and operation of the MiX (Michigan Xenon) development detector and the large scale PandaX-I (Particle and Astrophysical Xenon) detector. Finally, I discuss the outcome resulting from a dark matter search analysis of the first 17.4 live-days in the PandaX-I 37 kg fiducial volume [13]. With this effort, the PandaX collaboration provided a deep probe of the low WIMP mass parameter space, excluding the aforementioned low mass dark matter signal reports.

CHAPTER I

Introduction

Much evidence has amassed on the existence of a new component of matter in our universe, termed dark matter (DM). Tests put stringent limits for the known particles of the Standard Model of particle physics, so the dark matter that we view through astronomical means must be made of yet unknown particles [14,15]. If we hope to determine the fundamental nature of the DM, we must first observe its properties with sensitive particle detectors. The push for observation of the dark matter is at a mature stage where large regions of model parameter space are being probed by a multitude of collaborations [1–10, 12, 13, 16, 17]. In this thesis we discuss the first results of the PandaX-I dark matter detector.

1.1 Dark Matter

There are many lines of evidence which all point to a significant nonbaryonic matter component [14] in the universe which may be detectable. With this in mind, a brief standard story of dark matter is worth stating. The big bang leaves behind several relics such as protons, electrons, photons, light nuclei, but also dark matter. As time moves on, the dark matter clumps gravitationally to form large scale structure, which in turn seeds galaxy formation in the universe. We now live in a typical galaxy with a presumably typical abundance of dark matter that permeates our Solar System. Our location in this dark matter halo suggests that the Earth would have many dark matter particles O($10^5/cm^2$) passing through it each second. This leaves the opportunity for Earth-based detection. Several models exist which

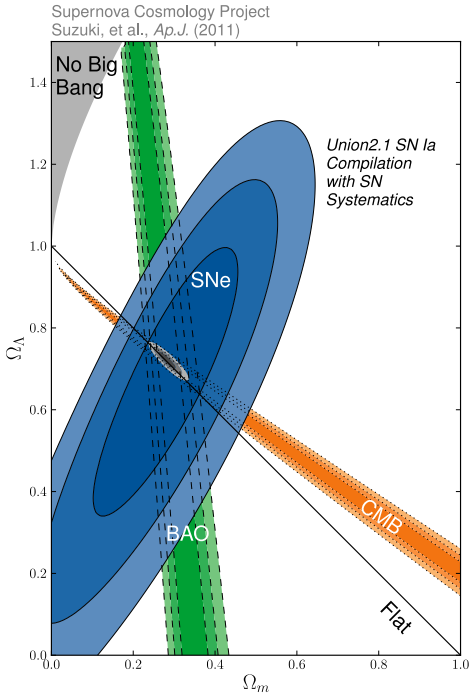

Figure 1.1.1: Concordance between many measurements is the signature of the ΛCDM model. Shown is the remarkable agreement between baryon acoustic oscillation, cosmic microwave background, and supernova measurements compiled by the Supernova Cosmology Project [18].

could explain the dark matter but the best motivated of them provides a weakly interacting massive particle (WIMP) as the dark matter, generated through the supersymmetry (SUSY) extension to the particle Standard Model.

1.1.1 Evidence

The first hints of dark matter were seen through astronomical observations of galaxy clusters [19]. Further supporting evidence was found through the observation of anomalous rotation curves of galaxies [20,21], large scale structure [22], the cosmic microwave background angular power spectrum [23–25], gravitational lensing [15, 26], the existence of dwarf galaxies [15], etc. The Universe is strongly constrained to be geometrically flat with energy densities relative to critical of 4.5% baryons, 26.5% cold dark matter, and 69% dark energy [18] (see

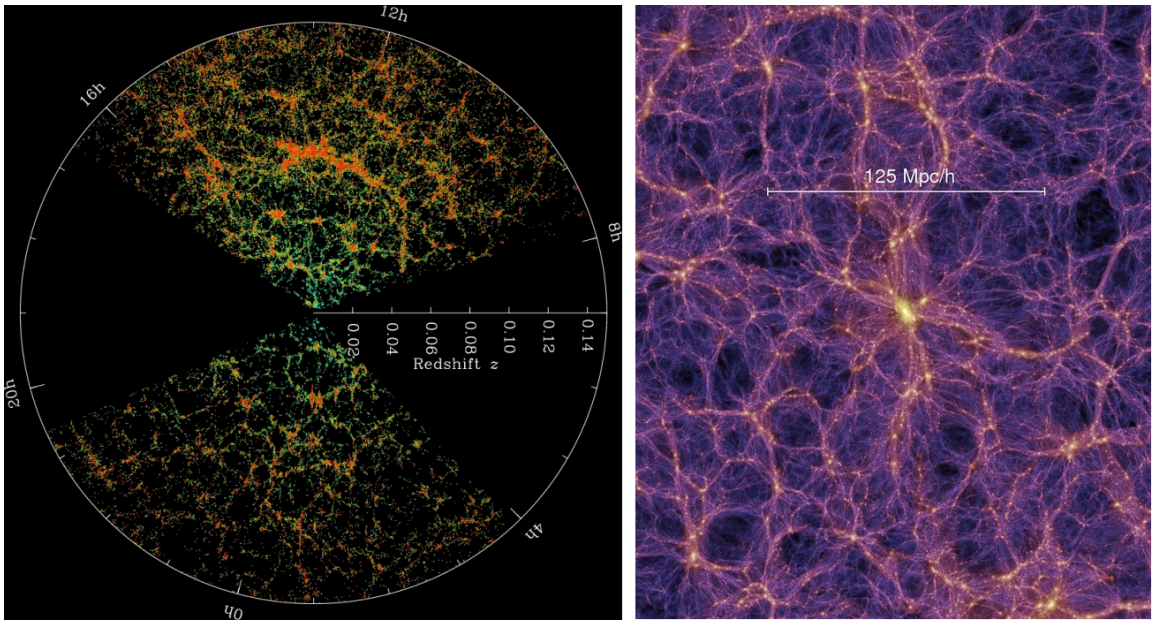

Figure 1.1.2: Left: Large scale structure is observed by sky surveys like the Sloan Digital Sky Survey [22]. Right: Simulation of dark matter gravitational evolution by the Millennium Simulation [27]. Remarkable agreement between simulation and observation strengthens the case for cold dark matter.

e.g. Fig. 1.1.1).

The standard concordance model of cosmology, lambda cold dark matter (ΛCDM), is consistent with a host of astronomical observations. The model is described by only six parameters: energy density of cold dark matter relative to critical Ω_c, energy density of baryons relative to critical Ω_b, current rate of expansion H_0, amplitude of primordial scalar fluctuations A_s, scalar index n_s, and optical depth at reionization τ. The model makes precise predictions which have had much success when observationally tested, making ΛCDM a foundation of modern cosmology.

1.1.1.1 Large Scale Structure

The well established ΛCDM model [28] accurately describes the evolution of the universe as it expands and cools. The first structures to form in the universe were seeded by density perturbations generated during inflation that grew via gravitational attraction. This collection

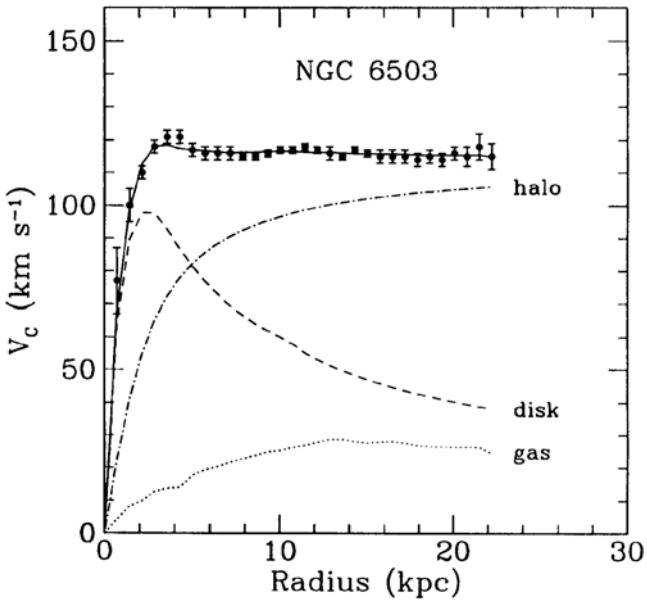

Figure 1.1.3: The galactic rotation curve for NGC 6503 [21] is shown. Velocity measured by the redshift of the 21 cm hydrogen line is shown in black circles with a solid curve fit. The contributing mass components are shown in dashed (disk), dotted (gas), and dash-dot (halo) curves. In order to produce the flat rotation curve at large radius, there must be an unseen dark component.

of 100 Mpc scale filaments, nodes, and voids forms the large scale structure (LSS) observed in the universe. The Sloan Digital Sky Survey (SDSS) in particular mapped a significant portion of the local large scale structure [22]. The Millennium Simulation performed a large scale computational effort to simulate the dark matter collapse into LSS at large scales [27] with marked qualitative and quantitative agreement with data as shown in Fig. 1.1.2. It is clear that without dark matter, the scale and shape of the structure in our universe would be unmistakably different due to its structure-preserving, cold nature.

1.1.1.2 Clusters and Galaxies

In 1933, Fritz Zwicky noted the incongruence between the velocity distribution of the Coma galaxy cluster and the visible matter it contained [19]. Using the virial theorem, there was far too much kinetic energy in the cluster system to be held together gravitationally by visible mass alone. Zwicky hypothesized that a nonluminuous matter component must be

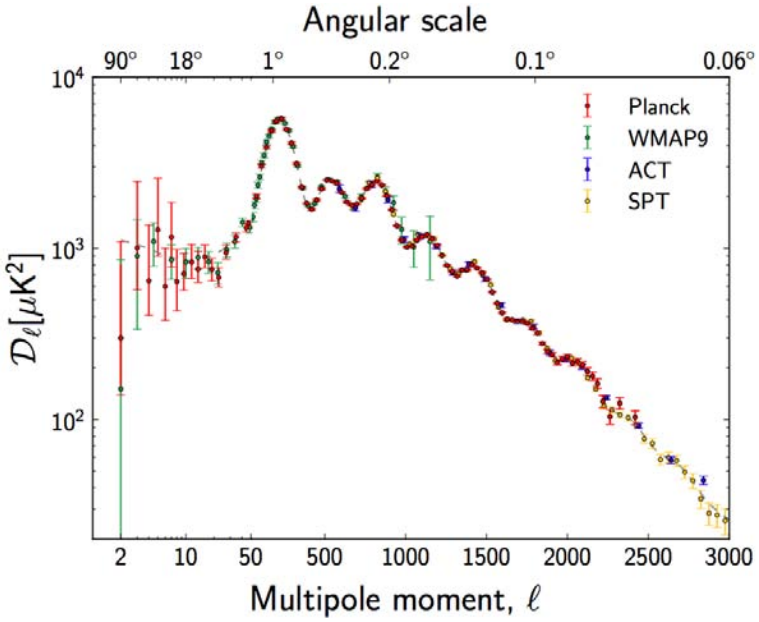

Figure 1.1.4: The angular power spectrum for the CMB, as measured by Planck. Included are the results of WMAP9 [24, 25], ACT [30], SPT [31]. A dashed grey line shows the ΛCDM power spectrum that corresponds to $\Omega_c = 0.265$, $\Omega_b = 0.045$, and $\Omega_\Lambda = 0.69$, showing remarkable agreement with the data. Figure from Ref. [23].

present to provide the potential well holding the galaxy cluster together.

Additional evidence for dark matter is seen in the velocity curves of rotating galaxies. The velocities of stars in a galactic disc follow the classical Newtonian dynamics equation $v(r) = \sqrt{GM(r)/r}$. Galactic rotation curves plot the speed of stars orbiting a galaxy's core as a function of radius but, as first seen in the NGC 6503 galaxy [20], the behavior does not follow the expected decaying curve that would be caused by luminous matter alone (see Fig. 1.1.3). The flat rotation curve suggests that $M(r) \propto r$ throughout the disk, and even at radii larger than the galactic disk the mass contained within a sphere of radius r continues to increase linearly [29], suggesting that the dark component continues well past the disk.

1.1.1.3 Cosmic Microwave Background

Striking signatures of dark matter are found in the cosmic microwave background (CMB) as well. High precision measurements have been conducted in the past couple decades which

Figure 1.1.5: Image of large bodies of dark matter lensing the background through strong gravitational lensing. This body is Abell1689, showing the classic signs of a large lens. The image of background galaxies are remarkably stretched and distorted, with multiple images emerging in some cases. Image from Ref. [32].

map the surface of last photon scattering at redshift $z \approx 1090$. The CMB has been thoroughly redshifted by the time it gets to us, sitting at 2.73 K with variation of the CMB across the sky on the 10 μK level. The anisotropies in the CMB are an image of structure formation in the early universe. Through statistical methods, a large amount of information can be gathered from the CMB and interpreted in terms of the ΛCDM model and the energy budget of the universe. The positions and relative heights of the baryon acoustic peaks in the CMB power spectrum inform us about the overall curvature of space, the amount of matter, and the fraction that is baryonic. Current measurements of the angular power spectrum of the CMB agree well with ΛCDM (see e.g. the Planck results [23] in Fig. 1.1.4).

1.1.1.4 Gravitational Lensing

Astronomers have found further evidence for dark matter while peering into deep space with highly sensitive telescopes. Many objects in the sky have been identified that pro-

Figure 1.1.6: Image of the famous Bullet Cluster is shown. The false color blue denotes the population of dark matter as garnered through weak lensing measurements. The pink is a false color x-ray overlay which shows the gas content. Two large bodies are believed to have collided with the dark matter passing through unhindered and the gas slowed considerably. Image from Ref. [33].

duce gravitational lensing effects. The observations capture warped images caused by large, transparent, non-luminous, and non-baryonic clumps of matter in the universe that lens background galaxies. The signatures of strong gravitational lensing appear as large arcs and double images, as seen in Fig. 1.1.5. When the position (redshift) of the strong lens is known, the mass of the lensing matter can be estimated and compared with the luminous component, showing a large mass ratio for dark-to-light components of O(10-100×) for typical objects [15].

Weak lensing is less dramatic when compared with the highly warped images produced by strong lensing. Nonetheless, it has proved itself to be an extremely valuable tool for probing dark matter properties on cosmological scales. In the weak lensing case, the background galaxies are only slightly distorted, but when analyzed statistically the correlated distortions yield the mass distribution between the observer and the background. This is the method used to reconstruct the dark matter mass distribution in the famous Bullet Cluster [26, 33]

(see Fig. 1.1.6). The Bullet Cluster is believed to show the result of two galaxy clusters colliding, with the point-like galaxies and DM matter portion of one cluster passing unhindered through the other cluster but the gas portion colliding and lagging behind. The noninteracting behavior of the cluster's largest matter component is consistent with weakly interacting dark matter.

1.2 Dark Matter Candidates

Structure formation data limits the allowable particle properties for dark matter, but still leaves freedom for the details of the exact particle model [15]. It is clear that the dark matter cannot be a Standard Model (SM) particle since only neutrinos could possibly fill the void, but they have been ruled out as plausible candidates [24]. It is thought that after the big bang the universe expanded, cooled, and eventually dark matter particle interactions began to freeze out [34], leaving the DM relic density that we see today. The front running extensions to the Standard Model which could explain dark matter are generally motivated by other areas of particle physics as well. The weakly interacting massive particles have a footing in solving the hierarchy problem and gauge unification coupling if the WIMP is a SUSY particle. Additionally, the dark matter could be explained by a nonthermal relic which was introduced to solve the SM strong CP problem, the axion. Further possible models exist, albeit arguably less motivated, but could account for the DM particle abundance as well [15]. We focus first on axions and ultimately the WIMP paradigm.

1.2.1 Axions

The strong CP problem asks the question of why CP-violation has not been observed, even though it is predicted with quantum chromodynamics. A solution of this problem suggests a global symmetry which, upon breaking, generates a new low mass particle termed the axion. This Peccei-Quinn mechanism produces a pseudoscalar which could have been produced in the early universe in large quantities to make up the DM relic density [35]. The axion could be detected by axion to photon conversion in a strong magnetic field using very large, high Q resonant cavities. Experiments have been constructed and operated at cryogenic

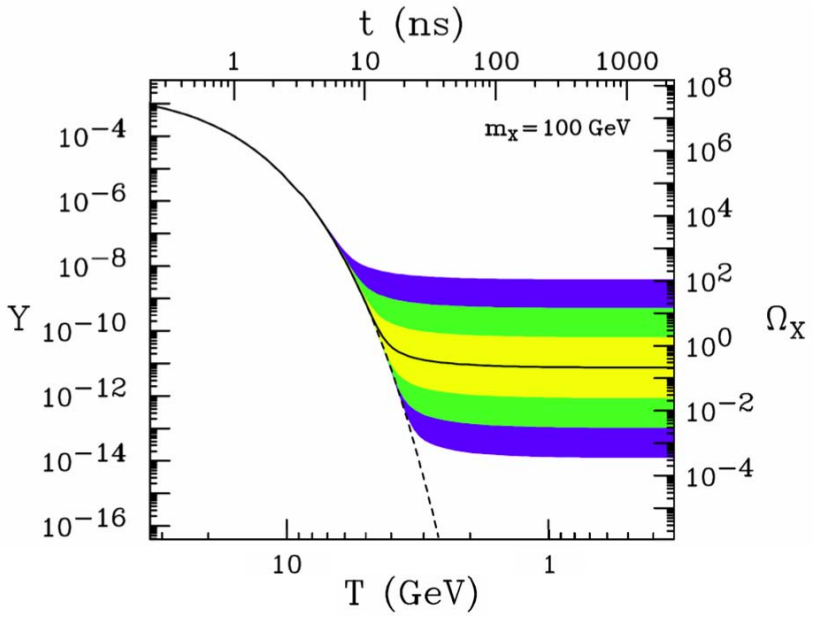

Figure 1.2.1: During the early universe dark matter particle are thought to have been in thermal equilibrium in the cosmic soup. After the universe cools, thermal freeze out of dark matter interactions happen, as depicted in this figure. A thermally averaged cross-section around the weak scale (around 10^{-36} cm^3/s, with cross-section varied by decade to produce the colored bands) will leave behind a relic density commensurate with the observed dark matter density, known as the WIMP miracle. Figure from Ref. [36].

temperatures to scan photon frequency space in search of the axion to photon conversion effect. The leading effort in the axion search is ADMX, a resonant cavity with the ability to search for axions with masses of O(10 μeV/c^2) [16].

1.2.2 WIMPs

The WIMP miracle is so named because a particle with mass and interaction cross-section near the weak scale (i.e. a detectable scale) makes a very good dark matter candidate, due to it supplying the observed relic density within our universe (see Fig. 1.2.1) . A prediction of the WIMP relic density is shown in Ref. [34] to be

$$\Omega_\chi h^2 = \frac{10^{-37} cm^2 c}{\langle \sigma_\chi v \rangle}.$$

It also happens to be that theorists have plausible theories which predict weak scale massive particles that fit the WIMP scheme. Supersymmetry is a typical extension to the Standard Model which provides these WIMP candidates for the dark matter. Additionally, SUSY has long been a favorite extension due to its ability to unify gauge couplings near the Planck scale and to solve the hierarchy problem in particle physics [34].

A typical candidate which arises from the Minimal Supersymmetric Standard Model (MSSM) is the lightest supersymmetric partner (LSP). The LSP is forbidden to decay to the SM sector via an R-parity symmetry [34] and usually sits around 10 to 1000 GeV/c^2 in mass, with a typical cross-section of 10^{-33} to 10^{-47} cm^2. The LSP is generally a neutralino χ, a linear combination of superpartner photino ($\tilde{\gamma}$), zino ($\tilde{Z}$), and neutral Higgsino ($\tilde{H}_1^0$, $\tilde{H}_2^0$) fields [34, 37], written as

$$\chi = N_1\tilde{\gamma} + N_2\tilde{Z} + N_3\tilde{H}_1^0 + N_4\tilde{H}_2^0.$$

The photino, zino, and neutral Higgsinos are fermion superpartners to the Standard Model photon, Z, and Higgs boson. WIMPs of this nature typically interact with standard atomic nuclei through weak scale interactions, either with the target nucleus spin or nucleon count [34, 38]. These interactions with standard matter are the basis for direct detection of MSSM DM candidates.

The MSSM parameter space is typically too large to probe directly through contemporary computational means. Accordingly, the parameter space must be reduced to representative model subsets which provide predictions for cross-section and mass of the neutralino. The Constrained MSSM (CMSSM), Next-to-Minimal Supersymmetric Standard Model (NMSSM), and phenomenological MSSM (pMSSM) [39–41] are subsets of the MSSM which combine parameters (e.g. unification at high energy scales) to provide representative predictions in the WIMP mass-cross section plane. These models produce a spectrum of dark matter masses and cross-sections as can be seen in Fig. 1.2.2. Current direct detection experiments already partially probe both the predicted SI and SD cross-sections across a wide mass range [42, 43] and continue to extend detector sensitivities.

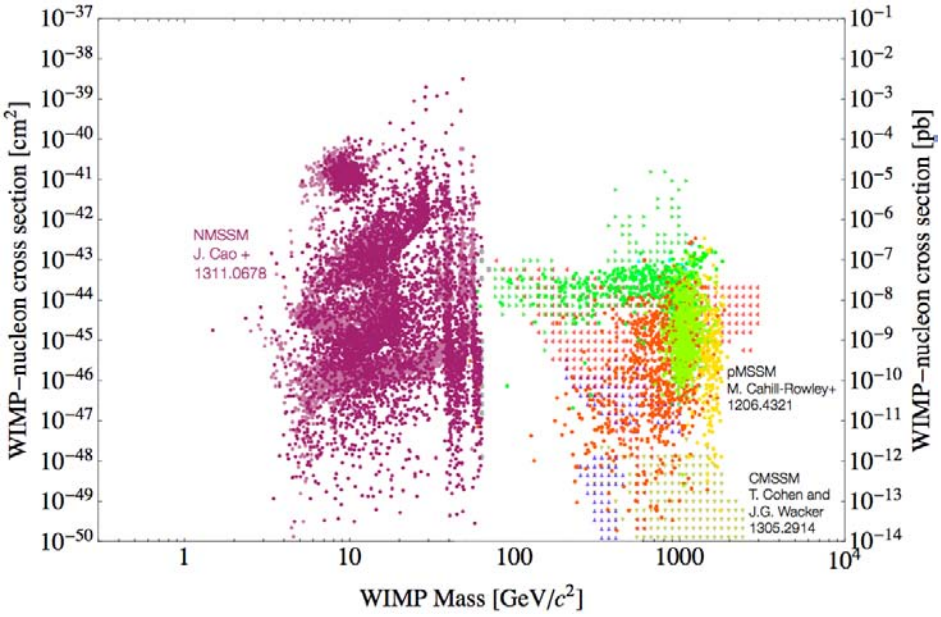

Figure 1.2.2: Grid points on the WIMP-nucleon cross-section versus WIMP mass plane from MSSM parameter subset scans. The Constrained MSSM (CMSSM), Next-to-Minimal Supersymmetric Standard Model (NMSSM), and phenomenological MSSM (pMSSM) points represented here form viable candidates for DM, consistent with a number of constraints [39–41]. Figure from Ref. [42].

1.3 WIMP Detection

The DM relic particles left over from the big bang are scattered throughout the universe, forming the large scale structure and seeding galactic formation. The Earth sits in a galaxy which is permeated with the relic particles that form the Milky Way's dark matter halo. The Earth's location in the universe (and the existence of suitable target materials on the Earth) allows experimenters to construct an experiment which could directly sense interactions with WIMPs. The general detection scheme has common characteristics across detection technologies that do not rely heavily on the chosen target material.

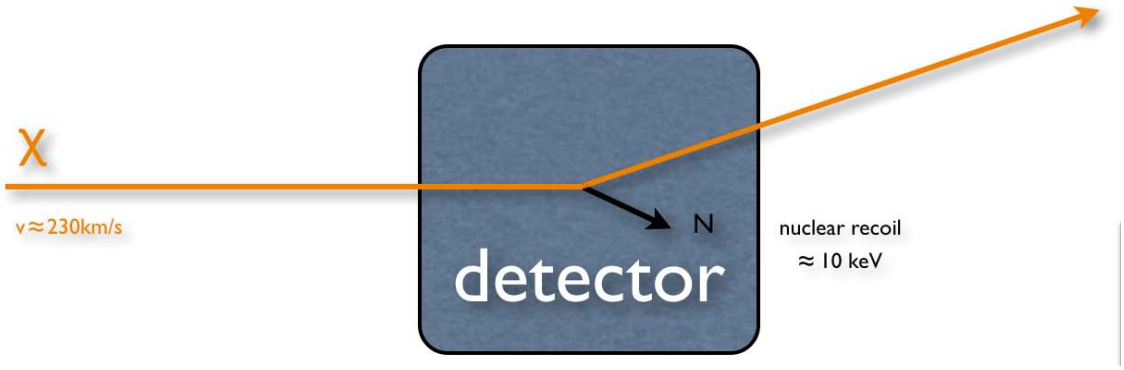

Figure 1.3.1: A schematic of a typical WIMP-nucleus interaction. The WIMP enters the detector with a typical velocity of 230 km/s and scatters upon a target nucleus, causing it to recoil with energy of a few keV. The WIMP continues on as the nucleus deposits the recoil energy into the detector over a short track.

1.3.1 Direct Detection General Characteristics

In general, research necessarily sits at the edge of what is discoverable - i.e. if we had more capability we would have extended the edge, by definition. This means the current lack of a direct discovery of particle dark matter has scientists building ever bigger, better, and more sensitive experiments. In contrast to the particle collider experiments which push high energy capabilities, the search for dark matter forces the construction of highly sensitive experiments in search of rare events in the low energy regime. The DM experiments nominally have a few qualities in common. It is usually necessary to locate the experiment deep underground to avoid cosmic radiation near the Earth's surface. Similarly, it is required to have low radioactivity materials, good background rejection capabilities, a low energy threshold, and to build the experiment with a large target volume.

The experiments also consider the ability for the WIMP to couple to nuclear spin or nucleon count, called spin-dependent (SD) and spin-independent (SI), respectively. The details of the standard interaction models like the A^2 enhancement and form factor suppression of the spin-independent cross-section and the effect on detection rates are detailed in Ch. 2. Specific target materials will usually have differing affinity for SI and SD interactions which drives the target's use in varied scenarios.

1.3.1.1 Underground

Dark matter hunters are pushed underground due to the very high sensitivities of dark matter detectors achieved today. If a detector were to sit at the Earth's surface, the event rate from background cosmogenic radiation would completely drown out any novel signals that could be hoped for. Typical depths for a contemporary experiment are in the one to two mile deep range, where deeper is exponentially better.

1.3.1.2 Low Radioactivity

Nearly all macroscopically sized substances that can be used to construct a dark matter detector are radioactive. They can contain trace radioactive isotopes from other elements, be activated by radioactivity during construction, or the element itself can have radioisotopes. This is unavoidable but can be minimized to impressive levels through careful material selection efforts. Detectors are constructed of highly purified low radioactivity target material, sensors and wiring, and mechanical structures. High purity copper is a mainstay construction material along with virgin teflon, high purity crystals, and carefully constructed photomultiplier tubes and other readout sensors. Once the detectors are built, they must be surrounded by a low radioactivity shield to block activity from normal everyday sources, then ultimately placed in a deep underground lab.

1.3.1.3 Background Rejection

After careful precautions have been taken to reduce background within a detector, there is still the opportunity for undesired particle interaction events to happen in the target volume. Most detectors are designed to handle this leftover background by using a signal discrimination procedure. Often the background signals will be electromagnetic in nature and produce a different signal response in the detector when compared to a DM-like signal, either in signal size or deposition structure. Additionally, a time discrimination technique may be used where an experiment is run for an extended period of time looking for signal modulation due to varying dark matter interaction rates with a known background.

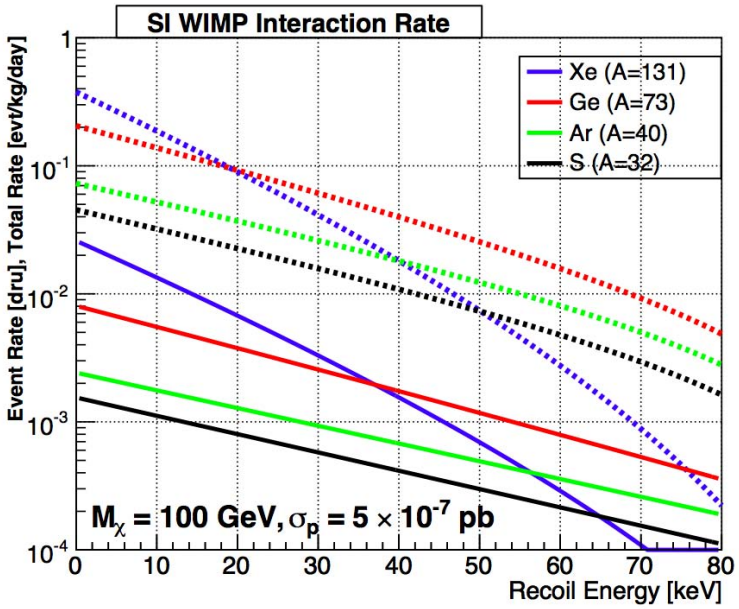

Figure 1.3.2: The differential recoil spectrum (solid) and the integrated recoil spectrum (dashed) for a WIMP with $m_\chi = 100$ GeV and cross-section of 5×10^{-43} cm^2. The integrated spectrum curve shows all events which occur above the specified energy. Figure from Ref. [44].

1.3.1.4 Low Threshold

The energy spectrum for a typical recoiling target nucleus due to a collision with a dark matter particle is near that of a falling exponential.]Since the collision speeds are small O(10^{-3}c), The WIMP-nucleus interaction can be treated as an elastic billiard ball collision with a momentum transfer dependence at relevant energies (as detailed in Ch. 2). That is to say, dark matter events depositing only a small amount of energy in the detector are overwhelmingly more numerous (see Fig. 1.3.2). The abundance of low energy events O(keV), with the promise of higher event rates, forces experimenters into the hunt for an ever lower detector energy threshold.

1.3.1.5 Large Target Mass

The weakly interacting nature of dark matter interactions means that there is no shielding effect in a detector target (the interactions are so infrequent that the detector material will

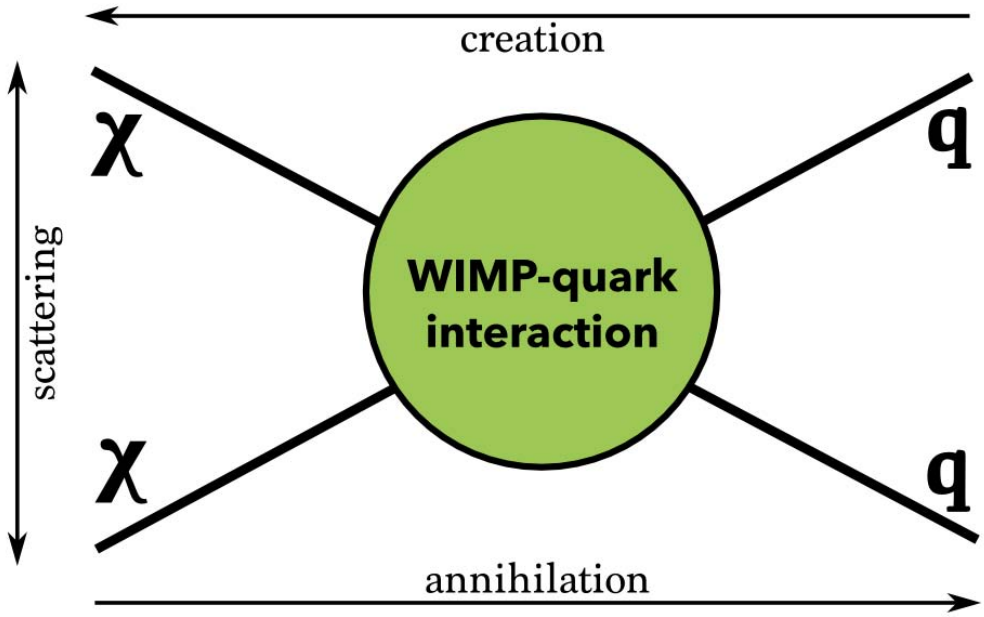

Figure 1.3.3: An effective interaction vertex is shown for a WIMP (χ) and Standard Model particle (q). The time ordering of the interaction determines whether it is an WIMP annihilation, creation, or scatter. The respective detection methods probing the orderings are indirect, collider, and direct efforts.

not block the opportunity for scatters deeper in the target). This means the interaction rate for dark matter with a target nucleus is proportional to the number of target nuclei within the detector, i.e. the target's total mass. Since models predict a small WIMP-nucleus interaction cross-section (and dark matter searches have yet to observe a convincing signal), the experiments have been pushed from sub-gram to ton scale in the past few decades [43].

1.3.2 Current Particle Detection Status

Detection of the WIMP scattering cross-section can be achieved through various detection schemes. A Feynman diagram of a DM-quark interaction is depicted in Fig. 1.3.3 showing the various time orderings which can be considered. If one considers the particles moving vertically in the diagram then it is DM-quark scattering. This is the mode that is exploited in direct detection efforts. If time moves rightward, the case of DM self-annihilation shows itself, leading to indirect detection techniques that search for the standard model offspring

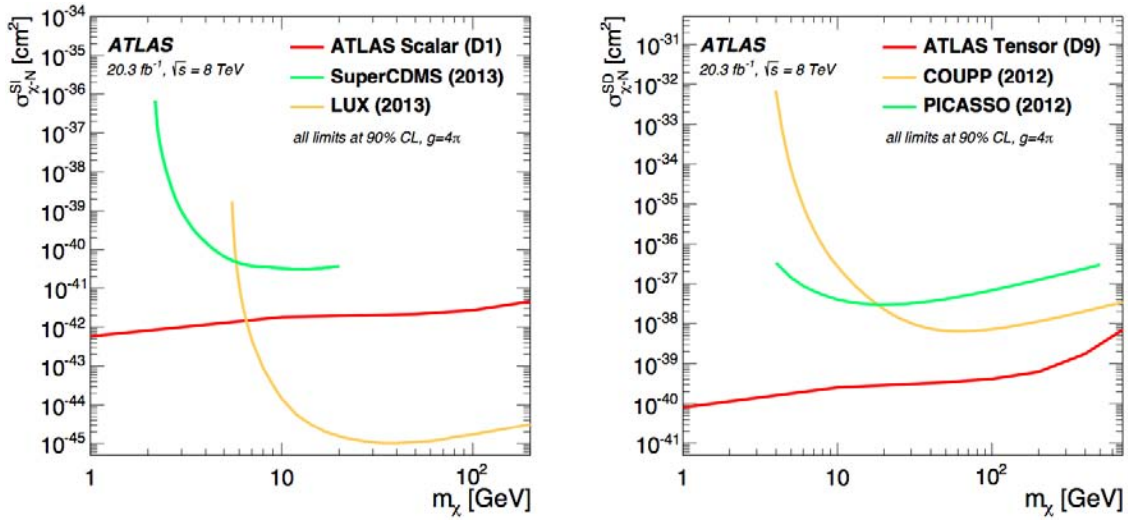

Figure 1.3.4: Left: The spin-independent cross-section result from the ATLAS missing transverse momentum search is shown. Right: The spin-dependent results are shown [45]. Colliders are particularly sensitive to low mass dark matter (since you must have enough energy to create the two WIMPs), but care must be taken to compare the results with direct detection efforts, as noted in Refs. [46, 47].

of the interaction. If time moves leftward, the standard model particles annihilate and produce dark matter particles. This is the favored mode of detection being studied with colliders through a missing energy signature. A summary follows of using colliders, indirect detection, and direct detection to probe the WIMP-SM cross-section.

1.3.2.1 Colliders

Colliders tend to have strong high energy spin-dependent cross-section probing capabilities, but the interpretation of the various effective field theory operators in the very low energy regime (where direct detection takes place) remains to be settled. Spin-independent and spin-dependent limits from missing energy searches at the LHC are shown in Fig. 1.3.4. The current limits are quoted here from Ref. [45] as compared to recent direct detection limits, but this comparison must be viewed through a lens which takes the validity of operators in various energy regimes into account. Recently suggested simplified models attempt to solve the validity problem by outlining a recipe for comparison applicable across a wide energy range (see Refs. [46, 47]).

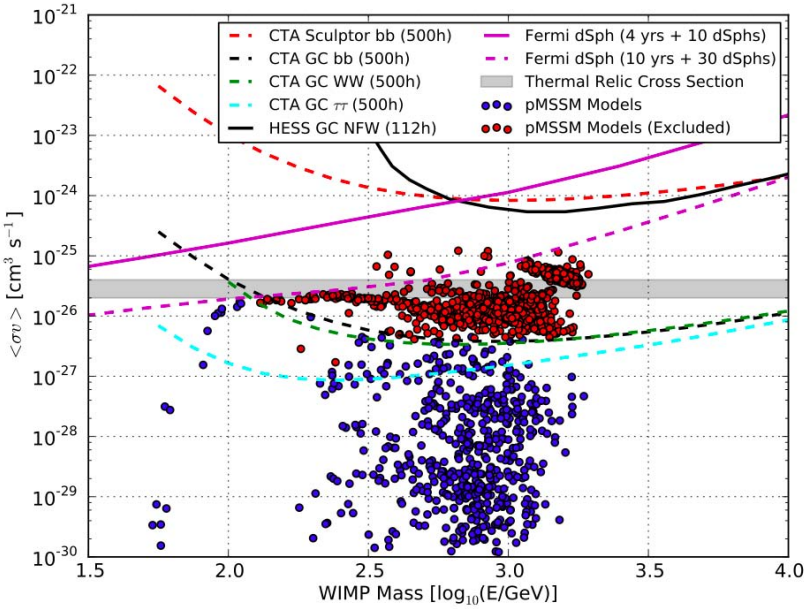

Figure 1.3.5: A collection of results from indirect detection efforts. There are Earth-based atmospheric Cherenkov detectors like HESS [48], CTA [49] and space-based experiments such as FERMI [50]. A collection of excluded pMSSM models are shown as red dots while remaining possible models are shown in blue. Figure from Ref. [42] .

1.3.2.2 Indirect Detection

Indirect searches which typically look for standard model remnants of dark matter annihilation are starting to probe the typical DM self-annihilation cross-sections in the MSMM, as shown in Fig. 1.3.5. Experiments typically look for over-densities of neutrino or gamma signals in regions where DM could accumulate and annihilate, such as in the Earth, Sun, or the core of our Milky Way galaxy. Although excesses in signal are found, it is difficult to interpret them as caused solely by dark matter since the characterization of key astrophysics models is not precisely understood [51].

1.3.2.3 Direct Detection

For over a decade, direct detection claims have been made. The longest running possible detection is the DAMA experiment which has been seeing an annual modulation signal for many years. This modulation is interpreted to be caused by an annual modulation effect

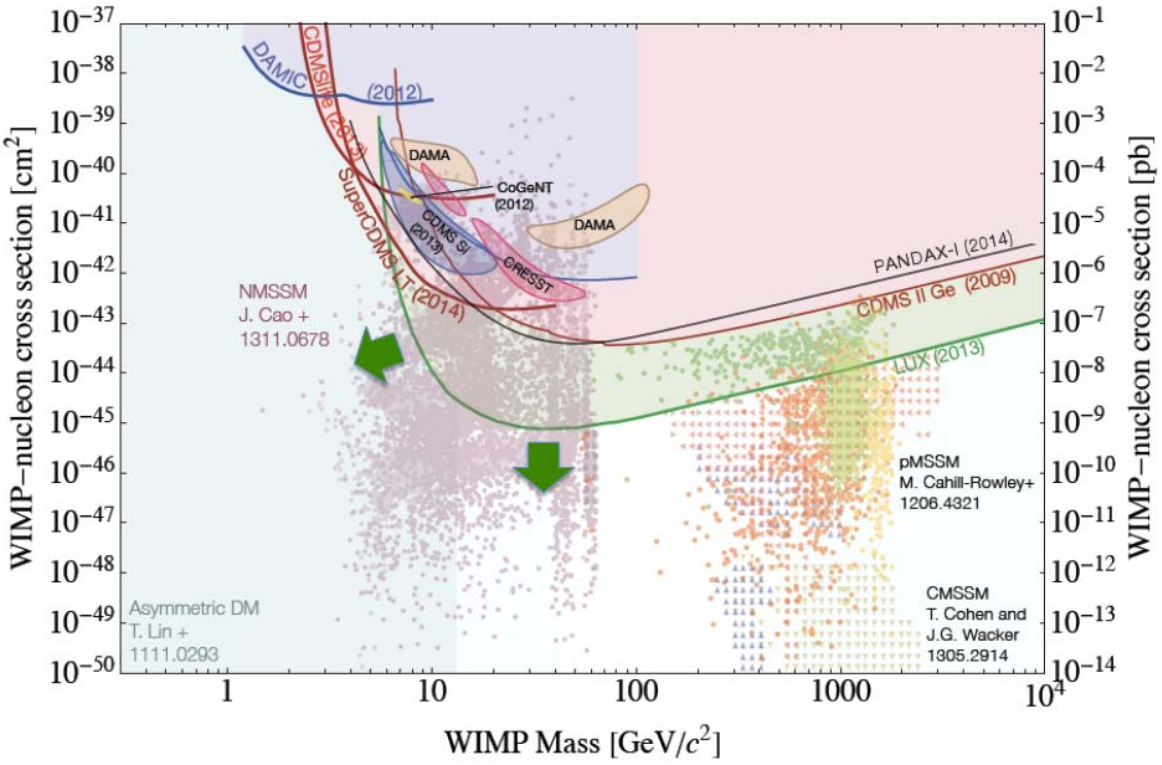

Figure 1.3.6: The collection of exclusions, detections, and proposed WIMP models which are of interest in the contemporary search for WIMP dark matter. Detections are closed contours while models are a collection of points. The exclusion curves are in heavy tension with the claimed detections. PandaX-I (black) joins the search with an exclusion result [13] that is the topic of this work. Figure from Ref. [52].

of the dark matter interaction rate caused by the Earth's motion around the solar system. The Earth revolving around the Sun gives a yearly period of higher and lower velocity in the galactic rest frame. The period of time at higher Earth velocity yields a higher event rate while lower Earth velocity gives lower rates.

The modulation signal can be interpreted as dark matter which has a mass and interaction cross-section of either 10 GeV and 10^{-40} cm^2 or 60 GeV and 10^{-41} cm^2 (depending on the interaction isotope). This caused much excitement, but as results from experiments using different direct detection technology emerged, the DAMA result was in strong tension with exclusions. In fact, multiple experiments now exclude the DM interpretation of the modulation signal by several orders of magnitude with standard WIMP assumptions.

Similar detection excitement was experienced after results from CDMS, CRESST, and CoGeNT [1–4, 8] were released which suggested low mass WIMPs. A poor understanding of background at the low energy threshold of the detectors is most likely to blame for the faint signals observed. The current world direct detection exclusion and detection curves are shown in Fig. 1.3.6, showing a tenuous relationship between detection and exclusions. The general feeling in the dark matter community is that we still have yet to see the WIMP.

CHAPTER II

Direct Detection

A large collection of astronomical evidence suggests that the Earth is bathing in a halo of several hundred km/s dark matter particles, so it is sensible for experimenters to build an Earth-borne detector that can sense the presence of the DM particles directly. The goal is to build a detector which has a very large number of target particles for which WIMPs have a large affinity. This constraint usually draws experimenters toward a target made of large mass target nuclei due to the A^2 enhancement of the spin-independent cross-section (see Sec. 2.1.1). Once the detector properties are determined, the impinging dark matter energy spectrum, detector response, and efficiency at those energies must be calculated.

As a comparison baseline, an estimate for background sources in the dark matter search window is found through Monte Carlo techniques. Once these tasks have been completed a rate estimate of events in the detector for a given cross-section and dark matter mass can be calculated. If the detector does not see events at the predicted rate, then the mass and cross-section pair are excluded as a possible interpretation of the dark matter. This process is completed iteratively over all considered mass and cross-section pairings, yielding a detection or exclusion result for the experiment. In this chapter, the process for determining the sensitivity curve for a standard dark matter WIMP detector is discussed. The exposition is largely based on the method outlined by Lewin and Smith in Ref. [53] and includes a visualization of the effects of key parameters on the sensitivity calculation. Refer to Table 2.1 for a list of variables and their descriptions used in the Chapter.

Variable	Quantity
m_χ	mass of dark matter particle
n_χ	number density of dark matter particles near Earth
ρ_χ	mass density of dark matter near Earth
v_χ	velocity of dark matter particle in detector frame
m_T	mass of target particle
n_T	number density of target particles in detector
ρ_T	mass density of target particles in detector
M_T	total mass of target
N_T	number of target particles in Earth-borne detector
V_T	volume of target material in detector
$\sigma_{T\chi}$	cross-section for dark matter and target particle
σ_0	low energy cross-section for dark and target particle
E_r	energy of recoiling target particle after interaction
v_E	velocity of the Earth in halo frame
v_{esc}	escape velocity of dark matter from Milky Way halo
v_h	galactic rotation speed in halo frame
$f_\chi(\vec{v}_\chi, \vec{v}_E)\, dn_\chi d^3v_\chi$	phase space element for dark matter particles
$f_\chi(\vec{v}_\chi)\, d^3v_\chi$	fraction of dark matter particles at velocity v
$dR = n_\chi \sigma_{T\chi} v_\chi N_T f_\chi(\vec{v}_\chi)\, d^3v_\chi / M_T$	differential interaction rate per unit target mass
$R = n_\chi \sigma_0 \langle v_\chi \rangle N_T / M_T$	interaction rate in detector per unit target mass
$E_0 = \frac{1}{2} m_\chi v_0^2$	most probable energy and velocity relation

Table 2.1: The variable quantities used in the sensitivity calculation. Quantities which apply to the WIMP are labelled with a subscript χ and for the target nucleus a subscript T.

2.1 Rate Estimate

To estimate the rate of interaction for DM in a detector, we must first determine the differential rate as a function of recoil energy. The interaction of a WIMP with a nucleus takes place at low energy due to halo velocities of WIMP particles less than an escape velocity of 700 km/s. With an initial WIMP kinetic energy in the lab frame of $E_i = m_\chi v_\chi^2/2$, a standard elastic scattering treatment yields an interaction with a target nucleus that produces a nuclear recoil with energy

$$E_R = E_i r \frac{1 - \cos\theta}{2}. \tag{2.1.1}$$

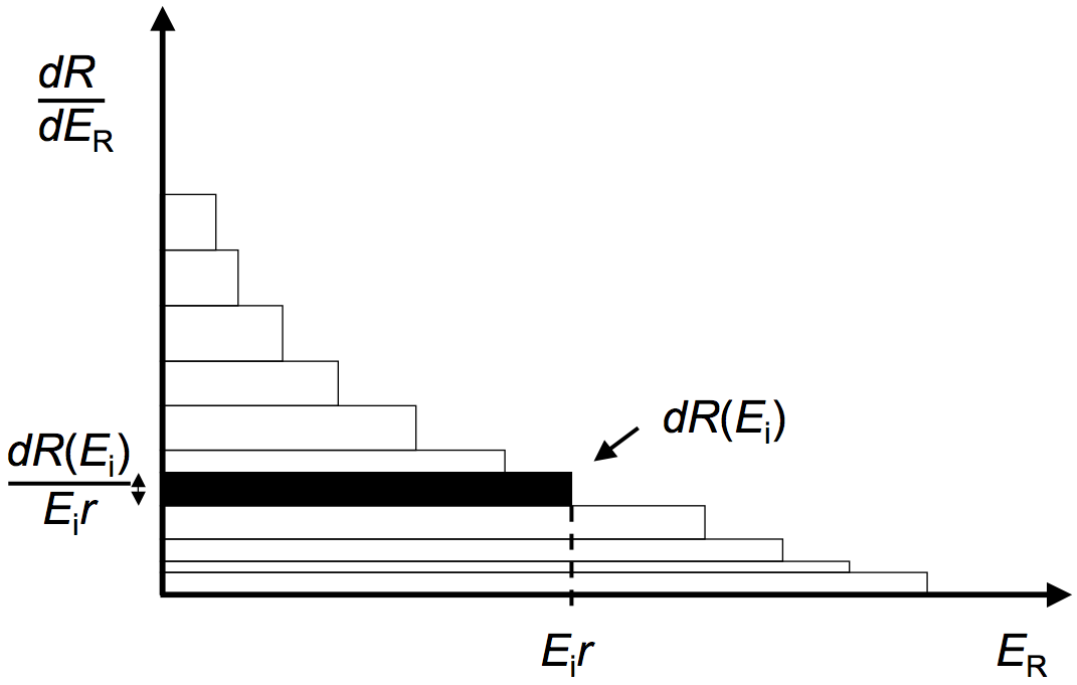

Figure 2.1.1: The differential rate spectrum for a detector with recoil of energy E_R uniformly distributed in $(0, E_i r)$ and incident energy E_i. The differential rate dR/dE_R can be determined by taking an integral with $dR(E_i)$ as the differential, then integrating from $E_i = E_{min}$ to E_{max}. Illustration from Ref. [54].

This relationship describes isotropic scatters where θ is the angle which the WIMP will scatter through. In the center-of-momentum frame $\cos\theta$ will be uniformly distributed between -1 and 1. The kinematic constant r is defined as

$$r = \frac{4 m_\chi m_T}{(m_\chi + m_T)^2}. \tag{2.1.2}$$

To determine the differential rate, we observe that at any given incident energy E_i the probability for energy deposition is uniform from 0 to $E_i r$ since $\cos\theta$ is uniform from -1 to 1. This means the contribution for each incident energy can be summed together to form an integrated total rate after finding an expression for the differential rate dR. Through inspection of Fig. 2.1.1 one can see that the differential rate as a function of recoil energy can be transformed to a differential rate as a function of incident energy. By definition, the

differential rate as a function of incident energy is $dR(E_i)$ and the height of the differential area is $E_i r$, so the width is $dR(E_i)/E_i r$. The calculation for $dR(E_R)/dE_R$ becomes

$$\frac{dR(E_R)}{dE_R} = \int_{E_{min}}^{E_{max}} \frac{dR(E_i)}{E_i r}, \tag{2.1.3}$$

where $E_{min} = E_R/r$ with E_R at the detector's low energy threshold and $E_{max} = M_\chi v_{esc}^2/2$. The relation between the most probable energy E_0 and velocity is $E_0 = \frac{1}{2} m_\chi v_0^2$ and will be used through the next discussion. Now the task is to establish the quantity $dR(E_i)$ and integrate the above equation. As noted in Table 2.1, the differential rate per unit mass is

$$dR(v_\chi) = n_\chi \sigma_{T\chi} v_\chi N_T f_\chi(\vec{v}_\chi)\, d^3 v_\chi / M_T. \tag{2.1.4}$$

The equation can be understood in the following way. Taking the product of the volume per unit time carved out by a moving WIMP $\sigma_{T\chi} v_\chi$ and the number of dark matter particles in the detector volume at a given velocity $n_\chi V_T f_\chi(\vec{v_\chi})\, d^3 v_\chi$ gives the volume carved out by all dark matter particles in the detector volume at velocity v_χ. Dividing that product by the total detector volume V_T gives the fraction of volume carved out by the WIMPs at velocity v_χ. Taking the product of the volume fraction carved out and the total number of nuclei present in the target gives the total number of interactions. Finally, dividing the total rate of interactions at velocity v_χ by the total detector mass M_T gives the of interaction rate at velocity v_χ per kilogram.

All quantities are known for the above equation except for $f_\chi(\vec{v}_\chi)$, which must have a model assumed for the Milky Way. An isotropic Maxwellian dark matter halo distribution is generally used to provide a realistic standard of comparison for different experiments across the field (although this may not be the case in the Milky Way due to tidal streams and other structure in the halo [55, 56]). That is, the standard halo profile is taken to be

$$f(\vec{v}_\chi, \vec{v_E}) = \frac{e^{-(\vec{v}_\chi + \vec{v}_E)^2/v_0^2}}{k}, \tag{2.1.5}$$

with k as a normalization constant and v_0 being the galactic rotational velocity of 230 km/s, as noted in Ref. [57]. Normalization of the halo profile with the assumption of an infinite escape velocity produces

$$k = k_0 = (\pi v_o^2)^{3/2},$$

while using a finite v_{esc} produces a normalization constant of

$$k = k_1 = k_0 \left[\text{erf}\left(\frac{v_{esc}}{v_0}\right) - \frac{2}{\pi^{1/2}} \frac{v_{esc}}{v_0} e^{-v_{esc}^2/v_0^2} \right]. \tag{2.1.6}$$

The rate differential now becomes

$$dR(v_\chi) = \frac{n_\chi \sigma_{T\chi} v_\chi N_T}{k M_T} e^{-(\vec{v}_\chi + \vec{v}_E)^2/v_0^2} \, d^3 v_\chi, \tag{2.1.7}$$

and can be inserted into Eqn. 2.1.3 after being transformed to incident energy coordinates. Using incident energy as the independent variable allows integration over the particle velocities in the halo, rather than recoil energy. To transform to incident energies, we first make the assumption of zero Earth velocity to simplify the expression without significant effect at typical incident energies

$$dR(v_\chi) = \frac{n_\chi \sigma_{T\chi} v_\chi N_T}{k M_T} e^{-v_\chi^2/v_0^2} \, d^3 v_\chi. \tag{2.1.8}$$

We denote the minimum incident energy which can produce a recoil of E_R (at recoil angle $\theta = \pi$) as $E_{min} = E_R/r$ and assume the cross-section does not depend on momentum transfer at the low WIMP velocities in our halo (since the p-wave interaction $\propto (v/c)^2$). Then, substitute the energies for velocity expressions to give

$$\frac{dR(E_R)}{dE_R} = \frac{n_\chi \sigma_{T\chi} N_T}{k M_T} \frac{2}{m_\chi r} \int_{v_{min}}^{v_{esc}} \frac{e^{-v_\chi^2/v_0^2}}{v_\chi} \, d^3 v_\chi. \tag{2.1.9}$$

After integration with an infinite escape velocity assumption, the differential nuclear recoil rate is found to be

$$\frac{dR}{dE_R}(v_\chi) = \frac{n_\chi \sigma_{T\chi} N_T}{k M_T} \frac{4\pi v_0^2}{m_\chi r} e^{-v_\chi^2/v_0^2}.$$

Substituting $k = k_0$ and regrouping gives

$$\frac{dR}{dE_R}(v_\chi) = \frac{2n_\chi \sigma_{T\chi} v_0 N_T}{\pi^{1/2} M_T} \frac{1}{\frac{1}{2} m_\chi v_0^2 r} e^{-v_\chi^2/v_0^2},$$

which can be converted back to energies to yield

$$\frac{dR}{dE_R}(E_R) = \frac{2n_\chi \sigma_{T\chi} v_0 N_T}{\pi^{1/2} M_T} \frac{1}{E_0 r} e^{-E_R/E_0 r}.$$

We have now achieved the differential rate as a function of E_R. The factor out front is now recognized as the total rate when integrated over all possible recoil energies

$$R_0 = \frac{2n_\chi \sigma_{T\chi} v_0 N_T}{\pi^{1/2} M_T} = \frac{2}{\pi^{1/2}} \frac{\rho_\chi \sigma_{T\chi} v_0}{m_T m_\chi}. \tag{2.1.10}$$

This allows the final differential recoil rate to be written in a simplified form as

$$\frac{dR}{dE_R}(E_R) = \frac{R_0}{E_0 r} e^{-E_R/E_0 r}. \tag{2.1.11}$$

Determing the interaction rate is now a matter of integrating over recoil energies. The equation is integrated over the recoil energy range in which a detector is sensitive (usually the low energy threshold to infinite energy). Using a realistic escape velocity $v_{esc} = 700\,\mathrm{km/s}$ instead of infinity coupled with $v_0 = 230\,\mathrm{km/s}$ changes the result by less than a percent [53].

An expression for the cross-section is now within reach. Solving for $\sigma_{T\chi}$ in the equation above for R_0, inputting a length of operation of the detector t, and selecting a minimum number of signal events $N_{events} = R_0 t$ (typically of order one) yields a fair estimate to an experiment's sensitivity to $\sigma_{T\chi}$,

$$\sigma_{T\chi} = \frac{\pi^{1/2}}{2} \frac{R_0 m_T m_\chi}{\rho_\chi v_0} = \frac{\pi^{1/2}}{2} \frac{m_T m_\chi}{\rho_\chi v_0 t} N_{events}. \tag{2.1.12}$$

As a concrete example, assume an experiment has perfect acceptance across the entire recoil energy range and the experimentalists are confident that DM would be detected at $N_{events} = 3$ events over background. Also, use xenon as a target with an atomic mass of $m_T = 131.29\,\mathrm{amu}$ and use a dark matter density near the solar system of $\rho_\chi = 0.4\,\mathrm{GeV\,c^{-2}cm^{-3}}$ and velocity of $v_0 = 220\,\mathrm{km/s}$. With these assumptions, we get a behavior such as

$$\sigma_{T\chi} \propto \frac{m_\chi}{t}. \tag{2.1.13}$$

This behavior is unrealistic since actual detectors always have a low energy threshold which affects the low WIMP mass region. Nonetheless, for WIMP masses near $100\,\mathrm{GeV\,c^{-2}}$ and above the trend is followed closely by the above equation. That is to say, the local DM density limits the number of local particles available to scatter (since $n_\chi = \rho_\chi / m_\chi$ shows up in the cross-section equation with ρ_χ constant), and with a longer exposure the experiment probes the WIMP-nucleus cross-section more deeply. If one considers the energy threshold effect, then equation 2.1.11 must be integrated from the finite low energy threshold to obtain

$$R(E_{thresh}, \infty) = R_0 e^{-E_{thresh}/E_0 r}, \tag{2.1.14}$$

which modifies the cross-section equations thusly,

$$\sigma_{T\chi} = \frac{\pi^{1/2}}{2} \frac{m_T m_\chi}{\rho_\chi v_0 t} N_{events} e^{-E_{thresh}/E_0(m_\chi) r(m_\chi)} \tag{2.1.15}$$

and

$$\sigma_{T\chi} \propto \frac{m_\chi}{t} e^{-E_{thresh}/E_0(m_\chi) r(m_\chi)}. \tag{2.1.16}$$

The fact that r and E_0 are a function of m_χ is emphasized. The additional exponential factor causes the well known low mass cutoff seen in sensitivity plots as seen in Figs. 1.3.6 and 2.1.2.

2.1.1 Precise Rate Estimate

The above treatment for finding the WIMP-nucleus interaction rate in a detector largely encompasses the quantitative and qualitative properties of WIMP detection. However, more precise calculations can be done which take into account the Earth's motion in the galactic halo, a finite escape velocity, a nuclear form factor, and the specific particle interaction properties.

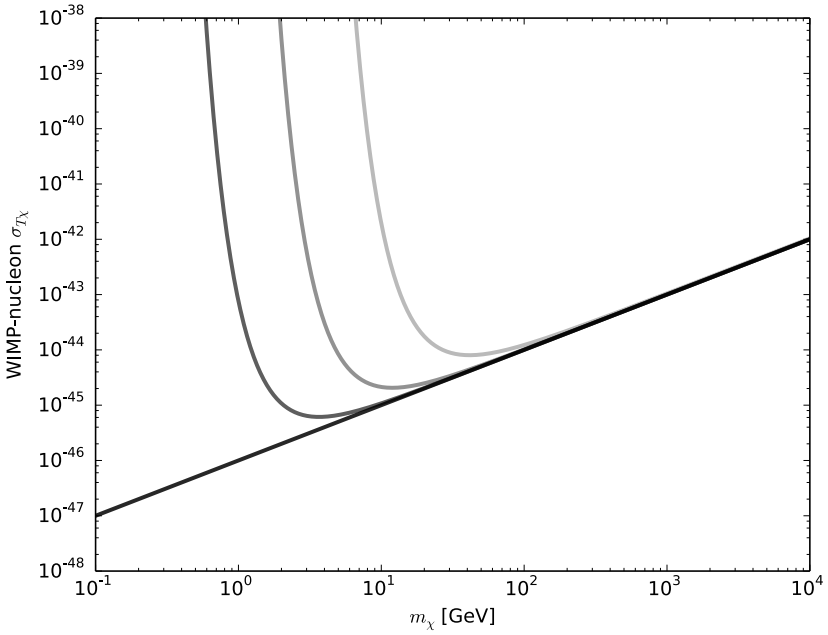

Figure 2.1.2: Estimated sensitivity curves for a detector with no low energy threshold (black) and increasing energy thresholds per decade (dark gray, gray, light gray). As the energy threshold is increased the sensitivity to low mass WIMPs wanes. Not shown is the slight reduction of overall rate at high mass (shown in Fig. 2.1.4).

A modification of the energy spectrum which includes the annual modulation is given as

$$\frac{dR}{dE_R}(E_R) = c_1 \frac{R_0}{E_0 r} e^{-c_2 E_R / E_0 r}. \tag{2.1.17}$$

The constants c_1 and c_2 are calculated at various points throughout the year, as listed in Ref. [53], but typical values of $c_1 = 0.751$ and $c_2 = 0.561$. A finite escape velocity can also be included in the rate by subtracting of the high velocity component and scaling properly [53], to yield

$$\frac{dR}{dE_R}[E_{thresh}, E_{esc}](E_R) = \frac{k_0}{k_1}\left[\frac{dR[E_{thresh}, \infty]}{dE_R} - \frac{R_0}{E_0 r} e^{-E_{esc}/E_0 r}\right]. \tag{2.1.18}$$

Taking account of the velocity dependence of the cross-section can be done at low energies

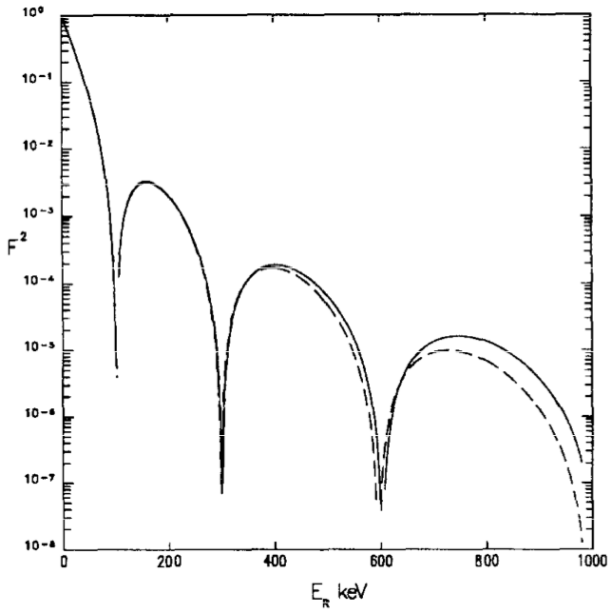

Figure 2.1.3: Helm form factor parametrization (dashed) compared with full Fermi form factor (solid). For high energy recoils, the form factor suppresses interactions due to decoherence of the nucleon wavefunctions. Iodine ($A = 127$) is shown but similar behavior is seen for xenon ($A = 131$) using $s = 0.9$ fm, $r_n = 1.14A^{1/3}$ fm. Figure from Ref. [53].

by including the effects of a nuclear form factor. The momentum transferred to the nucleus is denoted as

$$q = \sqrt{2m_T E_R},$$

and a typical nuclear radius is taken to be $r_n = 1.14A^{1/3}$ fm. With $\hbar = 1$, the quantity qr_n is unitless and parametrizes the effect of the form factor on nuclear interactions. An analytic form factor which approximates the numerically determined SI form factor well is the Helm form factor

$$F(qr_n) = 3\frac{j_1(qr_n)}{qr_n}e^{-(qs)^2/2}, \tag{2.1.19}$$

where $j_1(qr_n)$ is a spherical Bessel function of the first kind and s is of order 1 fm. To include the form factor, the cross-section must be redefined to include the momentum transfer

dependent factor $F(qr_n)$ and a zero momentum cross-section $\sigma_{T\chi 0}$ to give

$$\sigma_{T\chi} = F(qr_n)\sigma_{T\chi 0}. \tag{2.1.20}$$

The zero momentum transfer cross-section can be factored [34] into a more revealing form

$$\sigma_{T\chi 0} = 4G_F^2 \mu_{T\chi}^2 C, \tag{2.1.21}$$

where G_F is the Fermi constant, $\mu_{T\chi}$ is the reduced mass of the WIMP-nucleus pair, and C contains the specific particle model content. The particle physics coupling can depend on spin, but the topic of this work focuses on the spin-independent interaction. The C_{SI} factor can be written [34] as

$$C_{SI} = \frac{1}{\pi G_F^2} \left[Z_T f_p + (A_T - Z_T) f_n \right]^2, \tag{2.1.22}$$

where A_T is the mass number of the target nucleus, Z_T is the number of protons in the target nucleus, f_p is WIMP-proton coupling, and f_n is the WIMP-neutron coupling. In the nucleon agnostic interaction case, $f_p = f_n$, so the equation simplifies to

$$C_{SI} = \frac{1}{\pi G_F^2} \left(A_T f_p \right)^2. \tag{2.1.23}$$

Using C_{SI}, we see the full detailed equation for the spin-independent WIMP-nucleus cross-section

$$\sigma_{T\chi}^{SI} = F(qr_n) \frac{4\mu_{T\chi}^2 A_T^2 f_n^2}{\pi}. \tag{2.1.24}$$

The above equation can be rescaled to remove the target mass dependence so that a cross-section for a single nucleon $\sigma_{p\chi}^{SI}$ is obtained. Rescaling the A_T^2 and $\mu_{T\chi}^2$ dependence achieves

$$\sigma_{p\chi 0}^{SI} = \frac{\mu_{p\chi}^2}{\mu_{T\chi}^2 A_T^2} \sigma_{T\chi 0}. \tag{2.1.25}$$

The WIMP-nucleon cross-section σ_{pT}^{SI} can be found and compared across experiments of varied target types. This WIMP-nucleon cross-section is the traditional quantity reported in contemporary WIMP searches.

2.1.2 Sensitivity Estimation

Now the discussion moves toward determining an actual detector's sensitivity. In the previous calculations, we assumed that our detector had zero background, perfect energy resolution, and perfect event acceptance. In reality a given detector may or may not have a background, but it certainly will not have perfect energy resolution nor perfect event acceptance. Additionally, the measured quantities are only a proxy for the physical values, so the mapping between detector response and the actual recoil energies must be determined (or assumed).

2.1.2.1 Energy Resolution

Each detector which serves as a calorimeter will have an intrinsic energy resolution which depends on several factors like the Fano factor [58], geometric considerations, and transducer statistics (see Sec. 3.5.9 for a discussion of effects in liquid xenon detectors). The statistical spread in detected quanta is approximately Gaussian in nature (Poissonian at low energy) with the mean proportional to E and the width proportional to $\sqrt{E}$. The detector energy resolution defined as $\sigma/E = \alpha/\sqrt{E/\text{MeV}}$ will impart an intrinsic uncertainty to the energy of a detected signal since a singular detected signal could correspond to a spectrum of energies. A finite detector resolution will allow energies below the detector threshold to fluctuate upward and be detected, or for events above the threshold to fluctuate downward and not be detected at all. This must be accounted for in the acceptance function.

2.1.2.2 Acceptance

Since detectors do not have infinite energy resolution and perfect background rejection, an experimental effort must take these detection effects into account. Uncertainty in signal inversion caused by a detector's energy resolution will allow energy depositions outside the average energy search region to fluctuate past the threshold, likewise for events in the search

window to fluctuate out of the detection region. The modified differential rate for Poissonian events for a reconstructed energy $E_v = n\epsilon$ is

$$\frac{dR}{dE_v} = \frac{1}{n!\epsilon}\int \frac{dR}{dE'_v}\left(\frac{E'_v}{\epsilon}\right)^n e^{-(E'_v/\epsilon)}dE'_v, \tag{2.1.26}$$

with n being the number of detected quanta and ϵ representing the energy conversion factor. In the low energy searches which are typical for dark matter direct detection the smearing can be considerable. The steeply falling exponential energy spectrum for WIMP-nucleus interactions (especially at low WIMP mass) can have a boosted overall rate relative to the naive calculation, due to the smearing. An additional factor in the acceptance function must be applied on the differential rate to account for the energy dependence of analysis cuts (typically 0.3 across the search range).

2.1.2.3 Background

Estimating the background of an experiment is not an easy task but a baseline expected rate must be established in order to determine if a signal was observed. Once the background rate estimate has been achieved for the detector's energy window, the overall number of expected events can be estimated. Usually, the expected number of events will be well below O(10) and ideally are not much greater than one to ease the detection procedure.

The statistics model which handles the very low event number regime is that outlined by Feldman-Cousins [59]. The model gives the number of predicted events N_{FC} (upper limit) which would be ruled out at 90% C.L. when considering the expected background. One can then rule out all particle models which predict a number of events greater than the Feldman-Cousins quantity. Practically speaking, this means that one solves for the cross-section (similar to Eq. 2.1.12 but with energy dependence taken into account) and sets the product of the predicted rate and operation time to $Rt = N_{FC}$. The WIMP mass can be scanned in this manner and a curve generated.

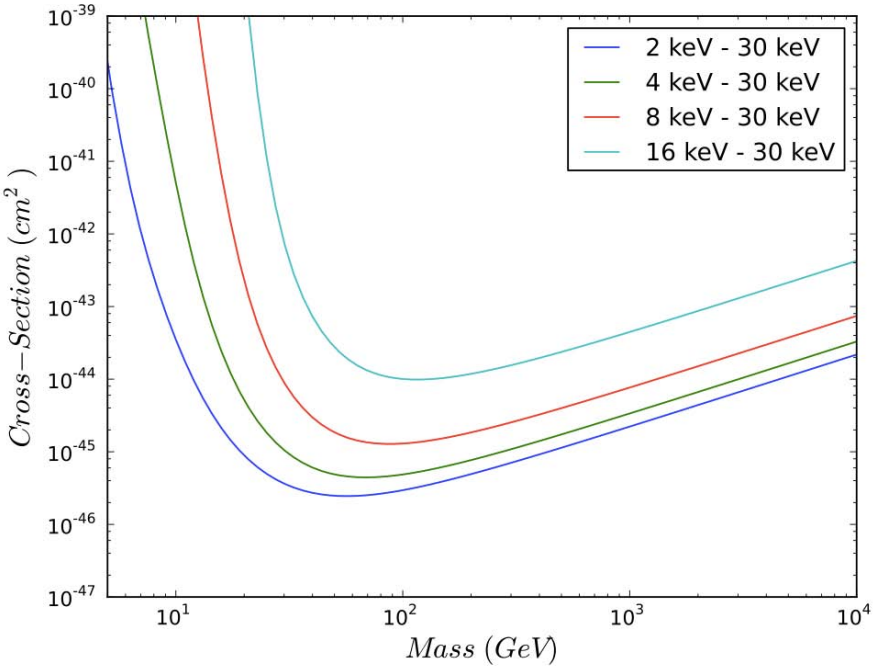

Figure 2.1.4: Sensitivity of hypothetical detector with differing energy thresholds but same energy cutoff and resolution. When the threshold is lowered the overall rate increases across the entire mass range. The rate significantly increases at low WIMP mass due to the steep WIMP-nucleus energy spectrum at low m_χ.

2.1.3 Curve Behavior

Is it worthwhile to explore the end result of the sensitivity calculation once all effects have been taken into account. For instance, consider the curves shown in Fig. 2.1.4. The full acceptance function has been applied to the analytic form and integrated for all WIMP masses, then plotted. A sensitive energy window with a recoil energy threshold at 2, 4, 8, 16 keV and a cutoff at 30 keV. The general trend can be seen as this: as the threshold is lowered, the overall rate will go up for all WIMP masses, but also the experiment becomes more sensitive to lower WIMP masses.

Additionally, consider a detector which is able to keep the energy threshold the same while changing its energy resolution as in Fig. 2.1.5. As the energy resolution worsens the detector is not able to reconstruct energies precisely, but its overall rate for low WIMP masses still increases (increasing its sensitivity at low WIMP mass). Note that a worse energy resolution

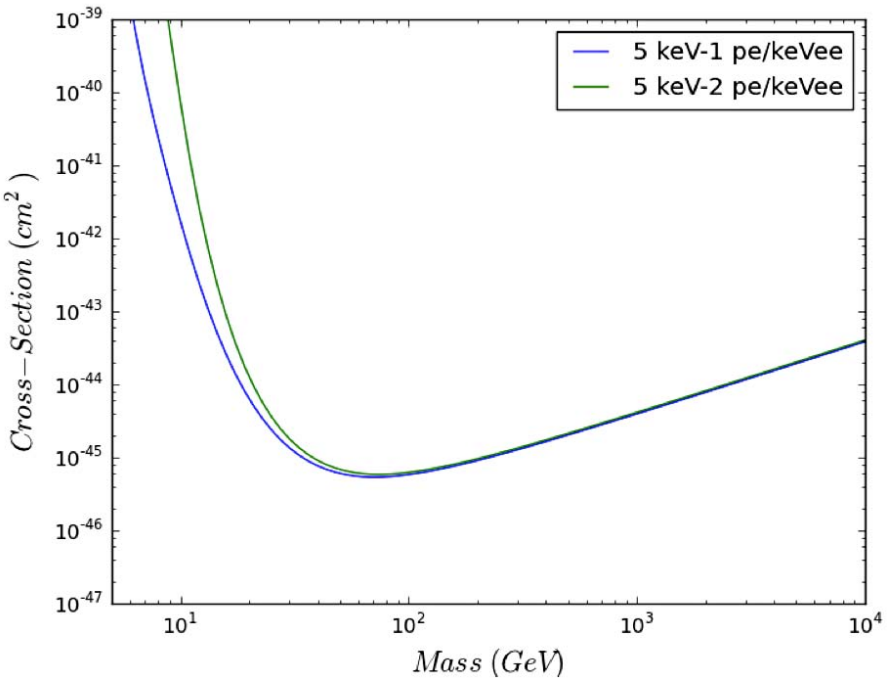

Figure 2.1.5: Sensitivity of a hypothetical detector with varying detector energy resolution but the same energy threshold (5 keV). The energy resolution is worse for a detector with lower quanta collection efficiency (1 quanta/keV), which leads to greater energy smearing and leakage. Events leak both ways across the threshold but the low energy events leak preferentially due to the decaying exponential rate.

giving a better rate at the same threshold is not a paradox. In practice, if an identical detector could tune its energy resolution to be better, then it could also lower its threshold which would result in a net overall rate increase.

CHAPTER III

Particle Detection in Dual Phase Liquid Xenon

At energies of interest to dark matter searches O(10 keV_{nr}), particles impinging upon a liquid xenon target will deposit energy through scattering off the electrons or nuclei that constitute the bulk material. The struck target particle recoils throughout the thicket of xenon atoms in the bulk of the material, finally coming to a stop within a few micrometers. If the impinging particle strikes an electron, causing it to recoil, the event is denoted as an electron recoil (ER). If the impinging particle strikes a xenon nucleus, the event is termed a nuclear recoil (NR). Most events are of a single type, but circumstances can arise which produce events having both recoiling electrons and nuclei originating from one event. For example, a mixed ER and NR recoil can be produced when both an ER from the emitted radioactive particle and an NR from the recoiling parent nucleus occur in the target, as in a metastable ^{131m}Xe decay.

The vast majority of background radiation encountered within a detector is electromagnetic (EM) in origin. The ER background can be removed with high efficiency using discrimination techniques, but nuclear recoils present a different challenge. Background NR events are generally caused by fast neutrons which deposit energy in the detector through elastic scattering. There is no way to discriminate single vertex background recoils from the WIMP-nucleus signal, so the neutron induced NR background must be reduced to very small rates.

See Ref. [60] for a thorough review of liquid xenon used in several particle detection technologies with application in physics beyond dark matter searches. A discussion of the energy scales and quenching factors used in LXe direct detection experiments is located in Appendix

A. The types of LXe detectors and properties of signal generation in liquid xenon are detailed in this chapter.

3.1 LXe as a Detector Medium

Liquid xenon (LXe) has highly desirable characteristics for a detector medium. The high density means there are many target nuclei within a unit volume, making LXe based detectors compact. Also, the interaction lengths are short allowing a self-shielding effect which protects an inner fiducial volume. Additionally, the material can easily be purified and handled at the relatively modest cryogenic temperature of 180 K. Relevant physical properties of xenon for particle detection are given in Table 3.2.

Material Property	Value & Unit	Conditions
Atomic number Z	54	
Atomic weight A	131.30 g/mole	
Boiling point T_b	165.65 K	1 bar
Melting point T_m	162.3 K	1 bar
Density ρ_{liq}	3.09 g/cm^3	1 bar, 160 K
Volume ratio ρ_{gas}/ρ_{liq}	518.9	
Critical point T_c, P_c	289.7 K, 57.6 bar	
Triple point T_3, P_3	161.3 K, .805 bar	
Radiation length X_0	2.8 cm	
Molière radius R_M	5.6 cm	
$-(dE/dx)_{mip}$	3.89 MeV/cm	min. ioniz. particle
Interaction length λ_I	55 cm	
Refractive index n	1.75	$\lambda = 176$ nm

Table 3.2: Xenon physical properties as reproduced from Ref. [61].

Signal generation in LXe consists of quanta from ionization but also from excimers which decay to photons (characteristic of the noble elements). The charge and light detection channels provide a basis for discrimination between electronic recoils (background) and nuclear recoils (signal) on a per-event basis. The material is easily procured from specialty gas providers and the simple design of dual phase detectors allows effective scaling in relatively short time scales.

3.2 Liquid Xenon Detector Types

The two prominent topologies of a liquid xenon detector are the single phase and dual phase types. A single phase detector nominally employs a LXe target with no applied electric field and no gaseous xenon in the sensitive volume. Single phase detectors lack low energy position reconstruction ability but enjoy a boost in sensitivity due to its reliance on pure scintillation as the signal carrier. The recombining ionization signal will produce additional scintillation, lowering the single phase threshold. The dual phase xenon detectors use both LXe and GXe within the sensitive volume while employing a time projection chamber design to produce drift, extraction, and acceleration electric fields. This topology elicits a more refined detector response to an event inside the target volume, producing signals from both scintillation and ionization from the particle interaction.

Both single and dual phase detector topologies can benefit from fiducialization to suppress a large number of background events. Electromagnetic background events originating from outside the sensitive volume tend to stop within centimeters as they enter the LXe from all directions. This self shielding effect means that the volume just inside the skin is very quiet (since nearly all external particles have already stopped in the skin), which allows detectors with position reconstruction abilities to select an internal, low background 'fiducial volume'.

3.2.1 Single Phase LXe

In a single phase design, the key components are the LXe target, the photomultiplier tubes, and the light reflector. Nominally, this means a spherical 4π array of PMTs has been constructed with a virgin Teflon reflector covering any exposed non active surfaces (Teflon is diffusely reflective from visible to below 160 nm wavelengths). The spherical volume is then filled completely with LXe. A particle can impinge upon the target and deposit energy, but the result will only be scintillation. The particle interactions in a single phase design are identical to that of a dual phase (discussed below), but in a single phase detector an electric field is not applied so does not separate ionization from the excimers. In this case, both the excimers and ionization will decay through the standard production of VUV photons. The lack of separated scintillation and ionization signal in the single phase design means there is a reduced ability to reconstruct the position and type of an energy deposition, leading to

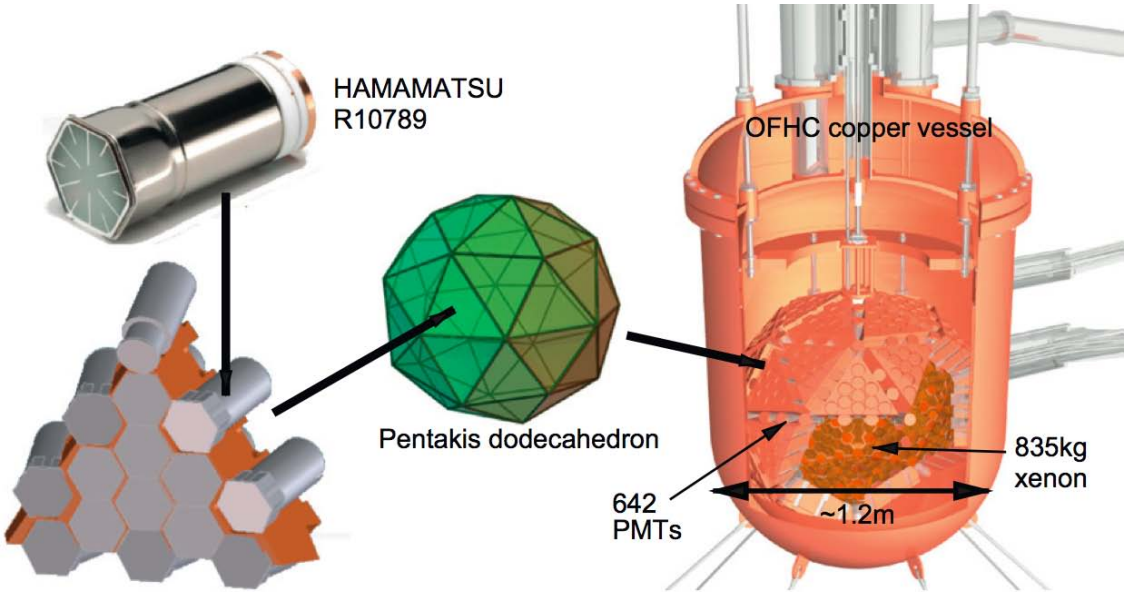

Figure 3.2.1: A schematic outline of the single phase LXe XMASS detector. The nearly spherical volume is surrounded by PMTs which observe prompt scintillation signals produced by events in the central volume. Figure from Ref. [62].

reduced background suppression ability. At energies around 25 keV_{nr} and above, position reconstruction can be used to define a fiducial volume that spatially suppresses background due to the LXe self shielding effect. The ZEPLIN-I experiment was able to demonstrate limited background rejection through pulse shape discrimination (PSD) in LXe [63] but the XMASS collaboration, which has operated a large scale single phase LXe detector with success in several avenues (see Fig. 3.2.1 and Ref. [62]), relies on position reconstruction to suppress electromagnetic background through fiducialization.

3.2.2 Dual Phase LXe

For dual phase detectors, the key components are similar to those in single phase detectors but the geometry is changed to be cylindrical in nature. The dual phase design allows effective probing of both the light and charge signal generated from a particle interaction in LXe. The liquid level is lowered to expose a gaseous xenon environment within the sensitive volume and planar grids are added for generation of the time projection chamber electric fields (see Fig.

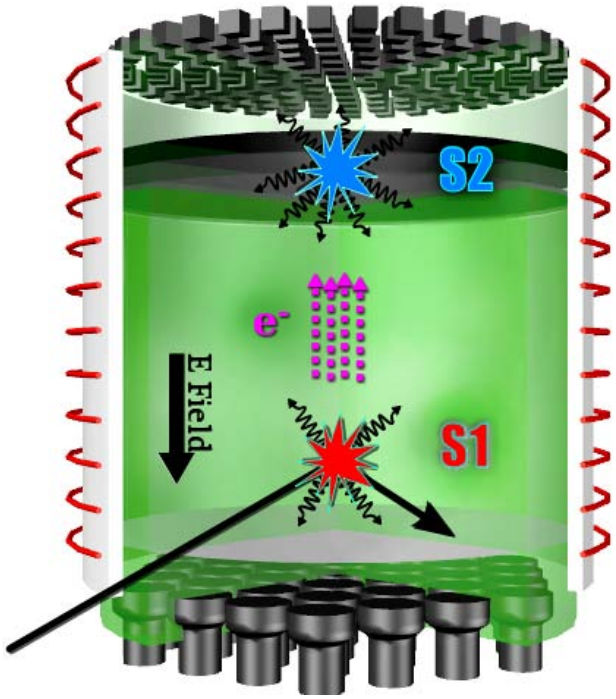

Figure 3.2.2: A schematic of an interaction in a dual phase liquid xenon time projection chamber. The cylindrical volume is instrumented with PMTs on top and bottom, fitted with electrodes for electric field generation, and surrounded by an efficient PTFE reflector with field shaping rings. The volume is filled with LXe where prompt scintillation (S1) is produced due to particle interaction. Drifting ionization electrons travel upward toward the liquid/gas interface, get extracted from the surface, and are accelerated to produce the proportional scintillation signal (S2). The dual signal nature gives good background discrimination and precise position reconstruction capabilities across the WIMP search energy region.

3.2.2). Low energy dual phase liquid xenon detectors use proportional charge amplification in the gas region to extend the energy threshold down to the keV$_{nr}$ level [60]. With the position reconstruction and separate light and charge identification abilities, dual phase detectors allow for both spatial background suppression and electromagnetic background discrimination down to an energy threshold of around 5 keV_{nr}.

3.3 Impinging Particle

The principle for detection within a time projection chamber relies on the scattering of particles within the target material which deposits energy and liberates detection quanta in the detector medium. This deposition of energy through scattering is an inherently discretized process which allows a particle to scatter once or multiple times within the volume. The resulting recoils from the target particle, on the other hand, endure an even more chaotic process since the recoiling particle loses energy through a multitude of ionizing scatters along its track through the medium.

Usually the impinging particle makes it to the sensitive target volume due to the fact that it is not very interactive with the target material (or else it would have been stopped outside the volume from the self-shielding effect). On the other hand, a recoiling target nucleus is very interactive with the other target atoms. This asymmetry means that impinging particles will behave in a multitude of ways (not scattering at all, or scattering once, twice, or more) but the recoiling particles have a predictable response (they get stopped in the target after leaving a short track of excitation and ionization). This process of energy deposition and its result in a LXe detector is described in detail below.

3.3.1 No Scatter

A rare event scattering discussion is not complete without mentioning the possibility that many particles will enter the detector and exit without ever touching a thing inside the detector. For a dark matter particle or neutrino this is overwhelmingly the case. If there is no scatter inside the detector then there will be no signal response so no detection of the passer-by particle. This fact drives rare event searches to rely on a high flux and a large target to achieve a perceptible rate of events.

3.3.2 Single Scatter

The single scatter is what DM searches hope for since a DM particle interacting in the target volume will produce only a single scatter. An interacting dark matter particle will

never double scatter inside the detector since the probability is vanishly small (building a detector hoping for a single scatter is one thing, but two scatters from a single DM particle is a vanishingly small probability). It is also possible for background particles (like neutrons) to scatter only one time in the target volume. For single scatters, the particle will enter the detector and impinge upon a target nucleus or electron, then either be totally absorbed (e.g. photoabsorption) or scatter and continue on its way out of the detector without interacting any further.

3.3.3 Multiple Scatters

Backgrounds from neutron and electromagnetic sources tend to scatter multiple times in the target. Since multiple scatters will happen within a few nanoseconds of each other, detectors must rely on spatial separation between the scatters (rather than time resolution) to notice the multi-scatter feature and discriminate against it. In large detectors the neutron multiple scattering fraction is very high, allowing for further effective discrimination of neutron background in next generation detectors.

3.4 Recoiling Target Particle

The recoiling target xenon nucleus or electron bleeds off kinetic energy through collisions in the bulk. In all cases the particle comes to rest on the micrometer scale but the track topology may vary substantially during the slowdown. The particle can come to stop or produce secondary nuclear recoils in a branched structure. This variability in the topology of the recoil track is thought to be the source of the signal variance seen when the recoil energy and particle are identical (see Sec. 3.5.9.2 for anti-correlation discussion).

The signature of a recoiling electron (ER) when compared to a recoiling xenon nucleus (NR) differs in liquid xenon when there is an applied electric drift field. For a given primary scintillation signal (S1) size, the ER will produce a larger ionization signal (S2) than the NR will, allowing for discrimination between the two types of events. An additional benefit of the time projection chamber is the ability to reconstruct the position of the interaction. The time difference between S1 and S2 signals gives the z coordinate while the pattern produced

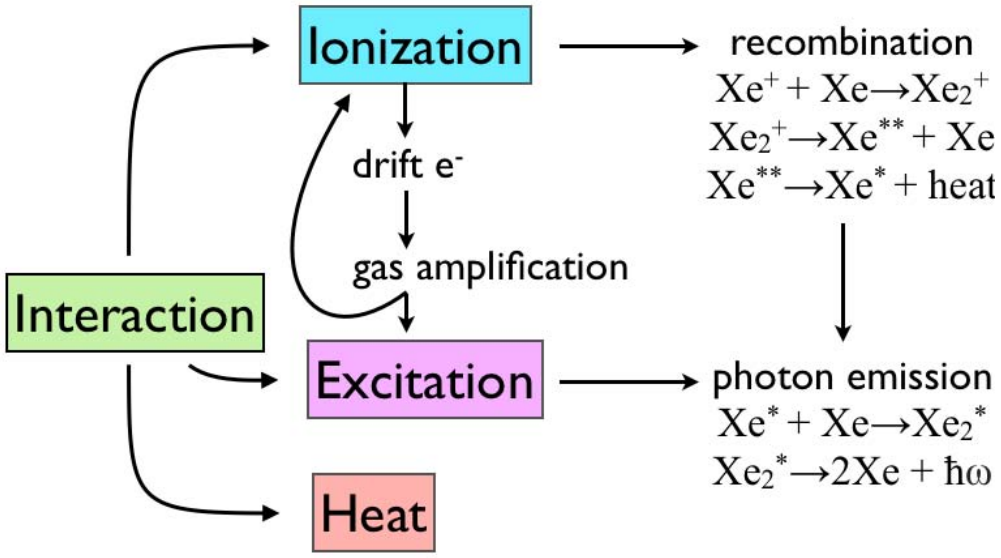

Figure 3.4.1: Schematic of signal production as a result of particle interaction in xenon. Heat, ionization, and excitons are produced. Heat information is discarded but ionization can either result in free drifting electrons or a collapse back down to excitons via recombination. Excitons (dimers) decay to produce 178 nm wavelength photons which can be read via light transducers in the detector. Note: free electrons which balance charge in equations are omitted to increase clarity.

in the PMT arrays gives the x-y coordinates of the interaction vertex. Here we discuss the details of the recoiling particle in the target material.

3.4.1 Energy Deposition

A highly interacting particle moving within the target volume will slow down quickly and come to a halt. This is the case for both recoiling nuclei and recoiling electrons. The moving particles will deposit their energy into three differing channels: heat, charge, light. The heat quanta (phonons) liberated into a detector are very difficult to detect for low energy interactions. Several semiconductor crystal detectors are able to catch this heat signal but LXe detectors are not capable in present form, so reading the heat signal is not attempted. However, dual phase LXe detectors are very good at collecting the charge signal (ionization electrons) and the light signal (scintillation photons), so these are the channels used.

3.4.1.1 S1 Signal

The light signal from interactions in a dual phase LXe detector are termed S1 (first scintillation). The production mechanism for this type of event is shown in Fig. 3.4.1 via the excitation path. As the recoiling target particle comes to rest it produces phonons, ionization electrons, and excited xenon atoms Xe^*. The phonon quanta are not measured, the ionization electrons will be discussed shortly, and the excited xenon atoms combine to form short-lived excited dimers (excimers). These excimers decay on a short time scale O(10 ns) with emission of VUV photons at 178 nm. A portion of the ionization will also collapse into an excimer state and emit UV photons of the same form on the same short time scale. This partial collapse is due to the inability to drift all ionization electrons away from the interaction site before they find stray Xe^+ ions with which to combine - i.e. some ionization electrons are inevitably lost to recombination. The recombination electrons deduct from the ionization signal and add to the S1 signal.

3.4.1.2 Drifting Ionization Electrons

After the heat signal is lost and the light signal is produced from both pure Xe^* excimers and recombination, the ionization signal must be handled. The leftover ionization electrons start to drift in the applied drift field toward the anode (electrons have an affinity for positive voltage). The ionization electrons drift at a constant velocity of about 2 mm/μs (see Fig. 3.4.2) which, in typical detector physical sizes, corresponds to drift time scales of O(1 to 500 μs). During drifting, the ionization electrons will diffuse at a constant rate and upon reaching the surface, the diffused electron cloud will be extracted to produce an S2 signal. The diffusion is seen in the S2 signal as a lengthening of the S2 pulse in time. Additionally, the S2 signal will be reduced as a function of drift length due to impurities which are present in the detector (see Fig. 3.4.3).

3.4.1.3 S2 Signal

The ionization electron cloud passes through the LXe target as it rises to the top of the detector, where the gate (see Sec. 5.6.1) sits just below the liquid/gas interface and the

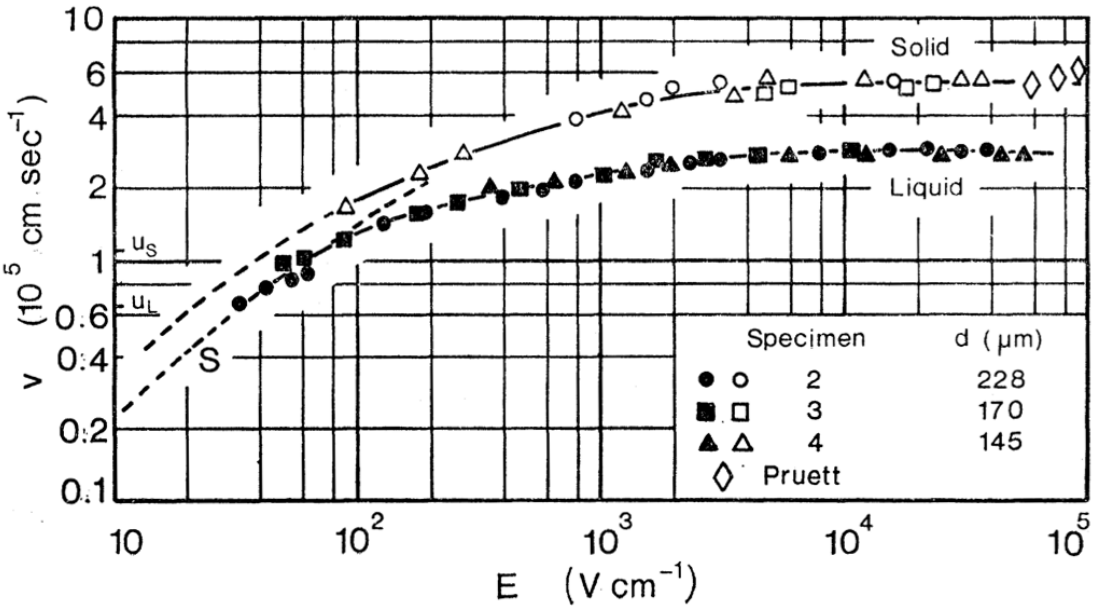

Figure 3.4.2: Drift velocity of ionization electrons in liquid and solid xenon as a function of applied electric field. Typical dual phase xenon detectors operate with near kilovolt electric drift field. The curve S is calculated from Shockley theory [64]. Figure from Ref. [65].

anode a few millimeters above. The electrons are extracted from the liquid into the gas phase and accelerated to produce a secondary scintillation signal in the gas phase, termed S2. This gaseous scintillation signal is produced with the same excimers/ion cascade with short decay time O(10 ns) as outlined previously. The duration of the S2 signal is O(1 μs) and is largely set by the distance from the liquid/gas interface to the anode grid with widening from electron diffusion in the z direction.

3.4.2 Electronic Recoil

If the impinging particle is electromagnetic in nature, i.e. alpha, beta, or gamma, then it will most frequently interact with the electron cloud surrounding the xenon nucleus, not the nucleus itself. It is possible that very high energy particles may produce excited nuclear states, but the vast majority of events due to EM radiation will be electronic in nature. These interactions will scatter from an electron or multiple electrons, producing recoiling electrons. This type of interaction is termed an electronic recoil (ER). A recoiling electron

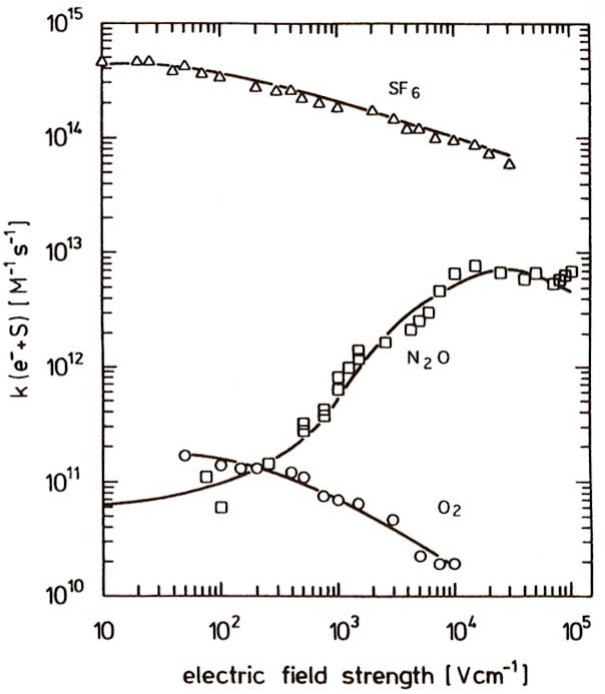

Figure 3.4.3: Electron attachment cross-section for impurities in liquid xenon with curve fits. Both O_2 and SF_6 cross-sections are reduced with higher applied drift field, but N_2O increases markedly in the high field region O(kV). Impurities will capture the drifting electrons and reduce the ionization signal, necessitating a purification scheme in LXe detectors. Figure from Ref. [66].

will tend to interacting more readily with atomic electrons in the target bulk to produce a high ratio of ionization electrons to xenon excimers, when compared with nuclear recoils. Additionally, an electron recoiling at one keV will have a velocity of around $0.1c$ while a recoiling nucleus will be moving much slower at around $10^{-4}c$. The high velocity of electron recoils results in much lower ionization density when compared with NR (see Fig. 3.4.4).

3.4.3 Nuclear Recoil

When an impinging particle scatters off a xenon nucleus the interaction is termed a nuclear recoil (NR). The scatter imparts momentum to the recoiling nucleus, sending it on a path through the bulk material while it quickly bleeds off speed in a short distance O(μm). The recoiling nucleus bumps into other xenon atoms along with producing excitation and

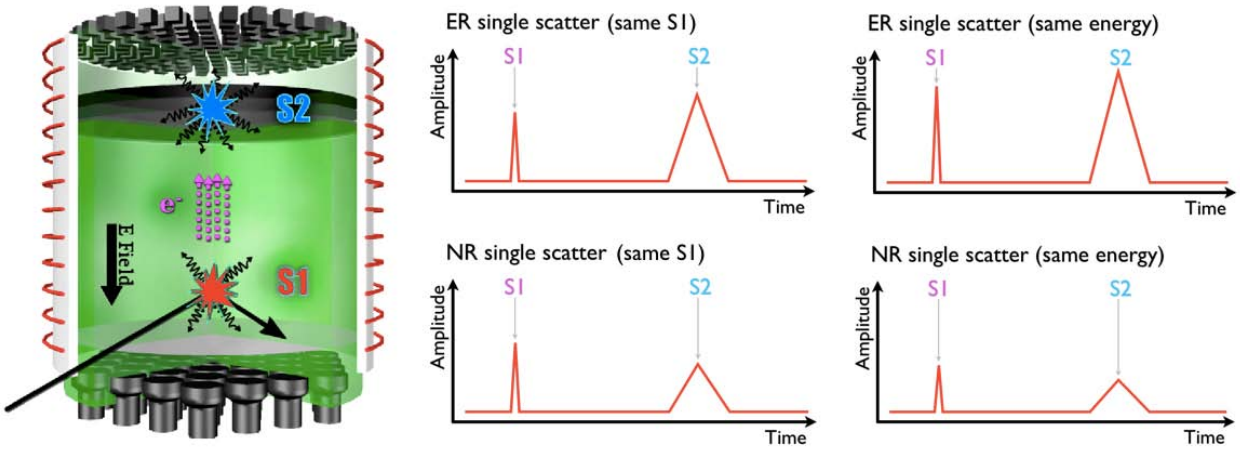

Figure 3.4.4: Schematic signal traces for electronic recoil (ER) and nuclear recoil (NR). Left: ER and NR events with equal S1 show the relatively lower S2 signal of NR events. Right: ER and NR events with identical energy shows the quenching effect felt by nuclear recoils (overall reduction of signal from kinetic energy lost to heat through the Lindhard factor [67]).

ionization. This behavior is the reason for significant differences between the target response to ER and NR events.

Firstly, the dressed recoiling xenon nucleus tends to bump into xenon atoms readily, losing energy via normal kinetic heat transfer. Recoiling electrons from ER events tend to only interact with other electrons, either ionizing the parent atom or exciting it. The NR events will do all three: atomic heat, ionization, and excitation. This means that the overall signal for a NR will be quenched (both S1 and S2) relative to an electron recoil of the same recoil energy. The quenching coefficient for NR signals is termed the Lindhard factor [67] (see Appendix A for a discussion of the signal quenching).

Secondly, the typical recoil path structure and length are different for an ER and NR of the same recoil energy. This behavior is captured in the fact that ER and NR events have different ionization densities. The ionization density in NR events is higher due to a more compact path structure originating from lower recoil velocities and frequent atomic interactions. It is important to note that ionization electrons found in high ionization density regions will be harder to separate with an applied electric drift field. This higher ionization density leads to higher recombination probability and is seen as a reduction in the S2-to-S1 ratio for NR events when compared with ER events. See Fig. 3.4.4 for a depiction of signals

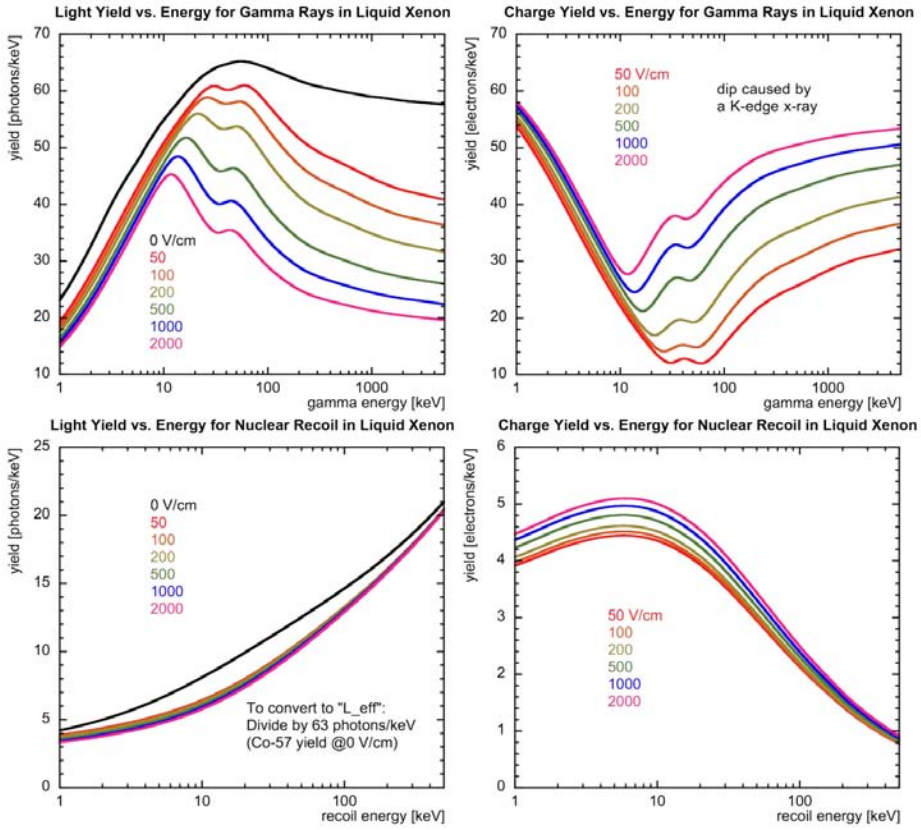

Figure 3.5.1: Top: Light and charge yield for various drift fields for gamma energy depositions (ER) in LXe. Bottom: Light and charge yield for nuclear recoils (NR) in LXe for various drift fields. Figures from NEST model in Ref. [68].

seen as a result both ER and NR recoils.

3.5 Signal Properties

In LXe there exists two types of recoils from the two particles which make up the target (electrons and xenon nuclei). The generation of signals from these recoils is discussed above, but the properties of the signals are detailed here. The signals are caused by discretized excitation and ionization within the LXe target with several parameters that govern the exciton/ion ratio, as well as the overall signal magnitude and variability. Particle type and energy, detector geometry, target cleanliness, and properties of the signal transducers all

play a role in this process.

3.5.1 Signal Quanta Yield

In a given interaction with a specified particle deposition type and energy, there will be a nearly constant number of signal quanta produced (see Refs. [60,68–70]). We define the work function for a quanta type as

$$W_{type} = \frac{E_{type}}{N_{type}},$$

where E_{type} is the deposited energy and N_{type} the number of quanta for a specific type. For LXe there are two types of quanta measured, the number of ions N_i and the number of decaying excitons N_{ex}. The work function W for both quanta types is difficult to measure, but defining

$$W = \frac{W_i + \alpha W_{ex}}{1 + \alpha},$$

where $\alpha = N_{ex}/N_i$, allows the equation to be written as

$$W = \frac{E_{dep}}{N_i + N_{ex}},$$

where $E_{dep} = E_i + E_{ex}$ is the total deposited energy, N_i is the number of ions, and N_{ex} is the number of produced excitons. This definition allows for ignoring the difference between the two work functions with no loss of generality. The general work function is taken to be $W = 13.7$ eV by Ref. [69].

This model allows for the reconstruction of events by estimating the number of ions N_i in the S2 signal and inverting the S1 signal to give the number of excitons N_{ex}. The energy deposited in an event can be estimated by rearranging the simplified equation to

$$E_{dep} = W(N_i + N_{ex}).$$

In Sec. 3.5.9.2, the partitioning of energy into charge and light is detailed to show the event-by-event anti-correlated signal fluctuation in dual phase LXe detectors.

3.5.2 Light Yield

As noted in Sec. 3.4.1, energy from a recoil will be deposited partially into excited xenon molecules. These excitons decay on the nanosecond timescale to give the 178 nm scintillation light typical of pure xenon material. The scintillation light yield of a dual phase xenon detector depends on the type of depositing particle and varies with the amount of energy absorbed. The light yield also varies with applied electric drift field for electromagnetic events especially, as discussed in Sec. 3.5.9.1. The light yield of the interaction Y is typically measured in units of photoelectrons per keV_{ee} and extrapolated to zero drift field. See Fig. 3.5.3 and Sec. 3.5.9.1 for a discussion of the light yield quenching effect from applied drift field.

3.5.3 Charge Yield

The charge (ionization) yield of a dual phase xenon detector also depends on the type of depositing particle and the amount of energy deposited. When an electric field is applied across the target volume, charge is able to be extracted and measured. For electromagnetic depositions, the charge yield grows as the applied electric field is increased due to the recovery of an increased number of ions which would otherwise recombine at lower fields. Eventually the boosted charge yield asymptotes to a maximum value at high enough applied fields O(5 kV/cm). See Fig. 3.5.3 and Sec. 3.5.9.1 for a discussion of the charge yield boosting effect from applied drift field.

3.5.4 Alpha Deposition

Energy deposits from alpha radiation have the highest ionization density and generally very large energies O(MeV). The high energy nature allows for efficient removal of background events but the high ionization density does offer an insight into liquid xenon microphysics

through the phenomenon of biexcitonic quenching [71]. Since ionization densities are extremely high in alpha depositions, the excitons that are produced will be in close vicinity and have a chance to form a biexcitonic state that only emits one photon, rather than the two photons that would be emitted from the original excitons. For normal ionization density (see Fig. 3.4.1), a pair of excitons would form two decay photons but for high densities the reaction can undergo biexcitonic quenching

$$\mathrm{Xe}^* + \mathrm{Xe}^* \rightarrow \mathrm{Xe} + \mathrm{Xe}^+ + e^-(\mathrm{K.E.}),$$

$$\mathrm{Xe}^+ + \mathrm{Xe} \rightarrow \mathrm{Xe}_2^+,$$

where the reaction continues down the recombination path to form only one photon. This results in a quenching of the S1 signal for very high ionization densities. For alphas, a reduction of scintillation signal of 77% is noted in Refs. [71, 72]. These effects, however, are unimportant for dark matter searches since alpha energy depositions are generally far out of the dark matter search window O(keV).

An additional phenomenon is of concern for a low energy dark matter search. Alpha particles can combine with several different materials to efficiently produce neutrons through the (α, n) reaction. An alpha can impinge upon the nucleus in the material, combine with the nucleus, and a resulting energetic O(MeV) neutron can be emitted. Neutrons emitted from (α, n) reactions inside the detector are particularly dangerous since they will not be moderated by a shield and would produce O(keV) energy NR scatters in the target. With this in mind, alpha emitters must be diligently cleaned from the surface of all detector and inner shield components.

3.5.5 Beta Deposition

Beta radiation is generally stopped well before it can enter the target volume. However, if the radiation originates in the target volume from radioactive isotopes within the LXe or on the surface of detector components, then the β radiation will be detected. If the beta is negatively charged the event will look identical to a pure electron recoil since the β^- is

equivalent to a recoiling electron. If the beta is positively charged β^+, it will quickly produce two back to back gammas after annihilation with a nearby electron.

The negative beta case can produce low energy signals which could contaminate the dark matter search energy window. If the β^- is part of a several body decay (as is the case with e.g. ^{85}Kr) that originates from a progenitor nucleus in the target volume, then the beta energy spectrum will be continuous down to very low energy and creep into the dark matter signal region. The β^+ is less of a concern since isotopes with positive beta emission are less common in the target, but also the high energy annihilation signature would allow removal of the event.

3.5.6 Gamma Deposition

Energy depositions due to gamma interactions are the most common background inside a dark matter detector. The majority of impinging radiation that makes it to the target volume is electromagnetic in nature and that of a high energy gamma. Typical interaction lengths are mm to cm (see Fig. 3.5.2), so the surface of the LXe target volume is highly populated with gamma events while in the central fiducial volume the number of gamma induced electron recoils is highly suppressed. The gamma induced electron recoils are generally due to photoabsorption or Compton scatters, with the Compton scatters usually serving as the source of low energy recoils. In addition to low energy beta depositions, as discussed in Sec. 3.5.5, a worrisome gamma event could nominally be caused by a higher energy gamma that scatters outside the TPC in an uninstrumented region, then finds its way into the TPC and gives up a final small amount of energy (events with this topology are termed gamma-X). The likelihood of gamma-X was estimated with Monte Carlo techniques during the detector design phase and proved to be a small but non-negligible background that must be reduced.

3.5.7 Neutron Deposition

Interactions sensed by the dual phase detector due to neutron events are of particular interest. Neutron interactions provide a calibration tool for probing WIMP-nucleus interactions since the neutrons elastically scatter to produce NR in the target, mimicking a WIMP elastic

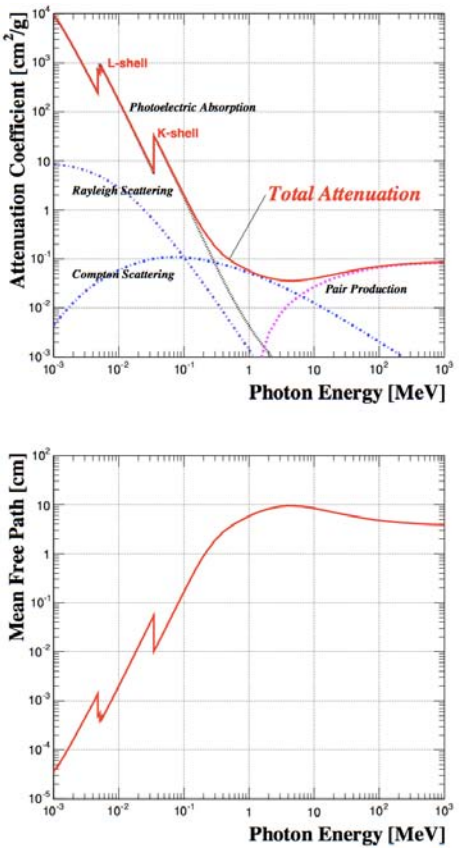

Figure 3.5.2: Top: Attenuation coefficient of gammas as a function of energy [73]. The contribution from Compton and Rayleigh scattering is included as well as pair production and dips from the liquid xenon L and K-shell edges. Bottom: Gamma mean free path as a function of energy. Gammas of lower energy have dramatically lower mean free paths, giving them far less penetrating power.

scatter precisely. The nuclear recoil nature of neutron events makes them nearly indistinguishable from a WIMP-nucleus interaction. The only way to distinguish a neutron-nucleus scatter from a WIMP-nucleus interaction is by searching for multiple scatters, which frequently happen with impinging neutrons but will never happen with a WIMP. The multiple scatter identification of neutrons becomes more effective with larger detector volumes since the interaction length for neutrons is around current detector length scales O(10 cm).

Events caused by neutron scattering are an example of the NR energy deposition type described in Sec. 3.4.3. Neutron events will produce elastic recoils which fit squarely into the

NR band but also inelastic recoils which result in a mixed event, one with both an ER and NR component. These inelastic events are easily tagged and particularly useful for producing a signal correction map throughout the detector volume (see Sec. 7.2.2). Events of similar topology to gamma-X (see Sec. 3.5.6) can occur with neutrons as well. The neutron-X events are a negligible WIMP search background, but must be taken into account when doing neutron calibrations.

3.5.8 WIMP Deposition

Energy depositions from WIMP-nucleus interactions are the desirable signal for rare event detectors in search of dark matter. An impinging WIMP is expected to interact only with target nuclei (as opposed to the electrons surrounding the nucleus) via an elastic scatter. The recoiling nucleus then deposits observable energy into the detector by the production of the excitons and ionization. All NR events suffer an overall quenching of the number of signal quanta due to heat loss, and WIMP interactions are no different. The unique partitioning of signal quanta into the light and charge channels allowing the NR events to be distinguished from electron recoils (ER), as discussed in Sec. 3.4.3. This means signals produced by alpha, beta, and gamma radiation can be rejected using the charge-to-light ratio, revealing the WIMP-like NR signal present in the detector.

The recoil will have an identical event by event response to that of a neutron elastic recoil. The S1 and S2 signals will be quenched in an identical manner to that of neutrons, so scattering neutrons can be used to calibrate the signal region (see above Sec. 3.5.7). The identical nature of the neutron and WIMP signals requires that the neutron signal be severely minimized during the WIMP search (see the background discussion in Ch. 6). This type of recoil is the signal sought after in the search for WIMPs. If an excess of nuclear recoils is found in a WIMP search, physicists get optimistic about a detection. If the detected energy spectrum is similar to that expected of WIMPs, then a positive detection is likely.

3.5.9 Signal Variability

During a WIMP search, one must allow for the fact that at low energy the signal will vary considerably (even at well defined recoil energies) and consider the implications of

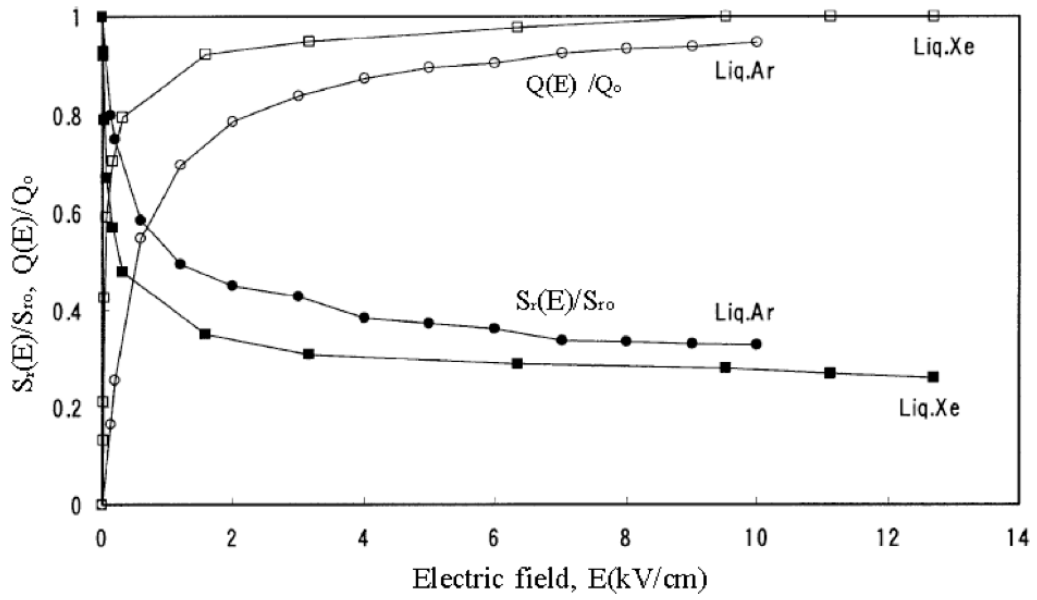

Figure 3.5.3: Charge and light signal dependence on electric field for both LXe and LAr dual phase detectors [72]. As the electric field is increased, ionization collection grows and eventually asymptotes while light signal drops complementarily. The behavior is due to ionization electrons being collected rather than forming an additional S1 recombination signal.

this behavior during the data analysis phase. Several sources of signal variability come into play but some only crop up due to detector parameters, like the S1-S2 anti-correlation due to S1 quenching. Sources of signal variability in this category will not change their effect over a run as long as the detector parameters determining their behavior are held constant. Other sources of variance happen on an event-by-event basis, like the S1-S2 anti-correlation due to varying exciton-ionization ratio creation, geometric induced fluctuations, and photomultiplier response. These must have their effects corrected for or accepted as an inherit property of the detector which cannot be ameliorated.

3.5.9.1 Signal Quenching Anti-correlation

Average S1 and S2 signals in LXe vary in response to an electric field applied to the target volume. As the magnitude of the field grows, the overall S1 signal is reduced while the S2 signal is boosted. S1 signal quenching is a result of ionization electrons being transported

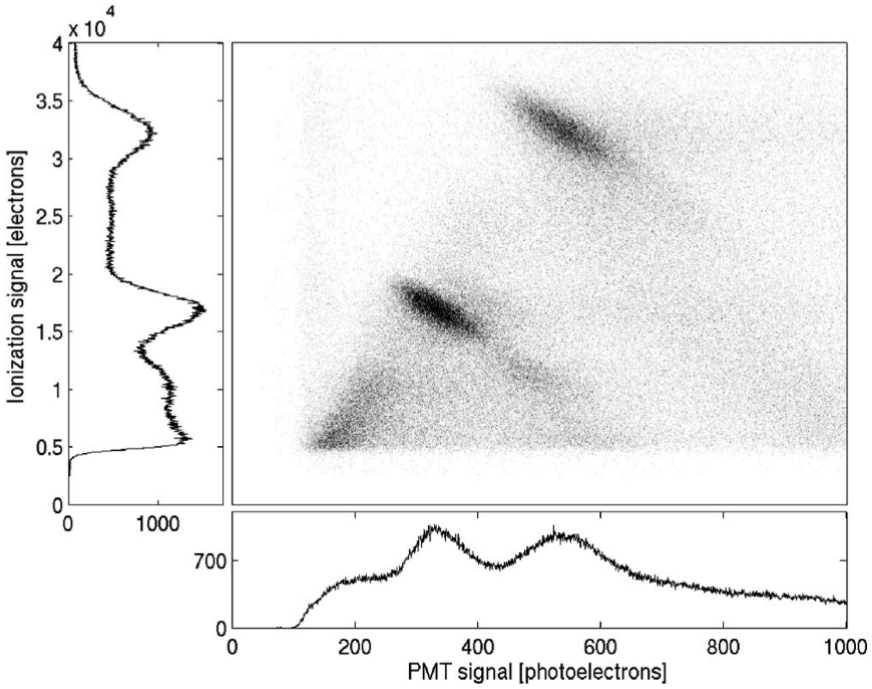

Figure 3.5.4: Data from ^{207}Bi energy deposits of 570 keV$_{ee}$ and 1064 keV$_{ee}$ in a dual phase LXe detector with drift field of 4 kV/cm [75]. A clear anti-correlation of S1 and S2 signal is seen in the peak energy depositions caused by a constant quanta count (E/W) but varying exciton-ion fraction.

away from their respective ionization sites by the drift field (see Sec. 3.4.1.1 for S1 generation discussion). At lower fields, a greater number of ionization electrons will recombine but higher fields more readily remove these ionization electrons from the interaction region to become free drift electrons. The amount of quenching is particularly high in the case of electronic recoils due to electrons having high recoil velocity O($0.1c$), hence low ionization density. Nuclear recoil ionization density is considerably higher since it has such low recoil velocities O($10^{-4}c$) which results in nearly field independent S1 and S2 signals [74] (see Fig. 3.5.3).

3.5.9.2 S1-S2 Anti-correlation

Anti-correlation of the S1 and S2 signals produced by a monoenergetic source will occur on a per event basis (likewise for an energy spectrum). This anti-correlation results from

several sources. Firstly, there is a variance in the ratio of the number of xenon excitons and ionization that take place due to stochastic nature of the tracks. The fraction of ionization electrons that eventually escape to become ionization electrons varies stochastically as well. With this is mind, the S1 signal for a given energy will vary along with the S2 signal, but they will be heavily anti-correlated since the initial number of ionization electrons and excitons is well determined by the deposited energy within an uncertainty of the LXe Fano factor (a measure of the physical fluctuation of quanta produced by an energy deposition [58]). In S2 vs. S1 space, this is apparent as a heavy anti-correlation for monoenergetic energy depositions, but the correlation happens at all energies (see Fig. 3.5.4 and Refs. [76–78]).

3.5.9.3 Geometric Fluctuation

All physical quantities are measured by transducing photons which make it to the PMT. There is inherent fluctuation in the measured signal strictly from geometric effects since less than unity reflection coefficients and a finite photon propagation length through the target media will cause variation in the number of photons reaching the PMTs [73]. A photon may be absorbed by the teflon reflector rather than striking a PMT directly, deflected through Rayleigh scattering, or it may be absorbed along its path by impurities in the xenon. Although the reflection coefficient of PTFE (Teflon) in LXe is very high, greater than 95% [79], and the absorption length for a photon is on the meter scale, the aggregate of these effects is still apparent. The low energy region is affected most by these fluctuations since a low number of detection quanta will more readily fluctuate. The variability at very low threshold restricts ER/NR discrimination ability and ultimately reduces the nuclear recoil acceptance sharply in the low energy region.

3.5.9.4 PMT Response Fluctuation

Adding to the geometric fluctuation mentioned above, the signal transducers themselves will introduce a large fluctuation of signal at low energies. This variance is caused by the characteristically large width of the single photoelectron peak from PMTs coupled with the $\approx$30% quantum efficiency. The quantum efficiency of a PMT will throw away most impinging photons due to physical limitations of the photoelectric effect in the photocathode. Only

around 30% of impinging photons will produce a photoelectron which is then amplified by the PMT.

The width of the single photoelectron peak is the result of stochastic effects caused by amplification signal generation inside the PMT. The photoelectron emitted from the photocathode after a photon impact is accelerated until impacting the first dynode. A statistically determined number of electrons will then be emitted from the first dynode due to the collision, and be accelerated down the chain for more amplification at other dynodes. The large variance in the production of electrons in the first few dynodes induces a large (and difficult to reduce) variance in the signal area O(0.25-0.50 PE/PE). The same variance applies to individual photoelectrons generated in a large aggregate photon signal, but as the signal area gets larger the percent variance gets smaller with the common resolution dependence $\propto \sqrt{\text{signal}}$.

CHAPTER IV

MiX: A Position Sensitive Dual Phase LXe Microphysics Probe

Studying small scale dual phase liquid xenon detectors allows for rapid research and development in LXe technology and can later be applied to dark matter experiments. One such experiment, the Michigan Xenon (MiX) detector, was constructed at the University of Michigan to study the microphysics of liquid xenon across a large energy range. The goal of the experiment is to construct a fully operating, reliable dual phase xenon detector with very high light yield and three dimensional position sensitivity. The easily managed system allowed for considerable understanding of cryogenic operation at 180 K and system handling via slow control. The supporting xenon handling system was constructed and commissioned in 2012, dual phase detector operation was established with initial testing in 2013, and a detector upgrade with serious analysis effort was undertaken in 2014. Developing a small scale dual phase detector with topology very similar to PandaX-I has proved useful in operating PandaX-I efficiently.

4.1 System Description

The MiX system consists of a cylindrical inner vessel (6" diameter, 12" high) housing a detector that is supported by an array of electronics, cryogenics, and gas handling equipment. The inner volume is hermetically sealed and wrapped in a stainless steel vacuum jacket to reduce heat load on the chilled inner volume. Gas lines supply a heat exchanger with

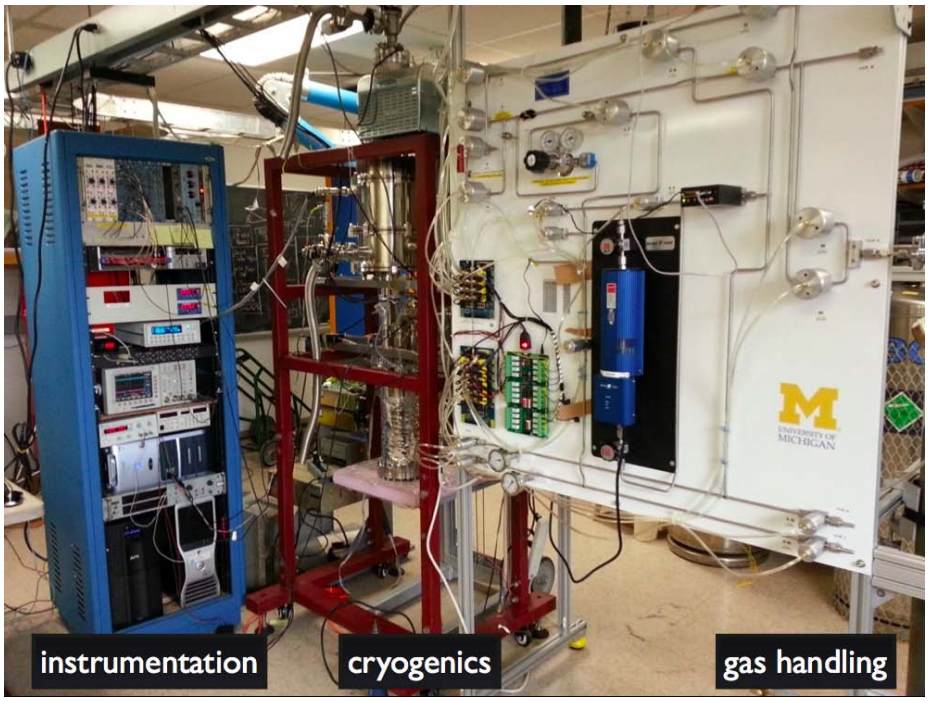

Figure 4.1.1: A photograph of the three main systems of the MiX experiment. Left: The slow control system, high voltage sources, signal handling, and data acquisition are housed in a rack. Center: The cryostat houses the LXe-filled detector and maintains cryogenic temperatures. Right: The gas handling system stores unused xenon and purifies the LXe using a pump and hot getter.

circulating, purified gaseous xenon (GXe) which recondenses the incoming gas and boils the outgoing liquid. The cooling power is supplied by a 24 W Joule-Thomson cooler, ARS MRCM-150-1, which is coupled to the inner volume by an indium sealed copper condenser. The cooling head is maintained at LXe temperature to allow for GXe condensation on the head. The condensed LXe gravitationally funnels down to the inner vessel where it cools the detector region. A gas panel with storage bottles houses GXe and maintains a constant flow of purified xenon by pumping GXe from the inner vessel through a hot getter, then back to the cryostat via a heat exchanger. High voltage feedthroughs allow passage of external high voltage into the detector for the operation of photomultiplier tubes and time projection chamber electrodes. Low voltage feedthroughs transport information about the state of the detector (such as liquid height and temperature) to the slow control system. A fiber optic feedthrough sends optical photons into the inner chamber for the calibration of the

photomultiplier tubes.

The MiX detector is a 4+1 PMT high light yield (low energy threshold), dual phase design. Four square top PMTs (Hamamatsu R8520-406) are closely packed on the top surface of the cylindrical detector. A single bottom PMT (Hamamatsu R11410-MOD) is situated on the bottom of the sensitive volume cylinder, with the photocathode as the entire bottom surface. The diameter of the sensitive volume is 63.5 mm (2.5") with a TPMT to BPMT height of 48 mm. The TPC electric field generation scheme only uses four electrodes, a grounded anode grid, negative gate grid O(-5 kV), negative cathode grid O(-5 to -10 kV), and a grounding ring to protect the bottom PMT in the event of a cathode discharge. The anode, gate, and cathode are fine-pitched hexagonal meshes that provide an equipotential surface while allowing 95% optical transmission. The ground ring is kept just outside the sensitive volume and allows 100% optical transmission.

4.1.1 Cryostat

A cryostat houses the detector, keeping the contents in a low heat-load environment to allow effective cooling of the interior. The stainless steel design features a vacuum jacket surrounding a hermetically sealed inner space which holds gaseous and liquid xenon. The cryocooler and heat exchanger are also encapsulated by the vacuum jacket. Feedthroughs which allow access to vessels populate convenient locations around the cryostat.

4.1.1.1 Outer Vessel

A vacuum jacket surrounds the interior of the cryostat to decouple the interior volume from external heat sources. A schematic of the cryostat is shown in Fig. 4.1.2. The interior of the outer jacket is evacuated to 10^{-5} torr which reduces convective heat load. Layers O(10) of superinsulation occupy the space between the inner and outer vessel surfaces to minimize infrared heat load. A ten-pin conflat (CF) feedthrough enters the outer vessel to allow electrical interface with the cryocooler heater and temperature sensor.

4.1.1.2 Inner Vessel

A stainless steel cylindrical volume measuring 15.3 cm (6”) in diameter and 30.6 cm (12”) in height is the main containment space for the MiX detector. Four vacuum-jacketed conflat feedthroughs allow direct access to the inner vessel (2x1.33”, 1x2.125”, 1x2.75”). The inner vessel is connected to a downtube which leads to the condensing head. A drip funnel collects liquefied xenon from the condensing head and transports it through the downtube to the inner vessel. Figure 4.1.2 depicts both the outer and inner vessel of the cryostat.

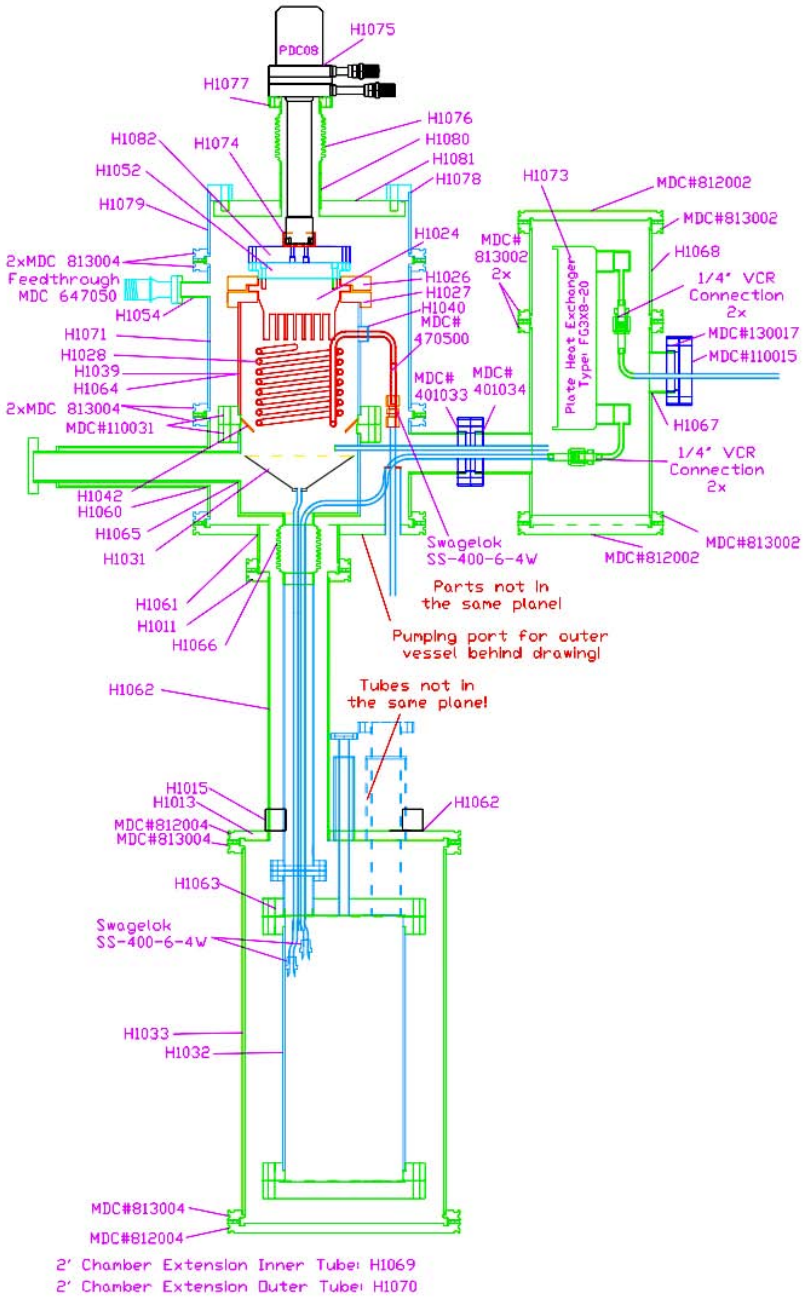

Figure 4.1.2: A schematic of the MiX cryostat. The inner vessel (H1032) is located at bottom with a cooling head (H1024) at top. The heat exchanger (H1073) is located at right. The system is a custom vacuum-jacketed stainless steel arrangement which ensures a low heat load. Design and drawing courtesy of Karl Giboni.

4.1.1.3 Cryocooler

A Joule-Thomson cooling head (shown in Fig. 4.1.2) is employed to remove heat from the system. A compressor supplies room temperature high pressure gas to the cooling head. The gas expands and cools a copper condensing head which couples the cryogenic head to the inner vessel volume. The condensing head is finned to increase the surface area for condensation. A PT100 platinum resistor temperature sensor is attached to the condensing head with thermal epoxy to monitor the head temperature.

The cryocooler supplies a constant cooling power which must be moderated by a heat source to maintain a constant temperature. For this purpose, two parallel resistive heating elements are embedded on the vacuum side of the condensing head to provide active heat flow into the condensing head. A Lakeshore temperature control unit employs a feedback control loop which monitors the head temperature and supplies variable heater power. The temperature is maintained within a tenth of a Kelvin for months at a time.

4.1.1.4 Heat Exchanger

Circulating xenon must be warmed from the liquid state, pumped through the getter (see Sec. 4.1.2.5), then recondensed and deposited into the inner vessel once again. This process is highly inefficient if a heat exchanger is not used to provide coupled liquefaction and evaporation. The heat exchanger brings the warm incoming gas into thermal contact with liquefied xenon, simultaneously evaporating the liquid and condensing the gas at greater than 90% efficiency. The heat exchanger used in MiX is a commercial plate unit that is housed in the cryostat vacuum jacket (similar to Ref. [80]). The heat exchanger unit is shown in Fig. 4.1.2.

4.1.2 Gas Panel

Effective gas storage and handling for the system is achieved through the use of a custom gas panel with several subsystems. The main panel is 1/8" aluminum mounted to an 80/20 frame with stainless steel 1/4" lines and VCR connections to form the gas pathways. The construction of this panel allows flexible, clean handling of xenon gas during liquefaction,

normal operation, and recovery of the liquid xenon. The panel, depicted in Figure 4.1.1, and subsystems are discussed below.

4.1.2.1 Pneumatic Valves

Eighteen Swagelok low and high pressure pneumatic valves are activated by an electronic relay board. The relay board is controlled through a serial-USB interface with the slow control computer to allow computer control. A custom graphical user interface (GUI) was developed to allow for visual valve state confirmation and individual valve control. The valves default to a normally closed configuration in the event that USB connection is reset or the power is cycled. The computer control allows for remote operation of the panel if necessary and automatic valve control in case of an emergency.

4.1.2.2 Flow Controller

A Hastings flow controller (HFC-D-302) allows for metering the xenon flow during filling and circulation. The flow rate can be controlled via slow control GUI input but achieves maximum flow when in the non-control loop purge mode. The meter tracks flow rate in standard liters per minute (SLPM) in both forward and backward directions and was calibrated for dry nitrogen gas, not xenon. A correction factor can be used to scale from nitrogen to xenon flow rates.

4.1.2.3 Storage Bottles

Two aluminum storage bottles are used to house the gaseous xenon when not in use. The bottles are hung from load cells (Interface Mfg. 1500ASK-200) which are read by the slow control system to track the contained mass. The bottom of the hanging bottles can be submerged in a bath of liquid nitrogen to cryopump xenon into the bottle. High pressure flexible VCR lines connect the bottles to the gas panel to accommodate coupling flex.

4.1.2.4 Pump

A MX-808ST-S pump is installed in the gas panel to provide the circulation necessary for purification. The pump is a diaphragm model which minimizes outgassing to the gas-side volume, keeping the xenon as clean as possible. It can withstand a pressure of 45 psia but must be started before a pressure of 25 psia is reached to ensure proper starting of the motor. The maximum flow rate induced by the pump while purifying LXe in the MiX system is about 6 SLPM.

4.1.2.5 Getter

A hot getter (SAES PS3-MT3-R-1) is installed in the panel to purify the xenon of electronegative impurities. The internal zirconium alloy getter cartridge is held near 650 K. Gas is forced through the cartridge while impurities collect on the highly reactive surface. The impurities in the outflowing gas are reduced to below the ppb level. The getter regulates its temperature and will notify the user in case of a fault.

4.1.3 Slow control

A slow control system (SCS) was developed by Michael Schubnell at University of Michigan for both the MiX and PandaX-I systems. The Python based software tracks slow parameters of the system in a SQL database and allows for control of several aspects of the experiment.

4.1.3.1 Pressure

The inner vessel pressure is monitored in two places while operating. A pressure transducer sits in a location far from moving gas to give a static reading of the inner vessel gaseous xenon pressure. Additionally, a pressure sensor is located before a small buffer volume on the low pressure gas line which emerges from the heat exchanger. The difference between the two pressures gives a measure of the health of the pumping state.

4.1.3.2 Temperature

Temperature is monitored in two places in the cryostat. One temperature sensor is situated between the cryocooling head and condensing head, as mentioned in Sec. 4.1.1.3. A second PT100 is located at the bottom of the inner vessel to monitor the LXe temperature. The lead to this sensor is routed through a thin PTFE tube to act as an electrical insulator near the TPC high voltage planes. Both sensors are measured using the four wire technique with a Lakeshore temperature controller. The Lakeshore setpoint and heater power are also sampled with the slow control system.

A final temperature sensor is located external to the system to monitor the room temperature atmosphere around the detector. A DS18B20 temperature sensor is attached to a DLP-TEMP-G USB board via a custom ethernet cable which locates the ambient temperature sensor away from heat sources. The slow control system regularly logs the room temperature to allow for temperature correlation studies of detector parameters.

4.1.3.3 Monitoring

Slow quantities besides the crucial temperature and pressure values are logged as well. Bottle mass, LXe height, server status, flow rate and status all can be monitored for faults and action can be computationally triggered if necessary. Email and SMS notifications are sent when alarms are triggered or emergency control can be set into motion, as is discussed in the following sections. Additionally, a web accessible server is maintained to allow personnel to remotely monitor the crucial system quantities.

4.1.3.4 Control

The slow control system is able to take command of several subsystems in the MiX experiment if necessary. The gas panel pneumatic valves can be manipulated with the GUI control discussed in Sec. 4.1.2.1. The valves can be controlled by events triggered in the slow control software. Additionally, the target temperature can be controlled on the Lakeshore device by changing the setpoint remotely through the SCS. The flow controller can be sent a fully-opened, fully-closed, or a closed loop target flow rate command.

4.1.3.5 Emergency System

An emergency system is in place to provide necessary cooling should a failure be encountered during normal operation. The SCS controls a relay board which can energize a normally closed cryogenic valve situated on an emergency LN_2 dewar. When the relay is switched closed, the valve will open and allow liquid nitrogen to flow through a coil attached to the condensing head. The SCS system can automatically activate this subsystem if the inner pressure elevates beyond a set threshold and deactivate if the pressure is brought back to normal.

Since the emergency LN_2 system is coupled to the coldhead, the system can be repurposed in the initial xenon liquefaction phase to shorten the cooling time. Using this technique, liquefaction can take place at about 4 kg/hr, filling the MiX detector in about two hours. The LN_2 assist can then be used (with personnel oversight) to shorten the time until purification is stable by helping to cool down the heat exchanger during the initial circulation. With the emergency system assistance the MiX LXe can be filled, circulating, and stabilized within 6 hours. The emergency system is then put back into backup cooling mode.

4.1.4 Detector

The MiX detector is a dual phase liquid xenon detector with three dimensional position reconstruction abilities. Liquid xenon partially fills a sensitive volume that is instrumented with several PMTs and surrounded by a reflector for VUV photons. Radiation based energy deposits in the liquid produce a prompt scintillation flash (S1) along with ionization near the interaction vertex. Electrodes draw an electric field across the liquid volume to allow for collection of the ionization electrons at the gas/liquid interface. The drifted electrons are then extracted and accelerated across a small gas gap to give a secondary scintillation flash (S2) which is proportional to the amount of charge produced at the initial interaction vertex. Both the S1 and S2 signals are sensed by the PMT devices and a time series of each PMT waveform is recorded upon an event trigger. The design was optimized through Monte Carlo methods using the GEANT4 [81, 82] library. A visualization of a 10 keV_{nr} event in the MiX geometry is shown in Fig. 4.1.4. For a detailed discussion of the signal properties in liquid xenon, see Chap. 2.1.3.

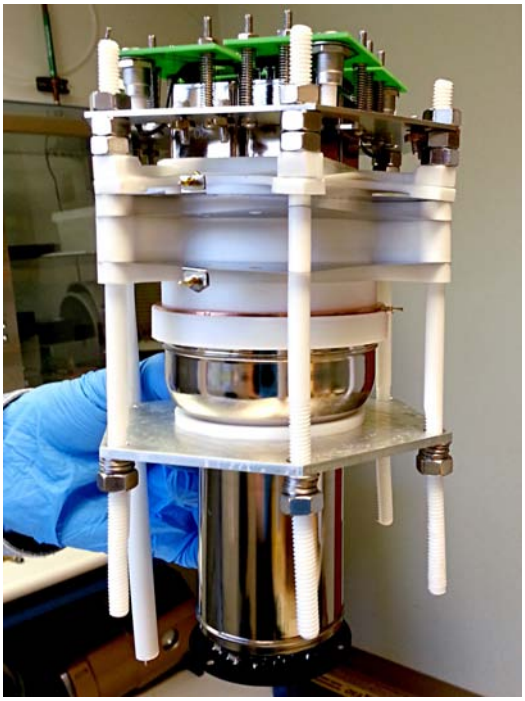

Figure 4.1.3: A photograph of the fully assembled MiX time projection chamber. Four 1" PMTs with custom bases are located at top with a single PMT with Cirlex base at bottom. A cylindrical PTFE reflector encloses the sensitive volume while chemically etched electrode grids define the drift and extraction regions. The high light yield detector is designed to image events in the sensitive volume with energy and 3-dimensional position reconstruction abilities.

The various subsystems which allow operation of the detector are discussed in this section. High vacuum components, both commercial and custom, have been utilized in the construction of the detector. High voltage systems to operate the light sensors and time projection chamber and a vacuum UV (VUV) PTFE reflector are employed. The MiX detector components are outlined below.

4.1.4.1 Feedthroughs

Custom and standard feedthroughs have been used to transport electrical and optical signals between the cryostat interior and the external systems. Two standard MPF ten pin feedthroughs with 1.33" CF flanges carry low voltage in and out of the detector; one for the

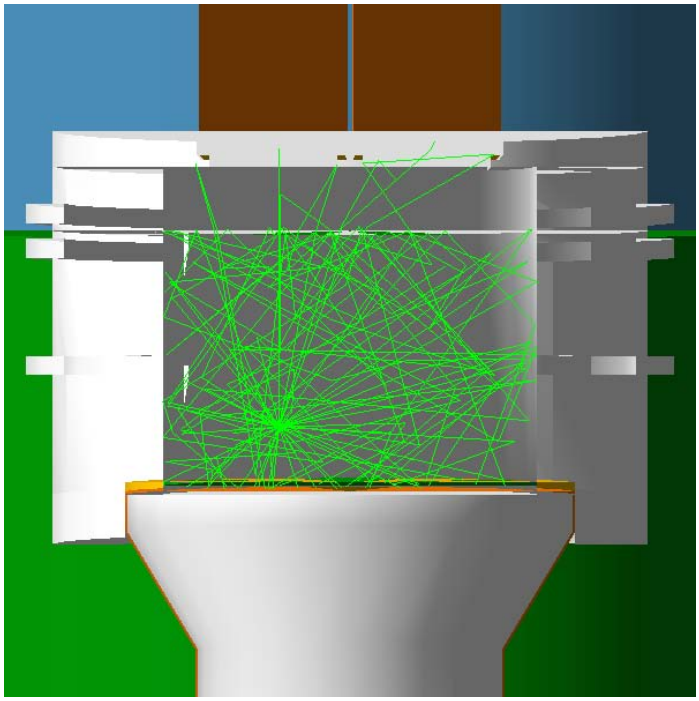

Figure 4.1.4: A representation of a simulated event in the MiX detector. The detector geometry was optimized through Monte Carlo methods using the GEANT4 [81, 82] and NEST [68, 69] libraries. This particular event represents a background 10 keV$_{nr}$ deposition below the cathode.

cryogenic head located in the outer vacuum and another for the inner vessel temperature sensor and level meter. Two standard four connector SHV to vacuum BNC (non-standard BNC) feedthroughs are used to transport the PMT high voltage and signals between the inner vessel and outside world. The SHV-BNC and inner vessel ten pin feedthroughs are mounted to a CF cross and elbow to allow for all PMT, temperature, and level sensor cabling to enter the inner vessel through a single 2.75" CF flange.

A custom fiber optic feedthrough was constructed to cleanly transport optical photons from a pulsing LED into the inner vessel. Two modified MDC high voltage 20 kV 1.33" CF single electrode feedthroughs bring in cathode and gate high voltages. A teflon sleeve and thin nickel connection rod were added to allow for cable attachment on the single electrode feedthroughs. The custom high voltage feedthroughs were tested to positive and negative 30 kV with no breakdown in air.

Figure 4.1.5: A photograph of the custom SHV-BNC feedthrough connectors and cabling used in MiX. Standard vacuum BNC connectors breakdown readily in gaseous xenon above O(1 kV). The connectors and cabling were produced in-house to allow for transport of the high voltages necessary for the PMTs. Connector design courtesy of Curtis Weaverdyck.

4.1.4.2 Cabling

Feedthroughs for the inner vessel do not pass through the vacuum jacket, but interface directly with the inner volume. Single strand 30 kV Kapton cables with UHV connectors were used for the cathode and gate high voltages. Gold plated connectors fit onto gold plated pins which are fitted to their respective grids. Kapton KAP3 cables were fabricated with in-house designed vacuum BNC connectors and high voltage LEMO quick connectors. Shielded vacuum cabling connects to the ten-pin feedthrough with UHV connectors and terminates at the two level meter connectors and a thin twisted four wire set similarly connects to the inner vessel temperature sensor. The outer vessel ten-pin feedthrough utilizes UHV connectors with Kapton insulated cables to connect to the cryocooler heating element and temperature sensor with soldered connections.

Figure 4.1.6: A photograph of the chemically etched mesh used for all electrodes in the MiX TPC (anode shown). The 50 μm-thick mesh has a central 76 mm circular region with hexagonally packed grid structure. The hexagons are created at a 2 mm pitch with 50 μm diameter wires to allow for homogenous TPC field generation while maintaining 95% optical transparency.

4.1.4.3 Grids

A chemically etched stainless steel grid was custom designed for the MiX detector in-house and manufactured by Great Lakes Engineering. The two-dimensional grid plane has a 50 μm (2 mil) thickness of hexagonal shape. A central 76 mm (3") circular region has 2 mm pitch hexagons surrounded by 50 μm (2 mil) width chemically etched wires. The packed hexagonal structure was selected for MiX since it offers the highest spatial uniformity of electric field for a given optical transparency (95% in this case). Figure 4.1.6 shows the custom hexagonal grid installed as the anode of the MiX detector. The gate and cathode grids are the same hexagonal grid design. Gold plated connectors thread through and clamp a bent stainless steel tab to provide the electrical connection seen in Fig. 4.1.7.

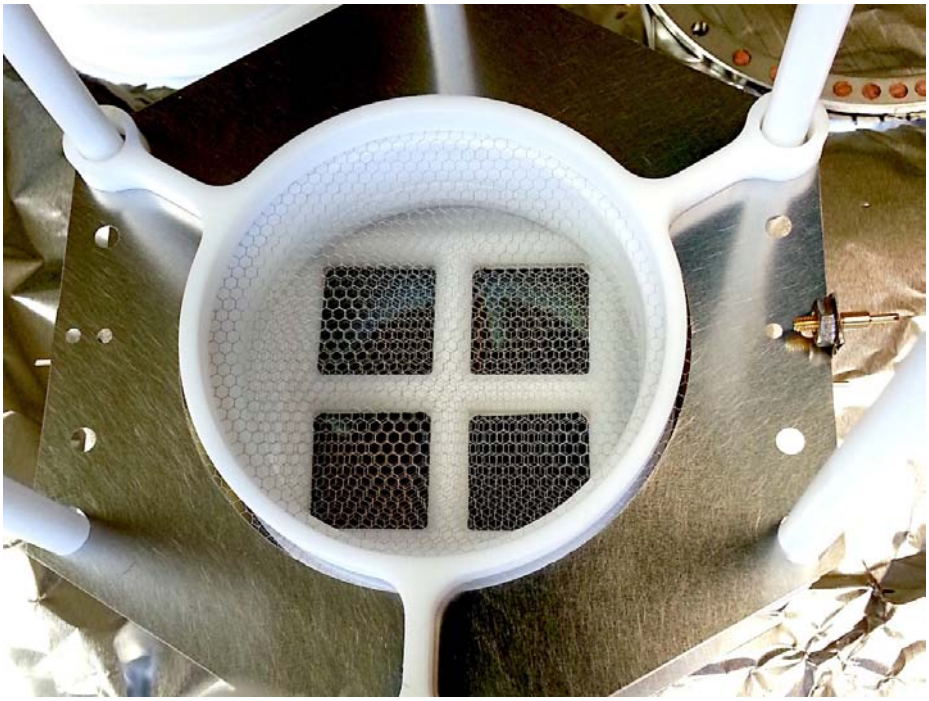

Figure 4.1.7: A photograph of the MiX reflector with all three TPC electrodes in place. The hexagonal meshes define equipotential surfaces from which uniform electric fields are generated in the sensitive volume. The reflector provides greater than 95% reflection of photons produced in xenon scintillation, greatly increasing the detector's light collection efficiency.

4.1.4.4 Reflector

The sensitive volume is surrounded by a cylindrical virgin PTFE reflector with portions removed to accommodate the top and bottom PMT photocathodes. The stacked structure of the PTFE reflector allows for insertion of the three mesh grids and ground ring electrodes between the PTFE layers. Reflectors constructed of virgin PTFE are greater than 95% reflective for VUV wavelengths. The PTFE pieces were machined with CNC techniques to achieve a 4 mm wall thickness for high reflectivity properties, but low PTFE mass. The reduction of PTFE mass in the time projection chamber allows for minimization of multiple neutron scatters when irradiated with calibration neutrons.

The reflector assembly is machined to fit tightly together so as to properly reflect photons back into the PMTs. However, this tight fit does not allow inherently easy flow of cleansed

LXe into the sensitive volume. Accordingly, a series of 3 mm diameter holes were drilled radially in the bottom PTFE reflector ring to allow free flow of clean xenon into the TPC.

4.1.4.5 Photomultiplier Tubes

Four square Hamamatsu R8520-406 PMTs are placed on the top of the detector volume. The TPMTs sit in gaseous xenon about 8.25 mm from the anode grid and 11.25 mm from the liquid/gas interface. They are tightly packed with only 2 mm between TPMTs and necessitated the construction of a custom base. The MiX TPMT base was designed and assembled at University of Michigan and features a high voltage LEMO receptacle and voltage divider circuit with charge storage capacitors (see Fig. 4.1.8).

A single circular Hamamatsu R11410-MOD is the final PMT in the detector. The bottom PMT photocathode makes up the entire bottom surface of the sensitive volume. The BPMT base is a Cirlex voltage divider with charge storage capacitors and a custom gold plated pin connector for the Kapton cable.

The PMTs are operated using positive high voltage supplied by low ripple PMT power supplies (FAST ComTec NHQ-203M). Gain calibration of all MiX PMTs is discussed in Sec. 4.2.1. The PMT bias voltage is selected based on the energies that are being probed by the detector. If looking for high energy events, the PMT gain can be lowered to reduce PMT saturation effects. If observing low energy events, the PMTs can be increased to a gain of about 4×10^6 to achieve the lowest energy threshold.

4.1.5 Data Acquisition

The PMT signals are decoupled from high voltage, fed into analog signal handling, and finally into the data acquisition system (DAQ) to digitize the waveforms. The PMT voltage signals are fanned out into a trigger logic system which can impose a number of trigger conditions. Once triggered, the fast analog-to-digital converter (FADC) of the DAQ capture the sampled PMT waveforms and save them to a disk array.

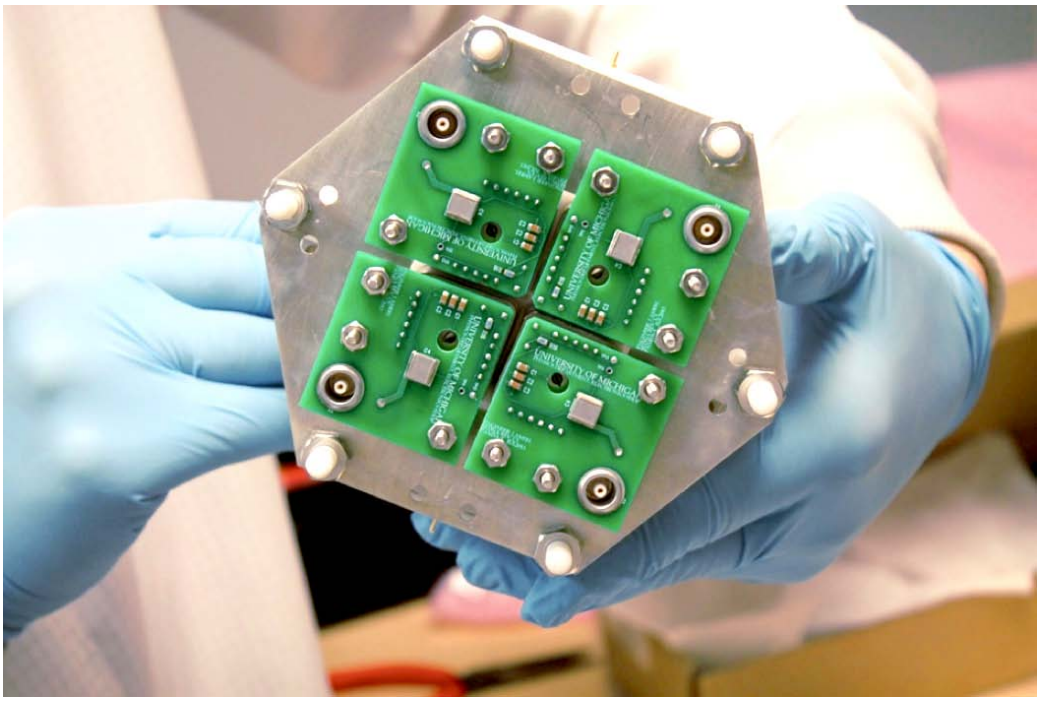

Figure 4.1.8: A top view photograph of the assembled MiX detector. The TPMTs are mounted with spring preloaded fasteners to the top aluminum plate. Custom bases were designed to provide both the physical mounting and voltage divider circuit for the TPMTs. A high voltage LEMO connector is used on the custom TPMT cables, allowing for quick disconnect of the base HV.

4.1.5.1 Decoupler

The high voltage line to each PMT is at positive high voltage and attached to the anode of the PMT. The voltage on the line remains high throughout all normal operating conditions, but signals are also carried on the line. The signals on the high voltage line are caused by large populations of electrons which collect on the anode after a light pulse. The signals cause the high voltage to drop by a few mV to at most a few volts. These signals must be decoupled from the O(1 kV) voltage being carried on the PMT cable.

A custom rackmount eight channel decoupler was constructed in a closed 2U aluminum unit. The front features low voltage LEMO connections and the back has two SHV connections for each channel, one for the power supply input and the other for the PMT supply. Each channel decoupler is wired internally to a standard resistor plus capacitor decoupler circuit.

An additional resistor is added to ground stray transient high voltage on the signal side.

4.1.5.2 Analog Signal Handling

The decoupled PMT signals are fed into NIM modules which split the signals and generate logic pulses based on chosen conditions. A LeCroy 428F fan in/out module fans out the PMT signal, allowing the signal to be duplicated. A copy of each PMT channel is sent into another LeCroy fan in/out module which is used as a fan in to sum the signals into a TPMT sum and total sum. An additional copy is sent to a LeCroy 612A 10x linear amplifier and LeCroy 821 octal discriminator to allow for triggering on PMT signals down to about -3 mV. A final copy of the PMT signal for each channel is piped to the FADC module in order to digitize the waveform once triggered.

Additional NIM logic is employed to handle the LED pulser triggering and signal splitting. A BNC 8010 pulser generates an adjustable 0.5-4 V pulse of width of 10-80 ns at a frequency of about 3 kHz. A Phillips 740 fan in/out duplicates the LED signal so it can be fed to both an LED and edge discriminator. The fanned out LED pulse is sent to the LED which causes the LED to emit a brief pulse of photons when the voltage pulse is present. Also, a discriminator branch of the fan out allows for precise triggering on the LED pulse across all pulse voltages.

4.1.5.3 Trigger Logic

Several trigger logic circuits are maintained to allow for efficient triggering in different analog based scenarios. Threshold triggers are set up for the TPMT sum, total sum, and individual channels, allowing for data acquisition based on signal size with edge discrimination. The minimum threshold for each is around -30 mV but with a 10x linear amplifier stage beforehand the threshold can reach -3 mV. An additional setup is created by sending the total PMT sum into a spectroscopy amplifier (Tenelec TC243) to be integrated and the output discriminated (LeCroy 623B) to produce a charge based trigger. A width based trigger is created by feeding the PMT sum into an updating discriminator (LeCroy 821) to produce a logic pulse whose width is identical to the width of the underlying pulse. This logic pulse is then integrated with a spectroscopy amplifier and discriminated to finish the width based

trigger. A final NIM-based trigger mode is achieved by using a discriminated LED pulse to generate the trigger logic pulse, as noted in Sec. 4.1.5.2.

Additionally, a PSI DRS4v4 evaluation board can be used to generate precise digital pulse processed triggers. The DRS4 is run by a PC which calibrates the board and sets the trigger threshold on up to 4 channels, with AND/OR logic. The DRS4 board can achieve down to -1 mV threshold triggering, but realistically is limited to 2-3 mV due to small baseline fluctuations. The induced trigger delay is O(1 μs) which is not a concern with the long waveforms O(20 μs) taken during normal data taking.

4.1.5.4 Digitizer

A CAEN V1724 FADC 6U VME module is employed to digitize the PMT waveforms with nearly zero deadtime. The PMT signals are transported to the FADC module by LEMO to MCX cables and the trigger uses a standard LEMO connection. The FADC samples at 100 MHz with a dynamic range of 2.25 V and multiple circular buffers. The buffers are filled in real-time when trigger pulses are encountered and read out via a CONET2 optical link regularly. The optical link connects via a dual optical fiber to the CAEN A3818A CONET2 PCIe card installed in a CENTOS 6 based linux machine.

4.1.5.5 Data Storage and Processing

The data sent from the FADC to the linux machine is written to binary on an internal standard four terabyte hard disk using modified CAEN software. The data is then synced to a Synology NAS in RAID5 for long term storage. Data files are transferred to a number of multicore analysis servers for offline analysis when necessary.

The servers employ custom ROOT-based software to perform the full analysis. The analysis chain converts the binary files to a ROOT format, reduces the data into pulse objects, identifies the physical nature of the pulse objects and combines them into corrected detector quantities, then finally reconstructs the event for final analysis.

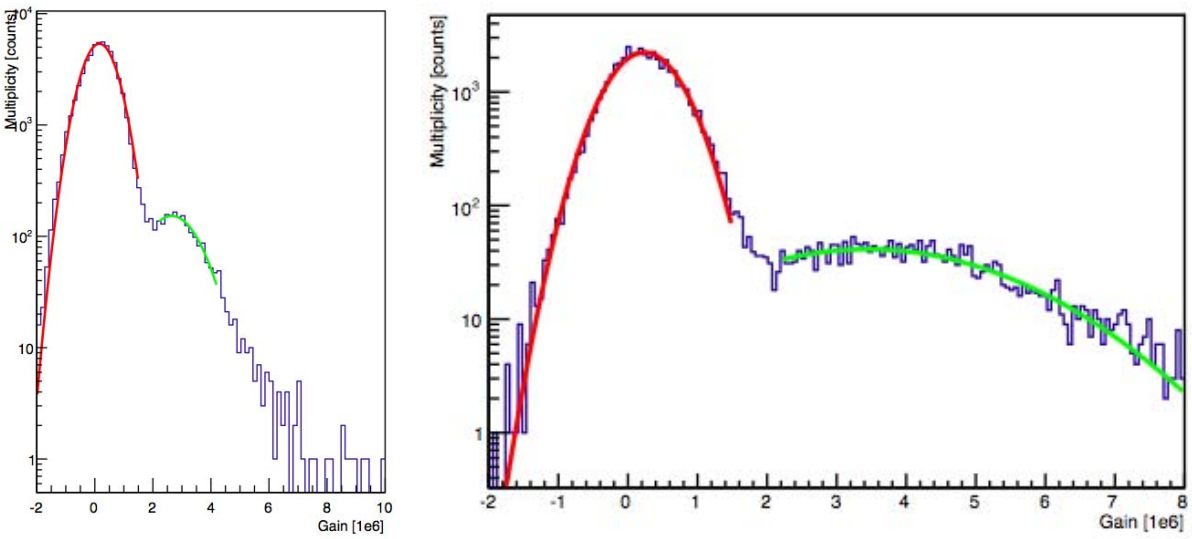

Figure 4.2.1: Left: A typical top PMT SPE spectrum near maximum gain. Right: The bottom PMT SPE spectrum near maximum gain. The noise peak and SPE peak are fit with gaussians to determine their mean and width. The gains can be computed by taking the difference of the SPE and noise means while the SPE resolution is the width of the fit SPE gaussian.

4.2 Analysis

Data captured must be analyzed offline using event reconstruction and selection techniques. The detector must first be calibrated by determining the gains of the PMTs and energy and position reconstruction abilities. The calibration and analysis is outlined in the following.

4.2.1 Single Photoelectron Calibration

The PMT gains can be calibrated with the pulsed LED coupled to the fiber optic feedthrough. The pulser signal is reduced to cause pulses only a few percent of the time with the rest of the events having no signal. This ensures that the vast majority of pulses induced are due to single photoelectrons that are liberated from the photocathode (not multiple photoelectrons). A gaussian peak can be fit to the noise peak and single photoelectron (SPE) peak, with the difference between the two gaussian means being the average SPE signal area (see Fig. 4.2.1).

The SPE gain calibration can then be bootstrapped to find the gain of each PMT across

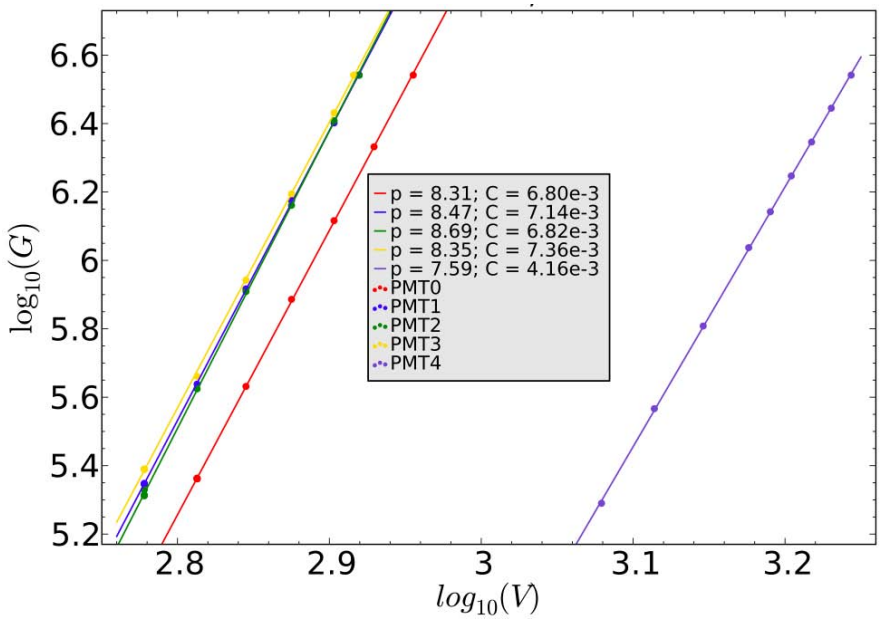

Figure 4.2.2: The gain fit for all PMTs used in the MiX detector. The gain of the PMTs are expected to have the form $G(V) \propto V^p$. The voltage of the TPMTs (PMT 0-3) were varied from around 600-850 V and the BPMT (PMT 4) was scanned from 1100-1750 V while a constant LED pulse sent photons toward the PMTs. A linear behavior is expected on a log-log plot and is indeed the case for all PMTs. The gain curves can be used to predict PMT gain at lower PMT voltages.

a wide range of voltages. First, the PMT voltages are set at the known gain found from the SPE calibration, then a large LED pulse is injected into the optical fiber O(1 kPE) and a large-pulse measurement baseline is taken for that gain. The injected pulse is held constant while the PMT voltages are then incrementally reduced. The pulse area in ADC units decreases with the voltage and can be compared to the original pulse area at known gain to find the reduction of gain at that PMT voltage. The results of the voltage scan calibration are plotted in Fig. 4.2.2.

4.2.2 Signal Analysis

Custom ROOT [83] software is used to store raw waveforms, reduce the waveforms to pulse quantities, then reconstruct the quantities into an event for final analysis. A ^{137}Cs calibration

dataset is used to define the pulse selection and event reconstruction parameters. Selection quantities are determined as follows.

For each event, all five PMT waveforms are summed and passed through a pulse finding filter. The waveform is smoothed with a window of 30 ns and samples which surpass the threshold for more than twenty nanoseconds are considered as signal. If the pulse is less than 350 ns in width, then it is classified as an S1 and if the pulse is greater than 350 ns but less than 6 μs it is labeled as an S2. All other pulses are labeled as noise.

Event reconstruction and selection is then accomplished. Drift times range from 1-15 μs but a fiducial volume cut is placed at drift times between 5-12 μs to remove events which happen above the gate and near the cathode grids. Additionally, the event x-y position is determined using a weighted average of S2 signal in the top PMTs. A radial position cut of about 17 mm is made which produces a fiducial LXe mass of around 25 grams.

Events in the fiducial volume are generally well-formed with regular signal generation qualities but the analysis still benefits from a final data quality selection process. An S2-width to S1-width ratio allowed region is enforced between 8.5 and 15 which removes both merged double scatter S2 signals on the high-side and misidentified S2s on the low-side. Events with a top S2-area to bottom-S1 area ratio below 30 are removed since they prove to be the result of bottom PMT ringing being identified as an S2 pulse.

4.2.3 ER Calibration

An electron recoil calibration of the MiX detector was accomplished with data captured from a ^{137}Cs source. The source was placed in close proximity to the side of detector (12 cm) and several million events were allowed to accumulate using a low threshold trigger. A clear photoabsorption peak can be seen in the ^{137}Cs S1 spectrum (see Fig. 4.2.5). The detector light yield and energy resolution is discussed in Sec. 4.2.5.

4.2.4 NR Calibration

The nuclear recoil response of the MiX detector was probed with a ^{252}Cf radioactive source. The source produces both high energy gamma rays and neutrons which produce recoils in

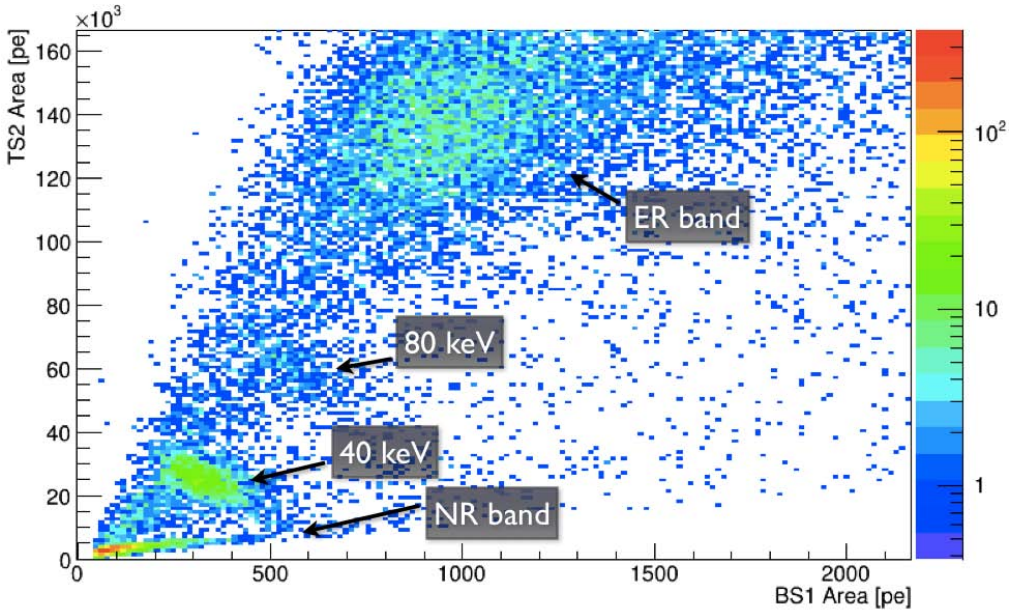

Figure 4.2.3: A top S2 versus bottom S1 spectrum for the MiX detector with ^{252}Cf neutron source. The NR band and ER band are labeled along with the two peaks associated with inelastic nuclear interactions with a^{129}Xe and ^{131}Xe. The inelastic events generate gamma rays of energies 40 keV$_{ee}$ and 80 keV$_{ee}$, respectively, and are displaced from the ER band due to an NR signal component from the recoiling xenon nucleus.

the detector. The source is placed behind 10 cm of lead to effectively shield the gamma contribution from overwhelming the dataset. Events are allowed to accumulate with the same low energy trigger as used with the ^{137}Cs source.

The topology of events due to the ^{252}Cf source are varied with standard elastic recoils and two additional contributions due to inelastic scattering on xenon isotopes. The ^{129}Xe and ^{131}Xe isotopes undergo inelastic scattering with resulting gamma ray energies of 40 keV$_{ee}$ and 80 keV$_{ee}$, respectively. The recoil produces both the ER from a gamma ray and an NR from the recoiling xenon nucleus. The resulting spectrum can be seen in Figs. 4.2.3 and 4.2.4.

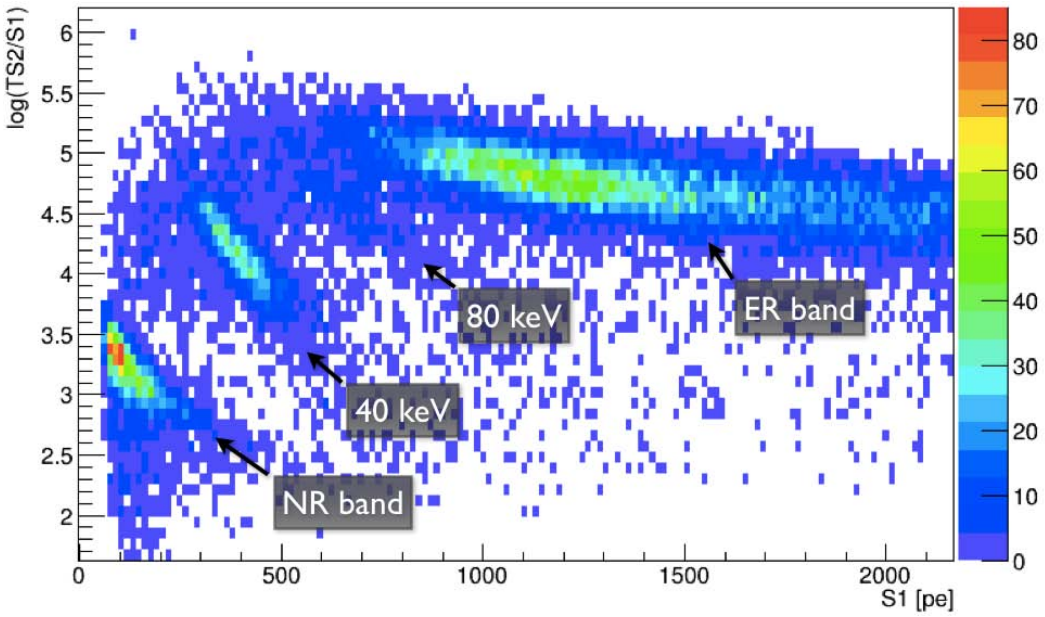

Figure 4.2.4: A $\log_{10}$(top S2/S1) plot of ^{252}Cf events in the MiX detector. The NR and ER bands are labeled along with the 40 keV$_{ee}$ and 80 keV$_{ee}$ energy depositions from inelastic neutron interactions with ^{129}Xe and ^{131}Xe, respectively. A clear identification of the depositions and separation of the NR and ER bands is shown at these energies.

4.2.5 Light Yield and Energy Resolution

The spectra from the ^{137}Cs and ^{252}Cf sources contains features which can be used to determine the detector performance. In the ^{137}Cs datasets, the total photoabsorption peak can be fit to determine the detector light yield and energy resolution at 662 keV$_{ee}$. Likewise, with the ^{252}Cf datasets the 40 keV$_{ee}$ peak can be fit (and have the NR contribution subtracted) to give the resolution and light yield at 40 keV$_{ee}$. Where S1 quenching must be accounted for the NEST [68, 69] model is used.

Figure 4.2.5 shows the energy spectrum and fit used for both energies with the fit parameters and subsequent light yield (at 1 kV/cm drift field) in Table 4.3. The S1 resolution is calculated from the fit for 662 keV$_{ee}$ and 40 keV$_{ee}$ to yield $(8.7 \pm 0.6)\%$ and $(22 \pm 4)\%$, respectively. The good resolution of S1 is complementary to the high light yield obtained.

The apparent discrepancy in the light yield is a result of the energy dependence of photon production in liquid xenon. The NEST [68, 69] model can be used to convert the observed

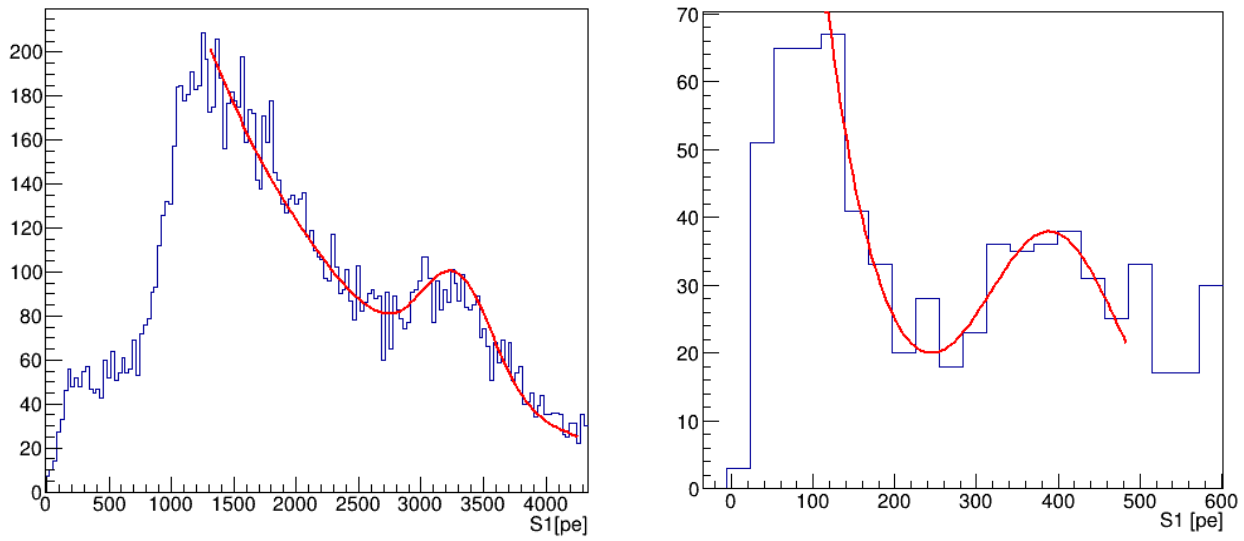

Figure 4.2.5: Left: The S1 spectrum from a ^{137}Cs source is fit with decaying exponential and gaussian to determine the light yield 662 keV$_{ee}$. Right: The S1 spectrum from a ^{252}Cf source fit with a decaying exponential and gaussian determines the light yield at 40 keV$_{ee}$. The fit quantities are noted in Table 4.3.

light yield into the commonly cited zero field light yield at 122 keV$_{ee}$, L_y^{122}. First, a conversion from the 1 kV/cm light yield at 662 keV$_{ee}$ (40 keV$_{ee}$) to light yield at 122 keV$_{ee}$ is done using the parameters in Table 4.4, obtaining 5.46 ± 0.15 PE/keV$_{ee}$ (5.30 ± 0.29 PE/keV$_{ee}$). The two light yields are averaged to produce the estimate at 1 kV/cm for 122 keV$_{ee}$, $\mathrm{L}_y^{122}(1\frac{\mathrm{kV}}{\mathrm{cm}})$. Then, the light yields at all three energies are estimated at zero field using the NEST photon yields in the table.

The above calculations were carried out using the following relations. To convert a light yield between energies with the same field use

$$\mathrm{L}_y^b = \frac{\mathrm{Y}_y^b(f_1)}{\mathrm{Y}_y^a(f_1)}\mathrm{L}_y^a(f_1),$$

where f_1 is the electric field and both a and b are energies in keV$_{ee}$. To convert a light yield with the same energy to a different field use

$$\mathrm{L}_y^a(f_2) = \frac{\mathrm{Y}_y^a(f_2)}{\mathrm{Y}_y^a(f_1)}\mathrm{L}_y^a(f_1),$$

Source	Energy[keV$_{ee}$]	Mean[PE]	Width[PE]	Est. NR[PE]	L$_y$(1$\frac{\text{kV}}{\text{cm}}$)[PE/keV$_{ee}$]
^{252}Cf	40	392.9 ± 11.2	86.3 ± 16.6	90 ± 10	7.57 ± 0.38
^{137}Cs	662	3291 ± 20	286.9 ± 31.4	0	4.97 ± 0.03

Table 4.3: The quantities derived from fitting the S1 spectrum of the 40 keV$_{ee}$ and 662 keV$_{ee}$ peaks from ^{252}Cf and ^{137}Cs sources, respectively. The drift field was identical for both datasets which allows for calculation of the light yield L$_y$ at 1 kV/cm for both energies. The NR signal component of the 40 keV$_{ee}$ line was estimated in order to remove the contribution from the light yield calculation.

where a is the energy in keV$_{ee}$ and both f_1 and f_2 are drift fields. Errors are propagated in the standard way.

Energy[keV$_{ee}$]	Y$_y$(1$\frac{\text{kV}}{\text{cm}}$)[$\gamma$/keV$_{ee}$]	L$_y$(1$\frac{\text{kV}}{\text{cm}}$)[PE/keV$_{ee}$]	Y$_y$[γ/keV$_{ee}$]	L$_y$[PE/keV$_{ee}$]
40	40.0 ± 0.5	7.57 ± 0.38	65.0 ± 0.5	12.3 ± 0.64
122	28.0 ± 0.5	5.38 ± 0.33	61.0 ± 0.5	11.7 ± 0.75
662	25.5 ± 0.5	4.97 ± 0.03	60.0 ± 0.5	11.7 ± 0.26

Table 4.4: The scaling parameters (photon yield Y$_y$) used to derive light yield quantities (L$_y$) by the NEST [68] model for MiX light yields at a drift field of 1 kV/cm and zero field (see Fig. 3.5.1). The center line contains estimated light yields for ^{122}Co in the MiX detector. The scaling of light yield (found in Table 4.3) from both ^{252}Cf and ^{137}Cs peak energies to 122 keV$_{ee}$ is completed then averaged to estimate the quenched L$_y^{122}$(1$\frac{\text{kV}}{\text{cm}}$). The drift field dependence is then removed to estimate the zero field light yield at all three energies L$_y^{40}$, L$_y^{662}$, and L$_y^{122}$.

4.2.6 Position Reconstruction

Positions are reconstructed using the weighted average of the S2 signal in the top PMTs. Due to mathematical degeneracy (of using a normalized S2 signal for reconstruction), the only region which can be reconstructed well is that in the center of the x-y plane. In practice, this behavior defines an r fiducial volume cut near 17 mm in the MiX detector. In the fiducial volume, the position reconstruction for x-y-z is better than 2 mm as seen in Fig. 4.2.6 from resolving the grid nodes (2 mm spacing) and a S2 peak time uncertainty of less than a microsecond (about 2 mm).

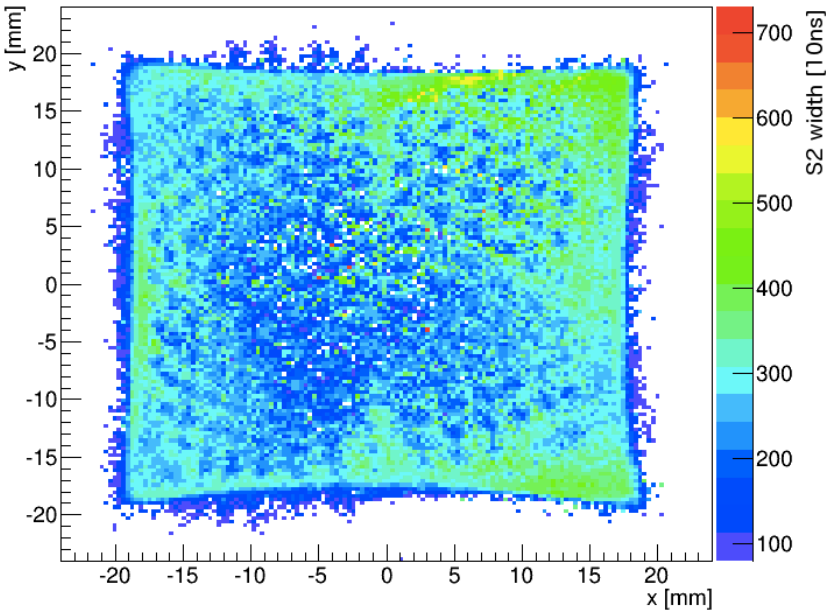

Figure 4.2.6: The profile of S2 widths from a ^{137}Cs source. The structure is caused by the hexagonal 2 mm grid pattern, which is resolved across the x-y plane.

CHAPTER V

PANDAX I: A 125/37 kg (sensitive/fiducial) Dual Phase LXe TPC

The PandaX dark matter search program operates a dual phased liquid xenon time projection chamber in western China. The institutions of Shanghai Jiao Tong University, Shandong University, Shanghai Institute of Applied Physics, University of Michigan, Peking University, University of Maryland, and Yalong Hydroelectric Company form the PandaX international collaboration effort. A three staged approach is taken in the PandaX experimental program. The large infrastructure like the outer vacuum vessel, many-ton radiation shield, cryogenics system, and gas handling have been designed to accommodate all three stages. The inner vessel will be upgraded between each stage, switching to a low radioactivity stainless steel version between stages I and II, then to a larger low background version between stages II and III. The TPC will be upgraded at each stage as well to accommodate the ever increasing sensitive mass - 125kg, 500kg, 1700kg for stages I, II, and III respectively. The data acquisition system will be upgraded between stages II and III to accommodate the greater number of digitized PMT channels.

The China JinPing Laboratory houses the PandaX experiment, located northwest of Xichang, Sichuan, China. The laboratory is housed in a hydroelectric service tunnel beneath $2,400$ m of radioactively quiet marble rock ($6,800$ m.w.e.) in JinPing Mountain (see Figs. 5.0.7 and 5.0.8). CJPL is the deepest scientific lab in the world and contains laboratory space housing both the PandaX and CDEX [12] dark matter search experiments with plans to expand in the near future.

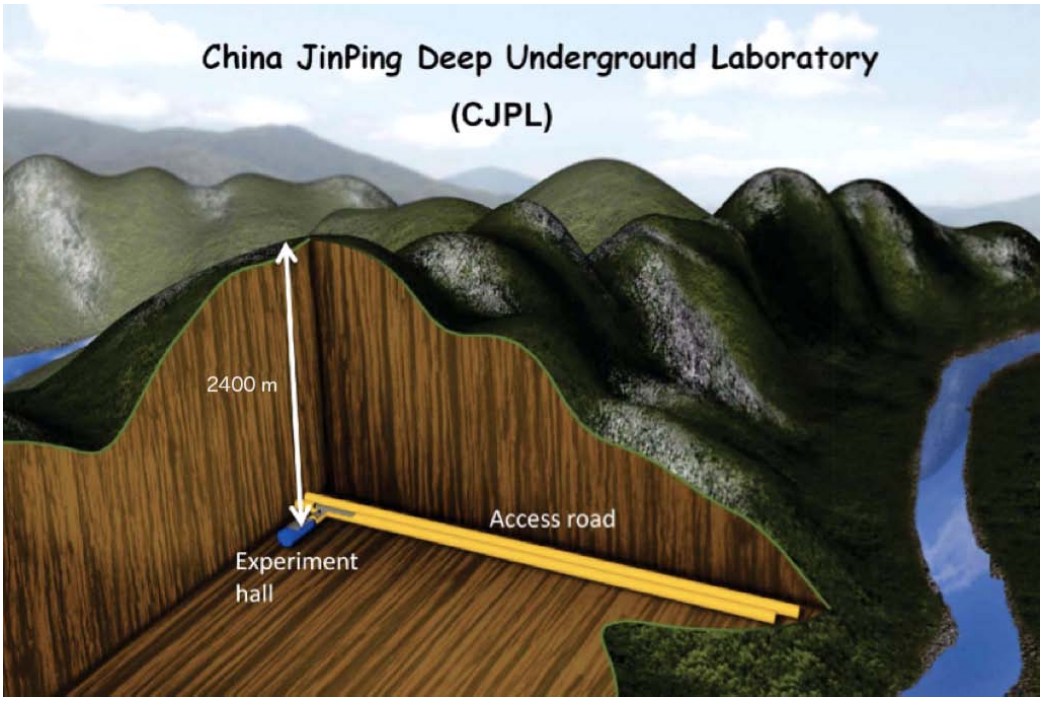

Figure 5.0.7: China JinPing Laboratory is located 2,400 meters underground (6,800 m.w.e.) in JinPing mountain, located in Sichuan, China. The lab is accessible through a 17 km hydroelectric service tunnel (midway). An office utilized by the collaboration is located at the east entrance to the tunnel.

5.1 PandaX-I

During the years of 2010-2012 the PandaX and PandaX-I specific systems were designed, constructed, and tested at SJTU. In Spring 2012, the supporting PandaX systems were moved to CJPL while the PandaX-I detector underwent final testing. In Fall 2012, the PandaX-I TPC and final components were shipped to CJPL and commissioning started. In early 2013, the first commissioning LXe run, Run3, took place with only bottom PMT sensors activated. Run3 was conducted to test system stability and functioning of all major components. A further commissioning run, Run4, started August 2013 to test the system with all PMTs in place and activated with intended full dual phase operation. The success of Run4 was softened by a broken high voltage connection to the cathode, however most goals of the run were met. In January 2014 the final Run5 for PandaX-I was started with the goal of conducting a long dark matter search until Fall 2014. The first segment of Run5

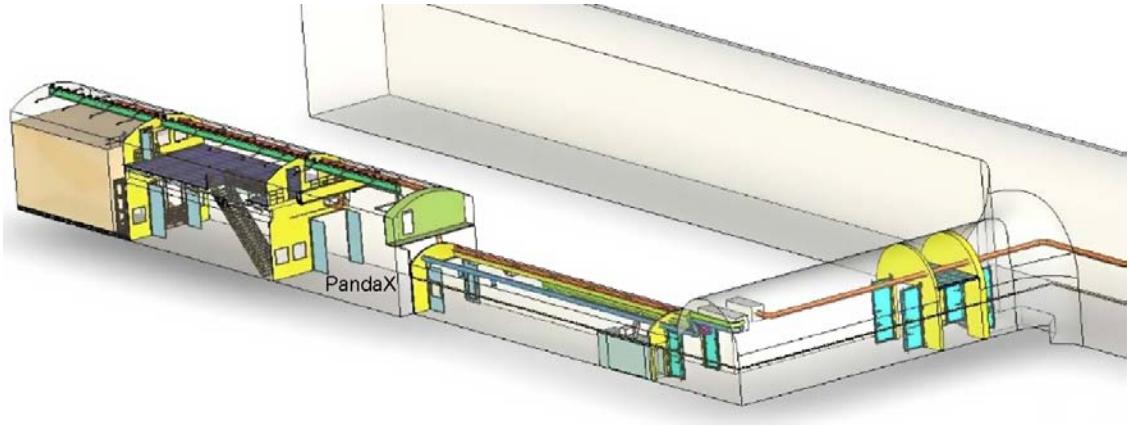

Figure 5.0.8: A schematic view of CJPL as viewed from the southeast. The experiment is accessed from the tunnel via a staging area and connecting hallway. PandaX is situated in the front volume of the large experimental hall while CDEX [12] occupies the back portion. Figure from [84].

was a final commissioning and detector characterization effort. After May 2014 the detector was fully characterized and the dark matter search started. The characterization of the PandaX-I detector will be discussed in this chapter, followed by a discussion of the expected and observed PandaX-I background in Ch. 6, and finally a discussion of the analysis leading to the spin-independent WIMP-nucleon dark matter search results for Run5 takes place in Ch. 7.

5.2 Design

PandaX-I was designed as a high light collection efficiency (low threshold), high drift field, low background detector which takes advantage of the deep CJPL location to reduce the complexity of the shielding structure. A cooling system which can handle target masses much greater than the 450 kg utilized in PandaX-I was designed using a bus system, as described in Ref. [80]. A multi-ton shield was designed to block electromagnetic and neutron backgrounds originating in the surrounding laboratory environment. A pancake TPC utilizing 180 PMT channels and a virgin PTFE reflector was designed to allow the detector to achieve a low energy threshold. The liquid xenon sensitive mass is 125 kg with a fiducial volume selection of 37 kg. The PandaX-I detector is planned to operate for a total of 100 live-days with a

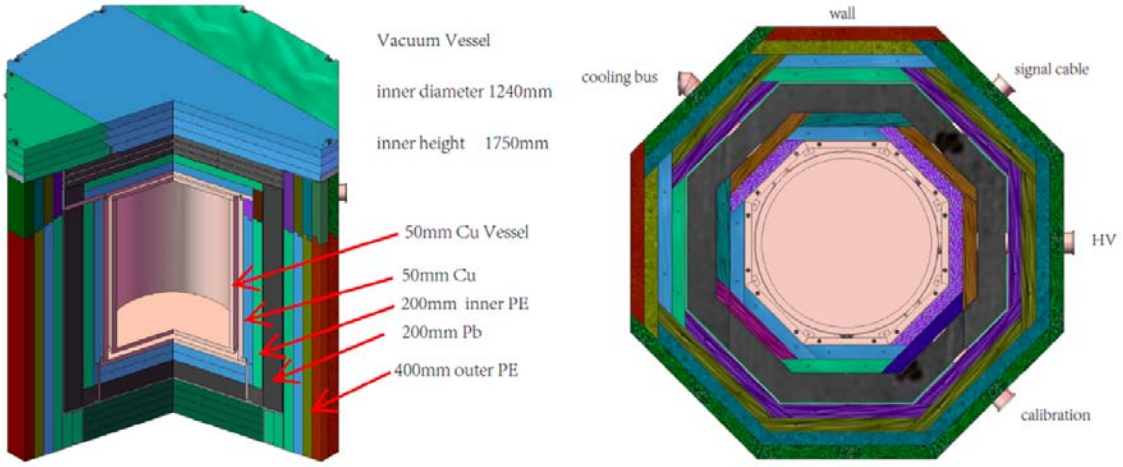

Figure 5.2.1: A schematic of the PandaX shield which will be employed for all PandaX stages. Layers of polyethylene, OFHC copper, and lead protect the inner volume from impinging neutron and electromagnetic radiation. Dry nitrogen is continuously flushed through the shield to limit radon radioactivity near the detector. Figure from [84].

low threshold that targets the tenuous low WIMP mass region.

5.2.1 Shield

The detector shield protects against radiation originating in the surrounding lab materials like rock, concrete, support infrastructure for the experiment, and other material. The design must consider two types of radiation which could cause significant background within the detector: that of a penetrating electromagnetic origin and from fast neutrons. The penetrating electromagnetic radiation is solely due to gamma rays which nominally originate from radioactive decays outside the detector and is stopped with a layered lead and copper configuration. The high Z properties of copper and lead provide ample electrons upon which the penetrating gamma rays to scatter and lose energy. Additionally, the materials are particularly dense which provides even greater stopping power. Single scatter fast neutrons are the most problematic type of background since they mimic WIMP interactions identically. The neutrons must be carefully shielded against with layers of polyethylene. The polyethylene has many hydrogen nuclei upon which the impinging neutrons can scatter and lose energy.

The neutron and electromagnetic shielding scheme must be carefully determined so that each

layer does not hinder more than it guards. The octagonal layers are chosen in a way that maximizes stopping power on the external layers, then has progressively more radioactively clean layers internally. A 40 cm polyethylene layer makes up the outermost neutron shielding layer, then a 20 cm thick lead layer constitutes the first electromagnetic shield. Inside the lead is another 20 cm polyethylene layer which is designed primarily to moderate neutrons originating from the lead layer due to ^{210}Pb decays. Inside the second polyethylene layer is the final octagonal shielding layer of 5 cm thick OFHC copper, which, along with the 5 cm OFHC copper outer vessel, serves as the secondary electromagnetic shield. See Fig. 5.2.1 for a representation of the shield deployed for PandaX-I.

Finally, there is shielding that ultimately comes from the liquefied xenon itself, termed self-shielding. This EM shielding is provided by O(10 cm) of LXe which surrounds the detector's fiducial volume (both active and nonactive shielding) and guards against further stray radioactivity originating from the shield and detector components.

5.2.2 Detector

The PandaX-I overall design was completed with several goals in mind. These goals were chosen to be in line with the characteristics of a development detector in the PandaX program. The first goal was to design a low energy threshold detector that can help probe the light mass WIMP region of parameter space. The detector was also designed with scalability in mind so that major system components can be utilized at a later date with minimal modification. Additionally, the detector should be able to be constructed rapidly.

With these goals in mind, the following criteria were chosen. Phase I will have a pancake detector design with high light collection efficiency to allow for deep probing of the light WIMP region. The considerable sensitivity to low mass WIMPs is derived from the additional reach gained when lowering the detector energy threshold coupled with the sharply falling exponential recoil spectrum associated light dark matter (see Fig. 1.3.2). The ratio of radius to drift length is four-to-one which places the PMT arrays in relatively close vicinity to the sensitive volume. The reverse field region was minimized to reduce nongaussian leakage into the nuclear recoil band from neutron-X events. The materials were carefully screened and selected, largely employing low radioactivity virgin PTFE, OFHC copper, and

stainless steel. Nonessential items are held outside the shield to further reduce the chance of background contamination due to their presence. The detector can easily be scaled to the next stage, using the same cryogenics and inner vessel design, but employing a taller, upgraded TPC for PandaX-II.

5.2.3 Cryogenics

The cryogenic demands of the PandaX-I detector require liquefaction of nearly half a ton of xenon, stable operation of the target mass and detector at liquid xenon temperature over long time scales, emergency provisions in the event of normal operation interruption, and the ability to recover the xenon fully when the run is completed. This is achieved with the use of the multifaceted cooling bus design. The cooling bus liquefies the target mass in less than a week's time, holds the inner vessel temperature to within one tenth of a Kelvin for months, employs a LN_2 coil design to provide instant emergency cooling, houses the heat exchanger which increasing efficiency of the circulation system, and contains instrumentation to monitor the physical status of the system. The design has proved to be very successful over the series of PandaX-I runs.

5.3 Construction

The cooling bus, a stand-in stainless steel outer vessel, the inner vessel, TPC, and gas handling system were constructed at SJTU for thorough testing of the system [80]. The TPC was assembled at SJTU with 88 PMTs to test TPC performance in gas phase and operation of a reduced capacity DAQ. The radiation shield was constructed and copper cryostat fabricated and delivered to CJPL in the interim. A large, raised platform to hold personnel and equipment during detector operation provides access to the top of the shield (where all detector feedthroughs are present).

The systems were then moved to CJPL for assembly. The DAQ was upgraded and finalized to its current 196-channel form. The TPC was fully reassembled with 180 PMTs in two arrays. Electrical shielding problems with the PMT cabling were overcome with conductive

fabric shielding after on-site troubleshooting. TPC high voltage systems were assembled and tested in a Dry Run onsite at CJPL.

5.4 Cryogenic System

During the dark matter search (Run5) the operation of the detector was stable. Occasional power outages in the beginning of Run5 were the only nuisance during operation, but they did not present a major obstacle over the entire run. The stability of the detector and slow control quantities from June-July of 2014 is evident with temperature and pressure being held within 1% during the dark matter search period.

5.4.1 Equipment

The cryogenic system demands the use of several subsystems to achieve smooth reliable operation at low temperature. Much supporting machinery in the form of vacuum pumps, power distribution equipment, a leak checker, residual gas analyzers, storage, and gas handling equipment is necessary. A discussion of the major subsystems follows.

5.4.1.1 Xenon Storage

Gaseous xenon is stored in large custom stainless steel high pressure bottles hung from load cells to measure the mass contained in the each bottle (≈ 200 kg). The load cells are mounted to a frame structure which also houses a pulley system for raising and lowering of vacuum flasks large enough to envelope the high pressure bottles. The vacuum flasks are open air vessels which hold the bottles in a liquid nitrogen bath if cryopumping of the bottles is desired. An additional small network of steel bottles is accompanied by a small stainless steel high pressure bottle to recover a few kilograms of xenon that are not stored in the large bottles. The xenon recovery process is described in Sec. 5.4.2.2.

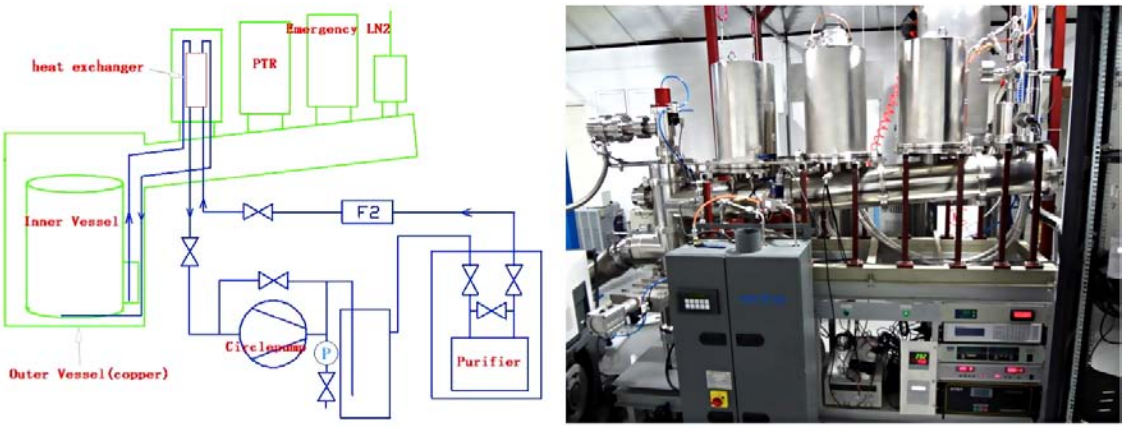

Figure 5.4.1: Left: A schematic of the cooling bus with circulation system. Right: A photograph of the cooling bus during the testing phase at SJTU. The PTR draws heat from the system while the circulation pump forces xenon through the purifying getter and heat exchanger [80]. An emergency LN_2 coil is the final module on the bus. Figure from [84].

5.4.1.2 Gas Handling

A gas panel with gas solenoid operated valves and a pressure regulator controls the flow of xenon out of the storage bottles. Additionally, manual valves control the circulation pathways that supply xenon to the cooling bus. The gas panel supplies both a controlled pathway for xenon filling and recovery along with manually operated emergency pathway for xenon recovery. Filling and recapture of the xenon is monitored by a gas panel mounted flow meter. The emergency gas conduit allows unobstructed xenon recovery via cryopumping in the event that all electrical power is lost.

5.4.1.3 Cooling Bus and Supporting equipment

The cooling bus consists of a pulse tube refrigerator (PTR), emergency LN_2 coil, heat exchanger, and supporting gas plumbing as outlined in Ref. [80]. A gas panel feeds the bus and provides the passage to the storage bottles. The cooling bus supporting equipment includes a continuous circulation pump and SAES PS15-MT50 noble gas hot getter (see Fig. 5.4.1). The circulation pump is a prototype Q-Drive model which reliably (and quietly) pumps clean GXe at 30 SLPM through the getter. The pump is a modified pulse tube designed to cleanly pump gas with high efficiency, low mechanical noise, and high reliability.

5.4.1.4 Cryostat

An o-ring sealed outer vessel constructed of 5 cm thick OFHC copper provides the vacuum jacket for the inner vessel (and serves as the innermost layer of the electromagnetic shield). A hermetically sealed stainless steel inner vessel was constructed to house the detector components and PandaX-I detector. A copper filler occupies the bottom of the inner vessel in order to displace xenon (to reduce cost but maintain radioactive shielding).

5.4.1.5 Instrumentation and Slow Control

Measurement of the state parameters of the system is achieved through the use of a custom Python-based Slow Control System coupled with temperature sensors, vacuum and atmospheric pressure gauges, feedback from controllers, and state notification from critical systems like the uninterrupted power supply (UPS). Platinum resistors transduce the temperature in various locations in the inner vessel and cryogenic system. The UPS and SCS server status are logged regularly. Pressure sensors monitor the outer vacuum pressure and the inner vessel GXe pressure. Readout from the Lakeshore 340 controller gives the state of the temperature feedback loop governing the heater regulated cryocooler head temperature.

All quantities are stored in a database for later assessment and realtime awareness of the system both remotely and in the lab. Selected quantities are automatically compared with acceptable limits and if out of range the SCS will send an alarm through text message and email to personnel. Additionally, an outside server monitors internet connectivity to the slow control computer and alerts personnel outside the lab in the event of a lost connection.

5.4.2 Liquefaction

The liquefaction process is accomplished with the equipment outlined in Sec. 5.4.1. Gaseous xenon is transformed in liquid after encountering the coldhead in the cooling bus, then flows down the bus into the inner vessel. A net gain of liquid xenon is achieved when the supply bottles are allowed to empty into the cooling bus and is stopped once the appropriate mass of xenon has been liquefied, putting the liquid height near the appropriate level.

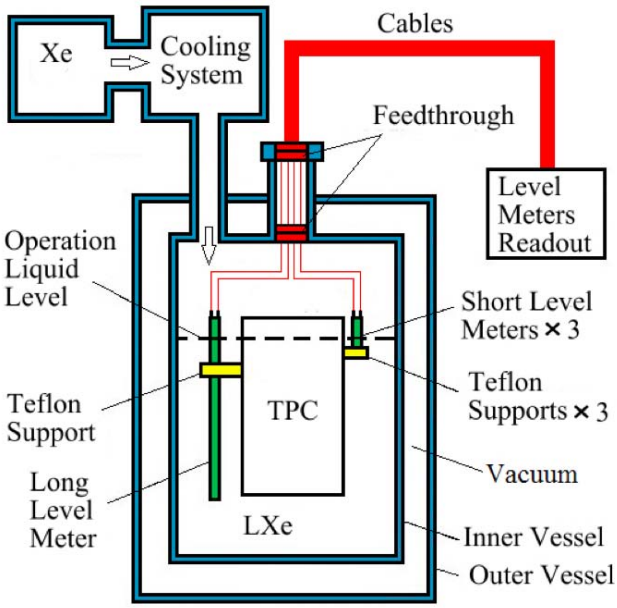

Figure 5.4.2: A schematic of the level meter system employed for the PandaX-I detector. PTFE supports hold three short level meters and one long. The short level meters monitor the fine LXe height and leveling of the surface. The long meter measures the height of the LXe over a large range. Figure from Ref. [85].

5.4.2.1 Liquid Height and Level

An overflow weir is used to control the overall LXe height in the detector. A linear motion feedthrough connects an actuating cable to the overflow point in the inner vessel, precisely adjusting the point up or down. The leveling of the detector is accomplished by adjusting three cone-shaped legs which support the entire outer vessel. Differentially adjusting the legs shifts the vessel to achieve a level LXe surface relative to the detector grids. The overall liquid xenon height is measured using a capacitive level meter coupled to a universal transducer interface (UTI) circuit (see Fig. 5.4.2). During filling, liquid xenon enters the inner vessel, submerging the detector, until the height nears the gate (see Fig. 5.4.3). At that point, three small capacitive level meters are partially submerged by LXe, allowing for fine adjustment of height and level. A UTI board tracks the capacitance of each level meter, as described in Ref. [80].

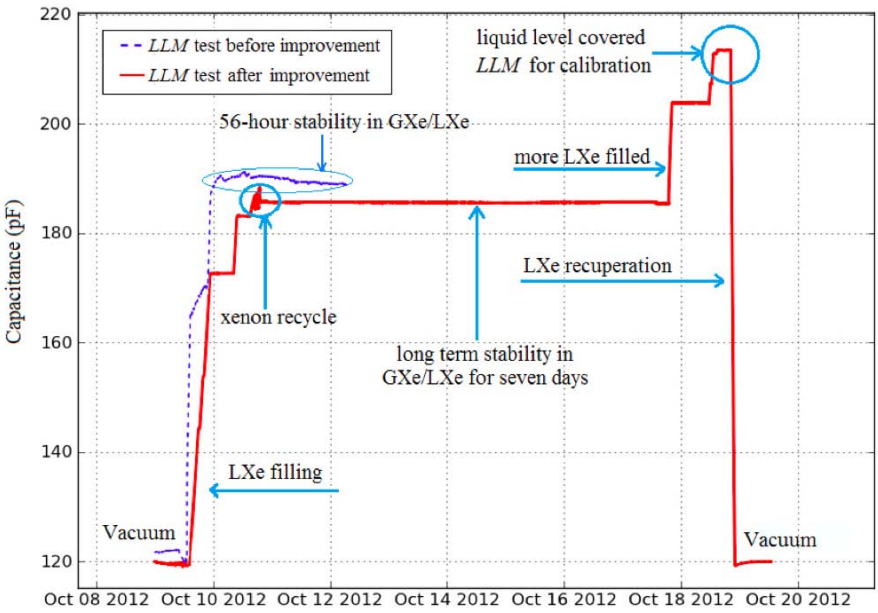

Figure 5.4.3: Plot of level meter testing before correction (blue) and after correction (red) [85]. The level meter with universal transducer interface system was improved to yield a highly stable measurement of the LXe height. Over the course of a ten days, the LXe was filled, level adjusted, and then recovered with precise meter behavior. Figure from Ref. [85].

5.4.2.2 Xenon Recovery

After a run is complete, xenon is recovered from the inner vessel with the cryopumping technique. To achieve this, stainless steel high pressure bottles are held in a vacuum jacket flask then cooled in a bath of liquid nitrogen to 77 K. GXe from the inner vessel is allowed to flow into the storage bottle, encountering the cooled bottle surface and freezing to the bottle wall. This controlled process cleanly pumps gaseous xenon from the inner vessel to the storage bottles with no moving parts. Once the bottle is filled the valve is closed and the bottle is allowed to slowly warm, moving the xenon from a frozen state with no pressure to a gaseous state of nearly 80 atm at room temperature. After both large high pressure bottles are filled, the remaining balance of 50 kg is recovered into a smaller stainless steel high pressure vessel then allowed to expand into standard steel gas cylinders.

5.4.2.3 Emergency Cooling

The PandaX-I detector utilizes emergency procedures and equipment which allow for control of the system during unexpected events such as power failures or equipment failure. If the inner vessel pressure rises too high, an emergency liquid nitrogen system is activated. An electric solenoid valve allows LN_2 from a high pressure LN_2 dewar to enter the emergency LN_2 coils inside the cooling bus. The flowing LN_2 will freeze GXe onto the emergency coils, relieving pressure in the inner vessel. The emergency LN_2 system is largely passive and can be operated for extended periods of time to keep the LXe cool in the event that the PTR fails to provide ample cooling power due to helium compressor failure, PTR head failure, or extended power failure. To provide passive outer vacuum pumping, Zeolite is kept in a LN_2 bath with a pneumatic valve ready to open if the emergency sequence is activated. In the event of a long outage of PTR cooling power the xenon can be recovered through the normal process safely into the high pressure bottle storage.

5.5 Purification Systems

The target material must be free of radioactive isotopes that could contaminate the energy region of interest to a dark matter search. In particular, the beta background from ^{85}Kr is problematic since the isotope is commonly found in atmospherically extracted xenon. The overall krypton level must be reduced to the parts per trillion level (mol/mol) to achieve a ^{85}Kr background rate less than O(1/year) in a ton-scale detector. Additionally, the xenon must be cleaned of electro-negative impurities to allow the unimpeded transmission of scintillation photons and efficient transportation of drifting electrons. To combat both of these problems a krypton removal system and continuous purification are employed.

5.5.1 Krypton Removal

A low energy background from the beta decay of ^{85}Kr is present in large xenon experiments. To combat this background, a krypton distillation tower was developed at SJTU to reduce the krypton contamination level of commercially available research grade xenon gas (see Fig.

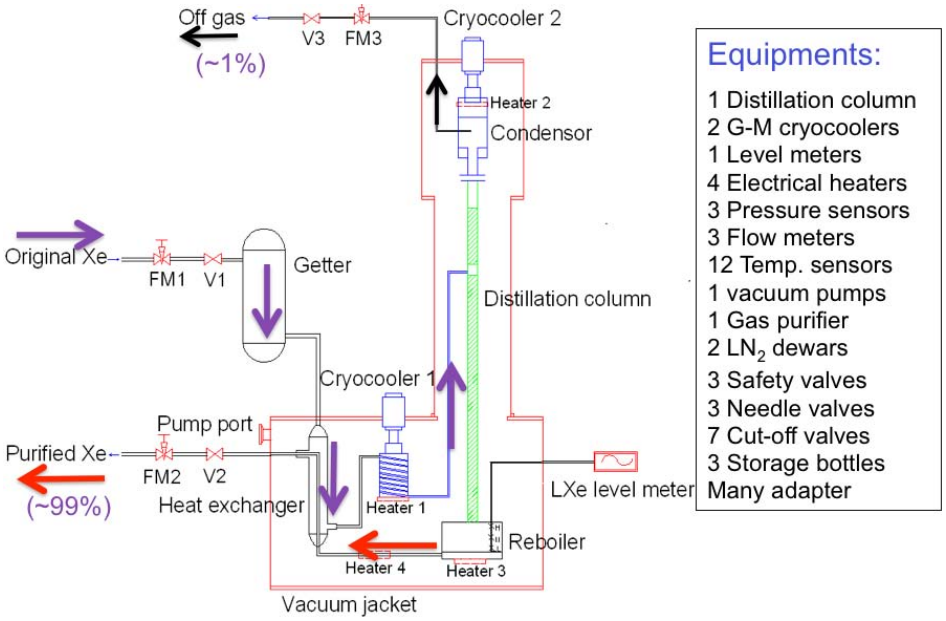

Figure 5.5.1: Schematic of the krypton distillation tower. Liquid xenon is held at its boiling point with a temperature gradient up to the second cooling head. Xenon flows into the apparatus where 1% of the mass is concentrated with krypton (the off-gas) while the remaining 99% flows out with reduced krypton content. Figure courtesy of Zhou Wang.

5.5.1). The design was pioneered by the XMASS collaboration to achieve ppt (mol/mol) level contamination of krypton [86]. The tower utilizes the different boiling points of krypton and xenon to vertically separate krypton from xenon across a thermal gradient. The xenon enters the column with a krypton impurity level of ppb mol/mol. The column is three meters in height with 6 theoretical McCabe-Thiele (MT) plates and is designed to reach the ppt (mol/mol) level. The offgas is concentrated in krypton while the remaining xenon stock has correspondingly diminished krypton content. In this process there is 99% efficiency of xenon recovery for the cleaned gas. The final krypton contamination level in the xenon target material used for PandaX-I was measured to be below 70 ppt by both probing with data analysis techniques and a gas composition assay using a sensitive in-house gas composition measurement system.

5.5.2 Continuous Purification

Purification of the LXe is necessary in order to achieve high light and charge yield in a dual-phase LXe detector. The pump creates a pressure differential which extracts LXe from the inner vessel, pushing it through the heat exchanger and causing the xenon to undergo a phase change from liquid to gas. The gas passes through the Q-Drive then enters the SAES hot getter where reactive impurities are absorbed into the getter material. A stable circulation rate of 30 SLPM was maintained over the course of many months which allowed the experiment to achieve the desirable outcome of a long drift electron lifetime (see Section 7.3.1). This positive effect of circulation is also evident in the very high light and charge yield seen in the PandaX-I detector, as discussed in Secs. 7.3.2 and 7.3.3.

5.6 Time Projection Chamber

The detector employed by the PandaX-I experiment is a pancake-shaped time projection chamber which utilizes dual phase xenon to observe both a light and charge signal via photomultiplier tubes. The PMTs transduce photons to electrical signals which are read by the data acquisition system, as described in Sec. 5.8. The TPC design allows for the reconstruction of the event energy and position, giving calorimetry and event imaging. Details of the operating principle of a dual phase LXe TPC are outlined in Ch. 3. The cylindrical TPC volume is formed by a 36-side regular polygon with a radius of 30 cm and height of 15 cm. The cylindrical volume is then capped with two plates to complete a 4π envelope of the sensitive volume. All internal non-instrumented surfaces are made of virgin PTFE, a highly reflective (>95% for LXe) material in the VUV range. The remaining instrumented internal surfaces are the photocathodes from the PMT arrays lining the top and bottom reflective plates, as shown in Fig. 5.6.1.

5.6.1 Electrodes

There are three electric fields of interest generated in the TPC volume. The fields are generated between the cathode grid, gate grid, liquid/gas interface, and anode grid (see Fig.

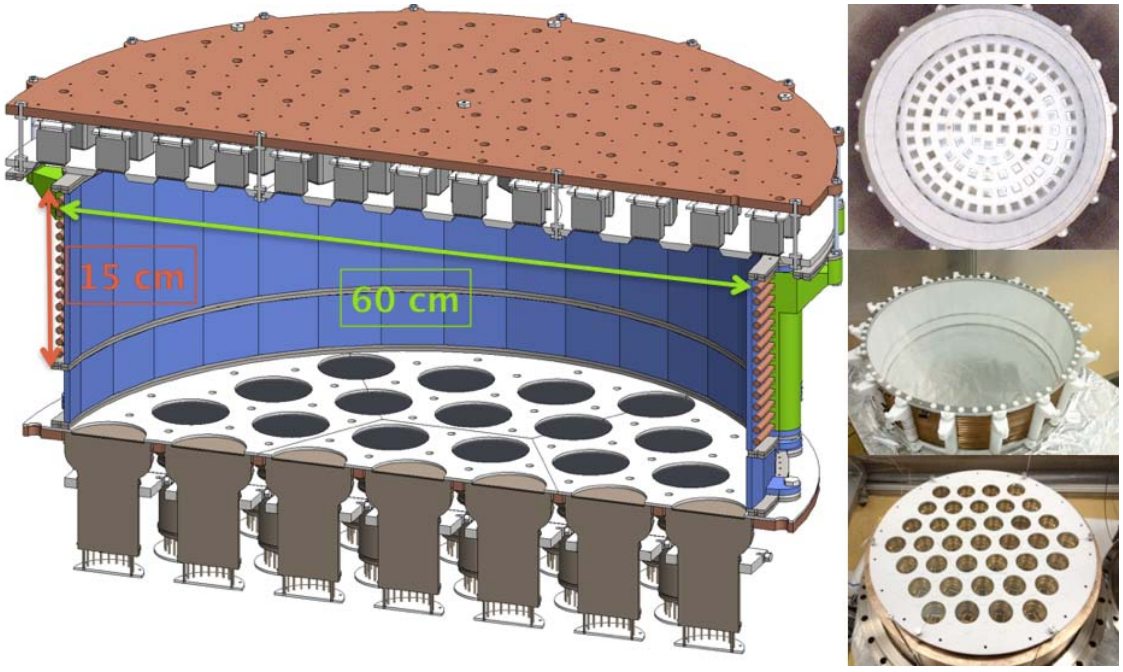

Figure 5.6.1: Left: Schematic cutaway of the PandaX-I time projection chamber. The cylindrical volume is surrounded by PTFE reflector and top/bottom PMT arrays. Right: Photograph of the assembled top PMT array(top), the field cage and cylindrical reflector(middle), and the bottom PMT array mounted in the copper filler(bottom).

5.6.2). A drift field is drawn between a horizontal cathode grid and a matching gate grid elevated 15 cm above the cathode. The gate grid is held at a negative high voltage O(-5 kV) and a greater negative voltage O(-15 kV) is placed on the cathode. This scheme generates a downward electric field which forces the negatively charged ionization electrons to drift upward. Between the gate and liquid gas interface exists the extraction field and above the liquid gas interface is the gas gap field. These fields are caused by the voltage difference between the grounded anode and negatively charged gate grid (and z-dependent dielectric constant between). The extraction field drifts the electrons to the surface and provides the impetus for them to escape the potential well of the liquid, releasing into the gas. The electric field in the gas gap provides the field necessary to accelerate the extracted electrons enough to generate the proportional secondary scintillation S2 signal. In the PandaX-I TPC a total gate to anode gap of 8 mm is set and the liquid level is kept at a nominal 4 mm.

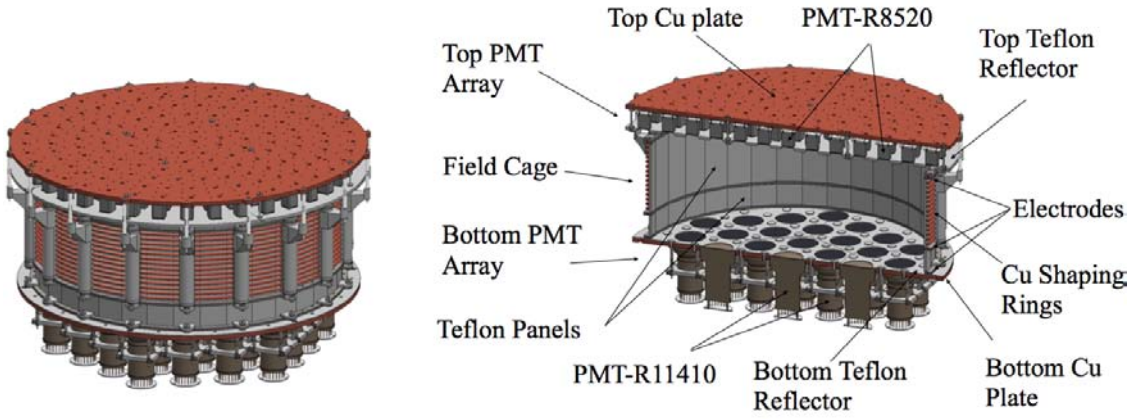

Figure 5.6.2: Schematic of the PandaX-I TPC with major components detailed. OFHC copper plates provide support for the PMT arrays while a PTFE reflector encloses the volume. A field cage and TPC electrodes (anode, gate, cathode) provide the electrostatic environment necessary to drift and extract ionization electrons. Figure from [84].

5.6.1.1 Anode

Extracted ionization electrons are carried through the gas gap to meet the anode surface, continuously liberating scintillation photons along the way. The anode is formed from a thin stainless steel sheet that is chemically etched to reveal a grid pattern with square unit cells. The grid has a pitch of 5 mm with 100 μm thickness wires, and has been shown to enhance the uniformity of the S2 signal generation in small scale tests (compared to parallel wires).

5.6.1.2 Gate and Cathode

The gate and cathode are constructed using a parallel wire method. Stainless steel 200 μm diameter wires are strung across a circular stainless steel ring with a pitch of 5 mm. The wires are tensioned with 228 gram weights to 41% of their yield strength to avoid sagging. A second stainless steel ring is screwed on top to secure the wires between the rings and complete the unit. Both rings are mounted in their respective locations in the TPC with the cathode at the bottom and the gate 8 mm below the anode grid.

Figure 5.6.3: Left: Schematic of field shaping cage and electrodes. A grounded anode caps the top of the high electric field region, the gate voltage sets the extraction field, and the cathode voltage sets the drift field. A set of 14 field shaping rings sets the voltage boundary conditions to maintain a uniform field in the TPC. Center: Photograph of a gate, cathode, and screening electrode unit formed of parallel 200 μm wires at 5 mm pitch. Right: Photograph of assembled electrodes and field cage with cylindrical reflector. Figure from [84].

5.6.1.3 Field Shaping Rings

The final electrodes contained in the TPC are those of the field shaping rings (see Fig. 5.6.3). The parallel plate capacitor design of the TPC grids produces a near uniform field at low r, but has ever increasing divergence at higher r if there is no effort to correct this undesirable behavior with field shaping. The electrodes are rings of hollow OFHC copper tubes of 6 mm OD and 5 mm ID that are wrapped outside the TPC cylindrical reflector. The 14 rings are set at a pitch of 1 cm in the vertical direction and connected in series with 500 MΩ resistors (SM20D from Japan FineChem Company, Inc.), and connected at each end through 500 MΩ resistors to the cathode and grid. These shaping rings provide cylindrical equipotential boundary conditions near the perimeter that correct the inner electric field to near uniformity.

5.6.2 Photomultiplier Tubes

The only physics sensors in the PandaX-I experiment are the photomultipliers which line the top and bottom surfaces of the TPC (see Fig. 5.6.4). All relevant physics signals are sensed by these ultrasensitive light transducers. Photomultiplier tubes employ a photocathode to release photons via the photoelectric effect when struck by a photon, a set of signal amplifying dynodes to multiply the single photoelectron to a measurable signal, then an anode which

Figure 5.6.4: Left: Photograph of a top PMT is shown after assembly and testing with attached voltage dividing base circuit and cable assembly. Right: Photograph of a collection of bottom PMTs during characterization. The external teflon wrap is for protection during handling and is removed before insertion in the TPC.

gathers the electron avalanche. The electrodes in the photomultiplier are held in a vacuum, with no direct conductive path to the other elements. Currents are briefly formed when electrons are liberated from the electrode surfaces and transported through the tube by the applied electric fields.

When an impinging photon strikes the photocathode, it ejects an electron into the tube vacuum with a probability, or quantum efficiency (QE), near 30%. The ejected electron is termed a photoelectron due to its history as an ejected electron from the photoelectric effect. The photoelectron finds itself in the tube vacuum but that vacuum is permeated by an electric field which pulls the photoelectron toward the first dynode. The electron is accelerated and strikes the first dynode, being absorbed during a violent process which averages around four electrons ejected back out of surface. These secondary electrons find themselves in a lensed electric field which accelerates them to the second dynode where they are amplified yet again. For a typical photomultiplier the number of dynodes, or stages, ranges from 8-14 with 10-12 being typical. After the amplification stages the newly formed electron cloud is absorbed by the anode to give the final electric signal pulse which is digitized by the data acquisition system.

The circuit which holds the cathode, dynodes, and anode at their respective voltages for

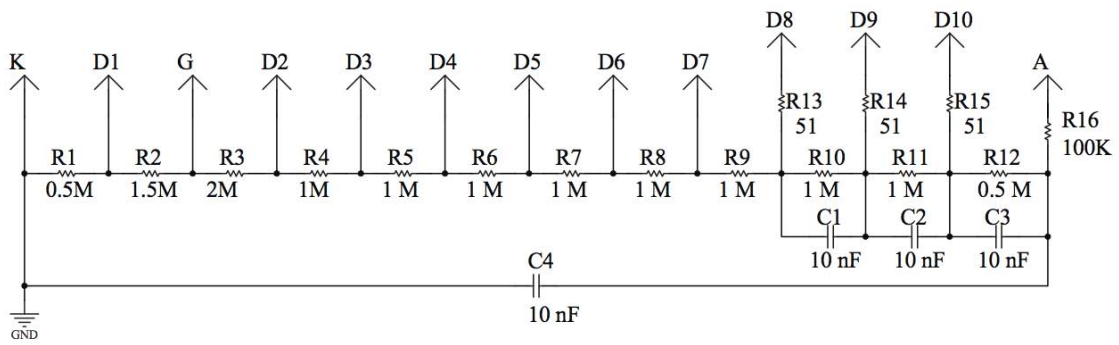

Figure 5.6.5: Schematic of the top PMT voltage divider circuit (base). The base utilizes charge reservoirs (capacitors) and resistors to maintain a static electric field inside the PMT and provide the charge seen as a signal pulse. The base is terminated at 100 kΩ to allow for both a reliable S1 and S2 signal. Capacitors C1 and C2 were removed to reduce the background rate emitted from the bases. Figure from [84].

proper operation is the PMT base. The base is a voltage divider which takes a large voltage difference O(1 kV) and divides it between the cathode and first dynode, first dynode and second dynode, etc., and finally between the last dynode and anode. The current which flows through the internal vacuum is supplied by the PMT base circuit. The base requires capacitors as a reservoir of charge because the pulse generation process would deplete charge very quickly in a capacitor-less system of the charge, making the voltages sag and inducing nonlinearity in the PMT response. This presents a tension between PMT performance and low background performance since the PMT capacitors are necessary to maintain a steady voltage supply in large signals but they also contribute a non-negligible rate to the background neutron budget. A compromise was met where one capacitor buffers the voltage held across the cathode and anode, and the last stage amplification stage also has a reservoir capacitor.

5.6.2.1 Top PMTs

The top PMT array is a collection of 143 Hamamatsu R8520-406 PMTs with custom Cirlex bases organized in an array with seven rings of increasing radius and mounted to an OFHC copper plate. The first ring is only a single central PMT, but then rings of 8, 14, 20, 28, 36, and finally another 36 PMTs fill out the array at ever increasing r. The rings are populated

in this way to provide accurate x-y reconstruction of S2 signals across the (r,θ) range while minimizing the background caused by the array (see Sec. 6.3.1 for a discussion on the EM background in PandaX-I). The PMT placement was optimized through Monte Carlo simulation.

An individual top PMT coupled to its base is referred to as a TPMT. The R8520-406 consists of an extended square 30×30 mm^2 metal package body with quartz window. The PMT is designed to be low in radioactivity and operate down to 173 K. Ten stages of metal channel (venetian blind type) dynodes are accompanied by a bialkali photocathode (20.5×20.5 mm^2 active area) and anode to form the internal PMT electrodes. The maximum recommended voltage difference is 900 V between cathode and anode, with a nominal operation voltage around 800 V. The spectral response is extended into the VUV region by the quartz window, reaching a sharp cut-off at 160 nm. The window has 90% transmission efficiency of the 178 nm scintillation light of Xe which contributes to the typical quantum efficiency value of 25% for the R8520-406.

The TPMT Cirlex bases (see Figs. 5.6.5 and 5.6.6) were custom designed to house the voltage divider circuit and provide physical connection to the PMT pins. The Cirlex substrate was chosen for its low outgassing properties to help reduce the offgas load which must be removed from the system by the getter. This reduced outgas load helps contribute to an increased drifting electron lifetime. The base couples to a coaxial Kapton cable which supplies the ground and positive high voltage to the circuit.

5.6.2.2 Bottom PMTs

The bottom PMT array is a collection of 37 Hamamatsu R11410-MOD PMTs with custom Cirlex bases organized in seven staggered rows then mounted to an OFHC copper plate. The first row is 4 PMTs, then 5, 6, 7, 6, 5, with a final row of 4. The rows are hexagonally packed in order to maximize centralized photocathode coverage in the bottom array. This optimization is crucial for obtaining a low energy threshold since the BPMTs gather the overwhelming majority of the S1 signal. The BPMT array can also provide an accurate, more smoothed, x-y reconstruction of S2 signals across the (r,θ). The R11410-MOD PMT is a very low background unit with ≈3x better EM background to photocathode area ratio (compared with the R8520-406). The optimization of the bottom array configuration was

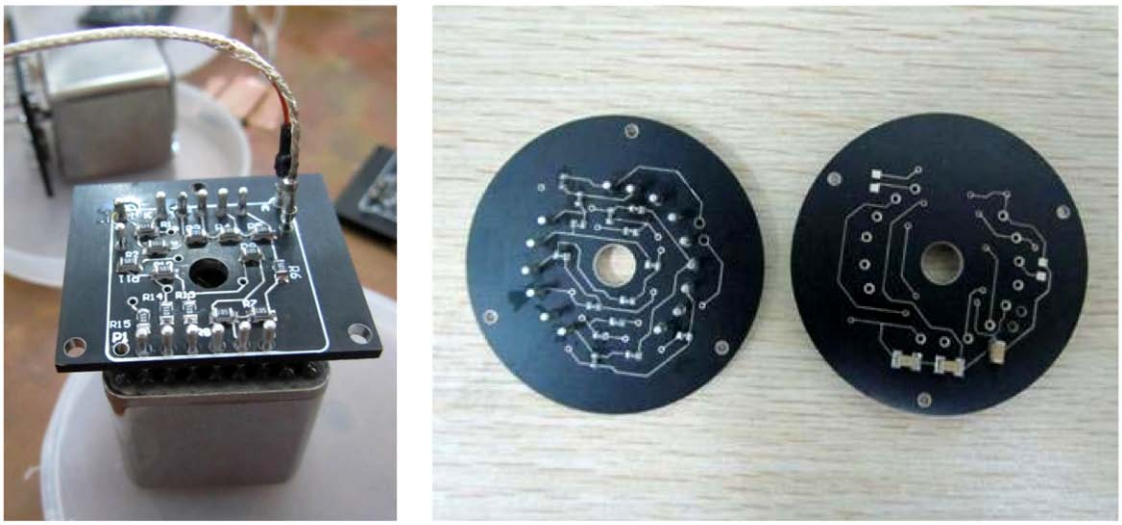

Figure 5.6.6: Left: Photograph of the Cirlex base for the top PMT attached to a Hamamatsu R8520-406. Right: Photograph of both sides of the Cirlex bottom PMT base. In both top and bottom cases, the Cirlex with deposited silver traces provides a very low outgassing substrate, reducing the offgas load in the inner vessel. Figure from [84].

done using Monte Carlo simulations. The large photocathode area of the bottom array contributes greatly to the S1 and S2 light collection efficiencies (LCE).

An individual bottom PMT R11410-MOD consists of a formed Kovar metal package body with synthetic silica window and is mounted to a custom Cirlex base. The PMT body is 76 mm in diameter with an active photocathode of 64 mm (71% active coverage area), and the metal body is formed to a smaller radius to house the dynodes. The total body length is 123 mm. The R11410-MOD is very low in radioactivity, has a SPE resolution of around 30%, and operates down to 173 K. An anode and twelve stages of dynodes accompany the low temperature bialkali photocathode. The maximum recommended voltage difference is 1,750 V between cathode and anode, with a nominal operation voltage near 1,500 V. As with the R8520-406 PMTs, the R11410-MOD has its spectral response extended into the VUV region by the quartz window with a sharp cut-off at 160 nm and about 90% transmission efficiency for 178 nm light. Typical quantum efficiencies for the R11410-MOD are around 30%.

The BPMT Cirlex bases were designed to contain the voltage divider circuit and provide physical connection between the PMT pins and cable (see Fig. 5.6.7). The BPMT attaches

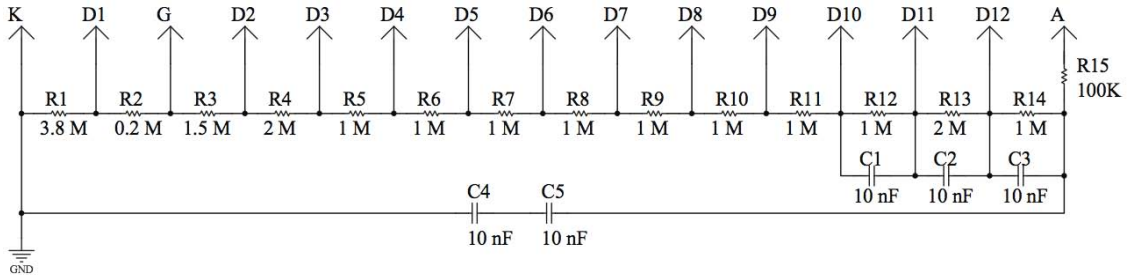

Figure 5.6.7: Schematic of the bottom PMT voltage divider circuit (base). The base utilizes capacitors and resistors to maintain a static electric field inside the PMT and provide the charge seen as a signal pulse. The base is terminated at 100 kΩ to allow for reliable S1 and S2 signals. Capacitors C1 and C2 were removed to reduce the background rate of the bases. Figure from [84].

to the Cirlex base via pin receptacles from Mil-Max Inc. The base couples to a coaxial Kapton cable which carries the ground and positive high voltage to the circuit. The circuit board tracks are deposited pure silver with no surface binder. Ceramic Kyocera capacitors and lead-free soldering tin (Sil-Fos) from Lucas-Milhaupt/Handy & Harman were used due to their minimal radioactivity. Finally, the PMT HV and signal are transported by a coaxial UHV KAP3 cable from MDC Inc.

5.6.3 PTFE Reflector

The target volume is surrounded by the 36-sided cylindrical TPC wall at the perimeter and by circular reflectors on top and bottom. The top and bottom reflector plates have clearance holes for the respective PMT type which is to be mounted; square for the top, round for the bottom. The reflector material is virgin PTFE, with the circumferential surface having 5 mm thickness, the top reflector 7 mm, and the bottom reflector 2.4 mm. The pieces were machined to interlock or be fastened with custom virgin PTFE bolts. Reflector supports are spaced along the perimeter of the TPC wall to provide mechanical support to the reflector as well as the TPC grids and field shaping rings. The PTFE is measured to be above 95% reflective based on Monte Carlo comparison of simulated detector response with acquired data. The purpose of the reflector is to provide a surface for the VUV photons upon which to diffusely reflect. The PTFE increases the probability of the originally 'missed' photon

eventually making its way to back a photon detector.

5.7 High Voltage Systems

High voltage must be supplied to the PMTs and TPC electrodes. The scheme for voltage delivery consists of fitting high voltage feedthroughs to both the outer and inner vessels and feeding high voltage via intermediary cables. There are a high number of PMTs which must have individual high voltage lines connected to them and only two for the HV TPC electrodes. Additionally, the high voltage level is different for the PMTs O(1 kV) when compared to the TPC electrodes O(10 kV). This means both systems must be considered separately in design and operation.

5.7.1 TPC High Voltage

The TPC high voltage has a small number of robust connections which must be made. There is a HV supply for both the gate and cathode grids while the Anode grid is grounded (see Sec. 5.6.1 for details). The negative HV for the gate is connected to a standard SHV feedthrough which transfers the voltage across the outer and inner vessel hermetic boundaries. The feedthrough into the inner vessel enters below the liquid surface then connects to a custom internal high voltage line which terminates on the gate grid. A maximum of -6 kV is supplied to the gate through this method. In practice, an operational voltage of -5 kV was maintained due to sporadic sparking encountered if operated at a more negative voltage. A 500 MΩ resistor of the type used between field shaping rings is placed between the anode and gate to reduce the current load on the gate power supply in steady state operation and also to allow controlled discharge of the anode-gate capacitor when the voltage level on the gate is changed (see Fig. 5.7.1).

The cathode is supplied with an even greater negative voltage. The custom feedthrough brings the cathode high voltage into the inner vessel through the liquid, and was designed to withstand -75kV. The feedthrough performs at the design level in air. During a LXe run in the PandaX-I vessel, the observed breakdown voltage was ≈-50 kV, while undesirable electroluminescence was encountered at voltages lower than -20 kV. It is believed that the

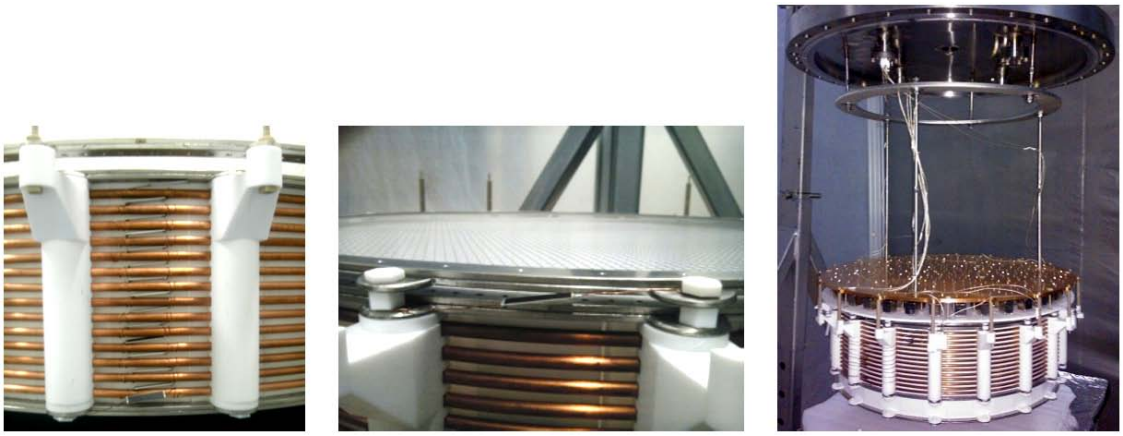

Figure 5.7.1: Left: Photograph of the resistor chain attached to the field shaping rings. The resistors linearly drop voltage vertically across the drift volume. Center: Photograph of the anode and gate electrodes. Right: Assembled TPC before the Run5. Figure from [84].

glow and breakdown occur at the sharp edges of the cathode, not at the feedthrough, since the induced liquid luminescence is fairly localized within the bottom PMT array. The practical action of raising the negative cathode voltage to -15kV was taken to suppress the chance of a cathode contribution to PMT dark current, however the lower drift field may actually be a boon for background rejection as noted in Ref. [87].

5.7.2 PMT High Voltage

Considerable care must be taken to ensure proper signal propagation and breakdown protection for the PMT high voltage system. Each PMT cable is coupled to an MPF feedthrough on the inner and outer vessel through its own ground pin and high voltage/signal pin. The positive high voltage nature of all PMTs in PandaX-I does not require the grounds to have individual pins but the coaxial signal protection offered from the individual ground and high voltage pins increases signal quality through reduction of induced noise and crosstalk. The safe passage of BPMT high voltages (max 1750 V) in the high density MPF feedthrough can be achieved because the feedthrough enters the inner vessel below the liquid level for the the BPMTs. For TPMTs, the lower maximum voltage (900 V) allows safe passage of high voltage even though the feedthrough enters the inner vessel in xenon gas.

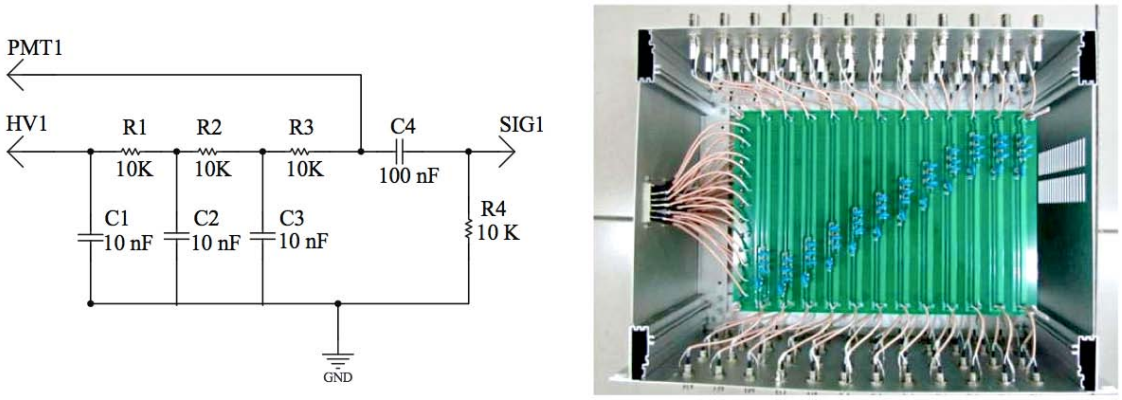

Figure 5.7.2: Left: Schematic of the decoupler circuit for a single PMT channel. The decoupler is a high pass filter which allows voltage changes due to PMT signals to pass through, eliminating the positive HV offset. Right: Photograph of the 12 channel decoupler circuit rackmount box. Figure from [84].

The high voltage for each of the 180 PMTs is generated by a CAEN A1517 power supply with four high density high voltage modules, each with 48 channels. The power supply has low ripple and allows each channels voltage level to be computer controlled. In the positive high voltage design both the signal and high voltage are carried on the same cable electrode and must be decoupled outside the detector (see Fig. 5.7.2). The PMT HV is supplied to the rackmount decoupler box and directed to the PMT cables. The decoupler taps the PMT high voltage with a capacitor that allows only the relevant sharp signals through, completely removing the O(1 kV) high voltage offset. In essence, the decoupler is a high pass filter which grabs the sharp signal wiggles and transports them to the data acquisition system.

5.8 Data Acquisition System

The signals from the PMTs are acquired with the fast hardware components and directed through software away from the data acquisition system (see Fig. 5.8.1). The hardware consists of a trigger system which instructs the DAQ to save digitized waveforms of all PMTs to a data file. The data file is then transported out of the experimental hall and further processed on a multicore server. The details of the data acquisition system are outlined in this section.

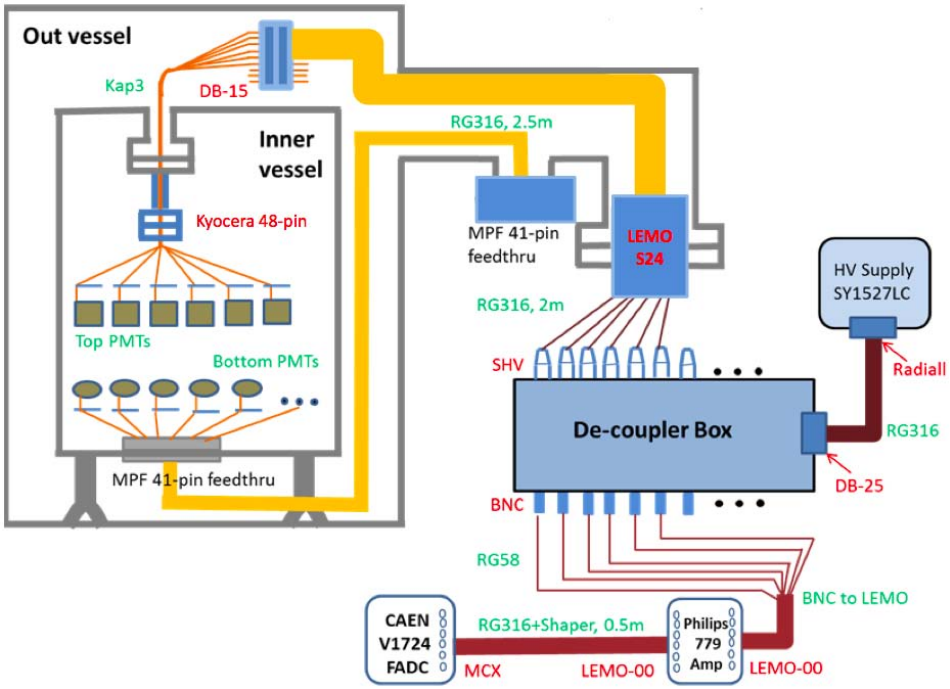

Figure 5.8.1: Schematic of the hardware components for PMT signal readout. The PMT cables emerge from the cryostat, the signals are decoupled from the positive HV offset, amplified, then digitized with CAEN V1724 modules in a VME64x crate. Figure from [84].

5.8.1 Hardware

The trigger can be generated using several schemes. For LED calibration, outlined in Sec. 7.1.1, a trigger is generated each time a voltage pulse is sent to the LED. During calibration and dark matter data taking the trigger is switched to a time-over-threshold (ToT) mode. The monitor signal from each set of eight PMTs is routed to a CAEN V814 field programmable gate array (FPGA) board which discriminates the input signal based on the width of a pulse while over voltage threshold. A spectroscopy amplifier based charge trigger was also used early in the data taking to trigger normal events. The ToT trigger was found to be more efficient for dark matter data taking due to its superior ability to trigger on low energy S2 pulses (<200 PE), allowing a reduced threshold compared to the charge trigger. Trigger efficiency is discussed in Sec. 7.3.8.

The high voltage PMT cables are routed to the data acquisition crates then decoupled. The

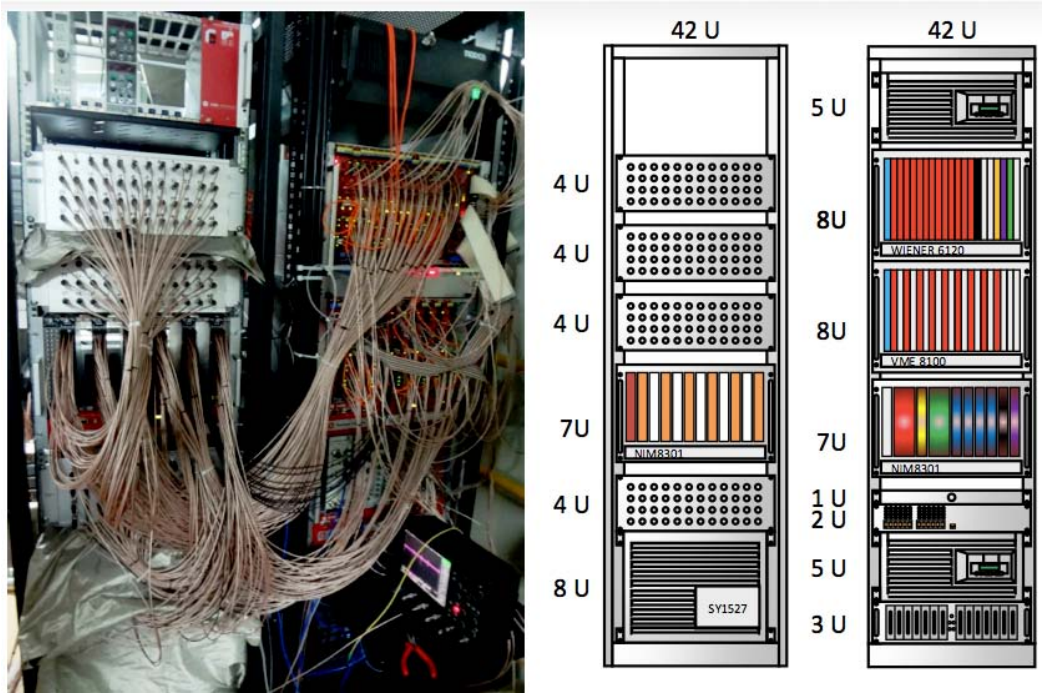

Figure 5.8.2: Left: Picture of the hardware crate. Right: A schematic of the layout for the crates and modules for the data acquisition system. Power supplies, decouplers, and linear amplifier populate the left crate. The right houses a DAQ server as well as crates for the FADCs and trigger logic. Figure from [84].

decoupler removes the DC offset O(1 kV) present in positive high voltage PMT systems. The decoupled signal is fed into a 10x Phillips linear amplifier, then directed to the CAEN V1724 fast analog to digital converter (FADC) boards. The FADC boards digitize the waveform of each of the 180 PMT channels in 10 ns sample time steps. The board continuously digitizes but allows data to fall off the pipeline unless there is a trigger condition sensed. If the FADC is triggered, then it locks the digitized waveform in the current buffer and switches to a new circular buffer for near deadtime-free operation. Once enough events are saved in the buffer, a transfer of the buffer contents on each FADC board is initiated to send the accumulated events to the DAQ server disk via optical fiber transfer. The DAQ server then writes the acquired data to hard disk in binary format. With this scheme, a maximum data taking rate of about 100 Hz is achieved which allows headroom for calibration runs which induce a nominal maximum event rate of 50 Hz (see Fig. 5.8.2 to view the DAQ hardware).

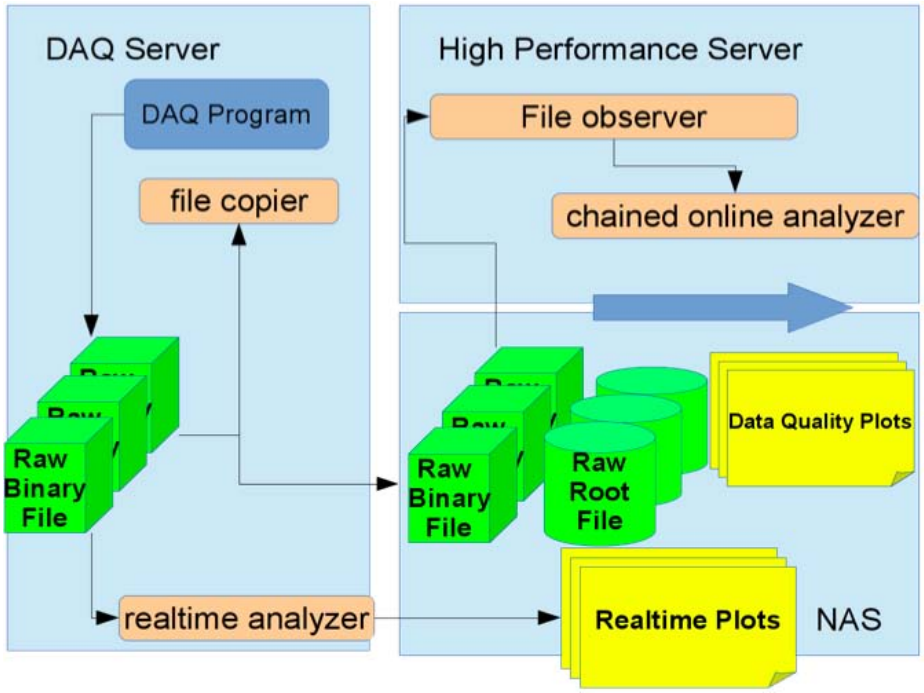

Figure 5.8.3: A schematic of the data handling used in the PandaX-I analysis. Binary files are written to disk by the DAQ server then transported out of the experimental hall to an external analysis server. The files are then converted to a ROOT [83] format and enter the data analysis pipeline (see Ch. 7 for analysis details). Figure from [84].

5.8.2 Software

Custom software handles the operation of the data acquisition system. The software communicates with the VME crates to initialize all FADC boards with parameters contained in a run XML file. Once events are triggered and written to the DAQ server hard disk, a PERL serving script transfers the file contents to an analysis server outside of the laboratory in real time (max 80 MB/s). The analysis server runs a PERL client script which awaits the incoming data and writes an exact copy of the binary file to a network attached storage (NAS) array in Raid 5 configuration. The checksum of the binary file is validated once the transfer is complete and the file is held for storage, awaiting offline analysis. For a visualization of the data flow, see Fig. 5.8.3.

5.9 PandaX-II

In Fall 2014, construction of the PandaX-II detector was started at SJTU with deployment scheduled for early 2015. The TPC houses 500 kg of sensitive LXe with a 300 kg fiducial volume. PandaX-II is planned to accumulate 300 live-days of exposure to target the high mass region of WIMP-nucleon parameter space starting in Spring 2015. The large exposure and high light yield allow aggressive probing of both the low and high mass WIMP region of parameter space. A novel nonlinear field shaping ring scheme will be employed to reduce the warping of drift electric field lines encountered with the standard linear spacing scheme. A low background inner vessel of similar dimensions will replace the standard stainless steel vessel deployed for PandaX-I to yield a lower background rate from inner vessel radioactive isotopes.

The TPC will use three inch Hamamatsu R11410 PMTs exclusively to transduce the S1 and S2 signals in the sensitive volume. A veto region will occupy the space between the TPC outer radius and the inner vessel wall which employs the one inch Hamamatsu R8520 PMTs. The PMTs will view the S1 signals induced in the veto region, allowing rejection of double scatters originating outside the TPC sensitive volume. With these modifications, the PandaX-II experiment expects to reach cross-section sensitivities near 10^{-46} cm^2 for a WIMP mass of 50 GeV/c^2.

CHAPTER VI

PANDAX I: Background

Reducing and characterizing background events in a dark matter search is key to achieving the sensitivity necessary to probe novel regions of parameter space. A direct detection experiment can expect the sensitivity to be proportional to MT (mass $\times$ time) as long as background is negligible. Once a background is encountered, it must be considered (either explicitly or implicitly) in the sensitivity calculation, which causes the sensitivity to rise as only $\sqrt{MT}$ [88]. Background sources which could cause events in a detector are numerous but most can be reduced to imperceptible levels during a detector operation time scale O(year) with proven techniques. The design of the detector must be simulated with realistic impinging backgrounds to determine the efficacy of the shield and detector design. In this chapter the PandaX-I background reduction and characterization effort is discussed.

6.1 Design Background Consideration

In rare event searches the ability to reduce encountered background events to a manageable level is key for achieving sensitivity goals. If the number of anticipated signal events is low, then the detector's background must be correspondingly low to ensure that the signal is not washed out. In practice, this means the total number of background events throughout the entire span of a run must be O(1). Only when this condition is met can an NR signal of only a few events be interpreted as a dark matter signal. The matter is complicated by the exponentially falling energy spectrum of WIMP-nucleus interactions which if present would

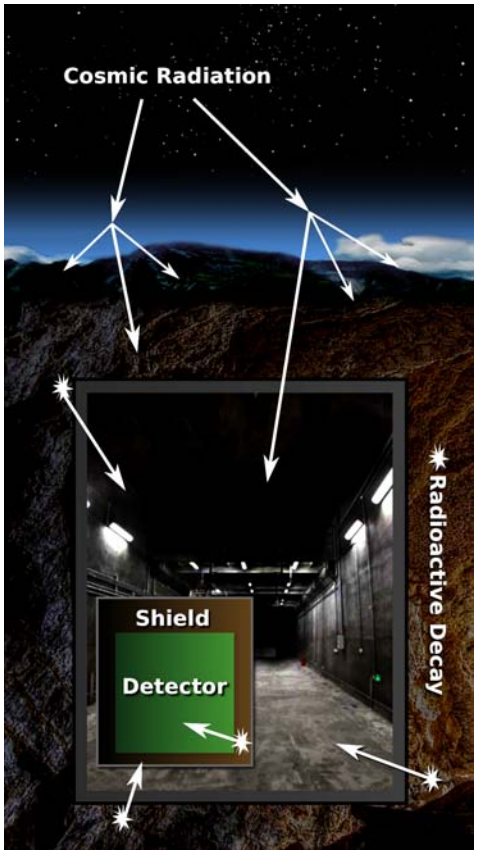

Figure 6.1.1: Visualization of background sources for an underground rare event search. Cosmogenic muons are moderated by rock and earth above the detector. Radioactive sources in the rock and laboratory structures are blocked by the detector shield. The rare background events which make it to the detector are cut with analysis techniques.

have very low energy events as the first detected events. This low energy preference makes experimentalists cautious when signal events are found in the lowest energy bins. It just so happens that low energy (near threshold) is where detectors start to have very pedestrian threshold effects (like baseline fluctuations, dark noise, or low signal identification efficiencies) creep into their workflow, tainting the analysis. More directly, experimenters are correct to be suspicious when interpreting signal events in the lowest energy bins.

The effort in this background section is focused on blocking physical events which may contaminate the data via calculated shielding and construction efforts. On the other hand, Chapter 6.4.2 focuses on using event analysis to efficiently remove irreducible background

events after they have happened in the PandaX-I detector.

6.1.1 ER Background

Radiation of electromagnetic nature is the most common form of background event in a LXe particle detector. Most forms of contaminating EM radiation can be minimized by surrounding the detector with shielding and selecting radioactively quiet detector construction materials. Additionally, electromagnetic radiation has a distinguishably different detector response when compared to that of a WIMP-nucleus scatter event. This characteristic allows active rejection of captured ER events during the offline analysis stage. The rejection is not perfect, with O(0.1%) of EM recoils fluctuating enough to look like an NR event, but is the final crucial step in reducing background in the WIMP search window. The imperfect nature of the ER/NR discrimination drives the need for anticipating the EM background in the detector, then comparing the leakage estimate with the measured spectrum of the dark matter run.

To reduce the electromagnetic background, thick high Z material was added to the multi-ton shield as layers of OFHC copper and lead. The high Z material has many valence electrons upon which impinging radiation will scatter, moderating the EM background. The shield's design is discussed in Sec. 5.2.1.

6.1.2 NR Background

Sources of nuclear recoils originating from Standard Model sources are a background which cannot be discriminated against. For practical reasons (there are not many nuclear recoil inducing background types), the only source of nuclear recoil background in detectors are those caused by stray fast neutrons. A neutron can scatter from a xenon nucleus, forcing it to recoil in the same manner as a WIMP-nucleus interaction would (see Sec. 3.4.3). The only pragmatic solution to reduce the rate of all possible sources of background NR is to reduce the neutrons in the lab environment to a very minute level.

Reduction of neutron background is achieved by placing the detector deep underground to avoid cosmogenic neutrons, wrapping the detector with a multi-ton hydrogen-rich shield to

moderate neutrons which originate in the rock and lab environment, and finally selecting low radioactivity detector construction materials to minimize near-target spontaneous radiation. Hiding from cosmogenic neutrons is achieved through the selection of CJPL, the world's deepest underground lab, as the site for PandaX. The multi-ton detector shield contains two layers for moderating neutrons. An outside first layer of polyethylene (PE) is used to stop impinging neutrons that originate outside the shield, then another layer of PE is just inside the outermost layer of lead shielding (to moderate neutrons emitted from the lead). The second layer of electromagnetic shielding does not require an inner PE layer since the construction material chosen, OFHC copper, has no perceivable neutron production. Nuclear recoil concerns due to (α, n) reactions in the shield are mitigated by a meticulous cleaning of shield surfaces before construction and a constant flow of dry nitrogen offgas to reduce radon levels in the shield from ambient levels of 400 Bq/m^3 to less than 10 Bq/m^3.

6.2 Counting Station

A high purity germanium crystal (HPGe) based counting station is employed in the PandaX experimental hall at CJPL to assay the radioactivity content of key detector components. The depth of the lab allows for a simple counting scheme, with no cosmic ray veto necessary. The HPGe detector is an Ortec GEMXX low background model (94100-HJ-LB-C-108) with a relative efficiency of 175% and resolution of 2.3 keV (FWHM) at 1.33 MeV. Events in the HPGe crystal are digitized by an Ortec DSEPC502 data acquisition system which acquires events with a shaping time of 12 μs. A shielding castle is built around the detector at a thickness of 10 cm for OFHC copper used in the inner layer and 20 cm of lead for outer layer in order to shield the HPGe detector from electromagnetic background (see Fig. 6.2.1).

The background spectrum for the counting station is shown in Fig. 6.2.2. Radioactive isotopes of ^{226}Ra, ^{228}Th, ^{137}Cs, and ^{60}Co in the shielding copper are all well below 1 mBq/kg, but the ^{40}K is relatively high, at 4 ± 1 mBq/kg. The moderate ^{40}K background is believed to originate from surface contamination. The ^{210}Pb activity in the shielding lead varies from 110 to 290 Bq/kg in several samples. The counting chamber has a cross-section of 20×20 cm^2 with a height of 34 cm which allows ample room for sample pieces of the detector (see Fig. 6.2.1). The HPGe detector sits in the volume with samples placed just above the crystal.

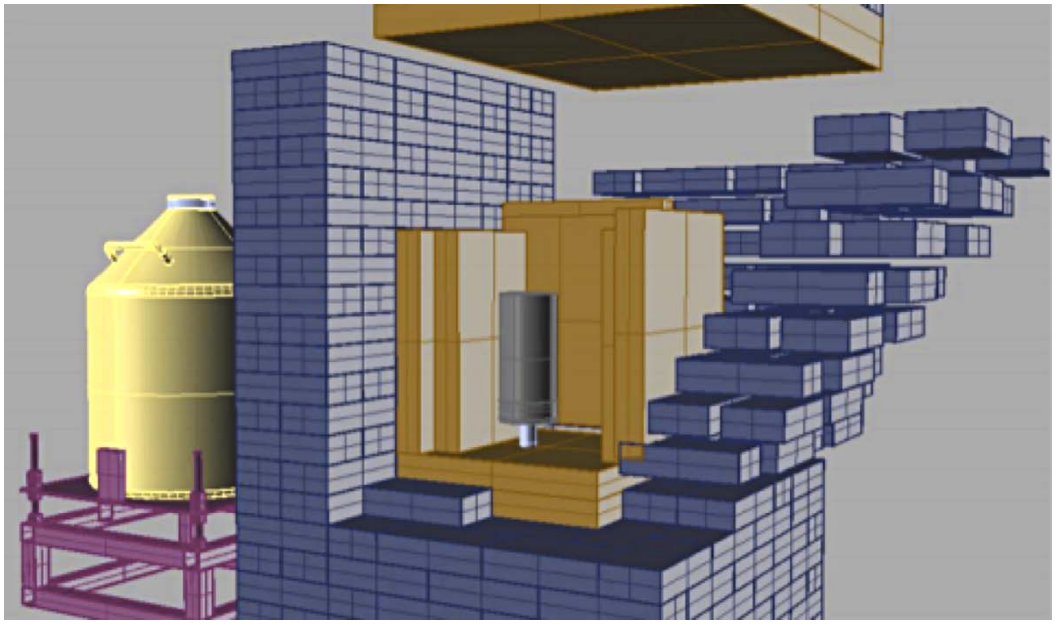

Figure 6.2.1: A schematic of the PandaX counting station in use at CJPL. A lead and OFHC copper shield are constructed to block EM radiation while a high purity germanium detector measures sample radioactivity. The radon background is reduced by surrounding the station with dry nitrogen flowing in an acrylic chamber. Figure from [84].

To reduce the radon level inside the counting station, a sealed acrylic housing surrounds the shield and is continuously flushed with dry nitrogen offgas at 7–10 L/min.

Key components (such as the inner vessel SS, outer vessel OFHC copper, and TPC components) of the PandaX-I detector were assayed in the counting station prior to its assembly to ensure that background rates would fall within the design allowance. The radioactivity rates for isotopes in the measured unit are compiled and used in a simulation of the detector in order to estimate the expected background. A table of expected rates for the major structures and the measured overall background is given in Table 6.5.

6.3 Monte Carlo Simulation

A custom simulation of the PandaX-I detector geometry and material properties using the GEANT4 library [81,82] was utilized to assay the background concerns during operation. The

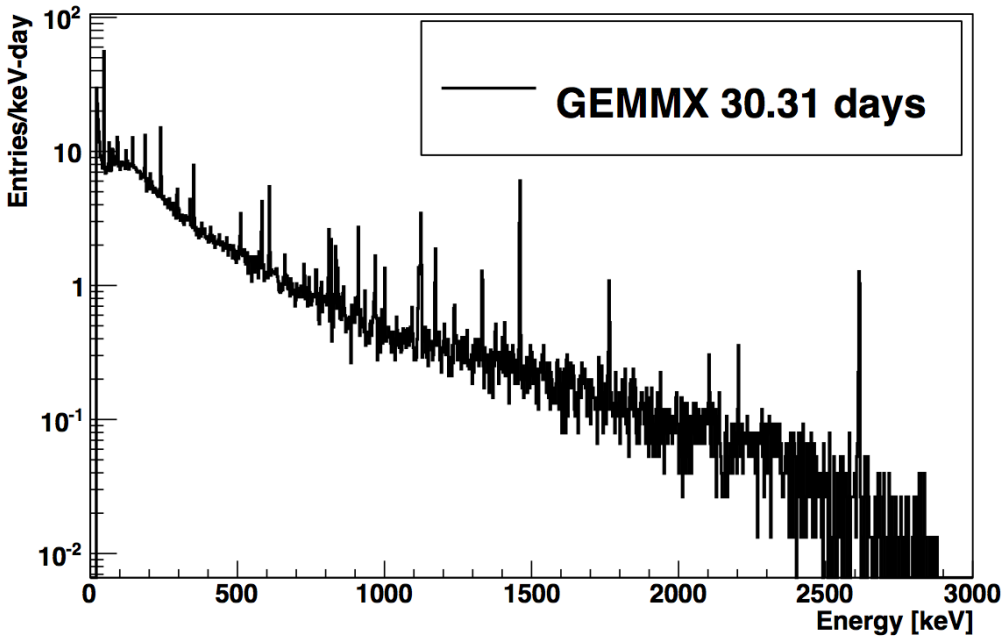

Figure 6.2.2: Background spectrum from the counting station high purity germanium detector. The spectrum shows an overall low background with a moderate contribution from ^{40}K. Figure from [84].

LXe volume inside the TPC is separated into two sensitive detectors, one which encompasses the entire region between the cathode and liquid surface while the other marks the region between the cathode and bottom PMTs. These are respectively called the drift region and the reverse field region (RFR). In the drift region an energy deposit will result in both an S1 and S2 signal being produced while interactions in the RFR will only produce an S1 signal. The distinction between the drift region and RFR does not affect the physics of the simulation, only in partitioning the data into a ROOT tree. The differentiation allows for easy identification of events with a typical nongaussian fluctuation known as gamma-X or neutron-X (which scatter once in the RFR and once in the drift region, producing two stacked S1 and a single S2, giving an artificially low S2-to-S1 ratio).

PMT windows are considered sensitive detectors for the case of impinging optical photons. This allows the GEANT4 model to serve a dual purpose as both an energy deposition and light propagation simulation tool. The energy depositions are quickly simulated by disabling photon propagation since the photon propagation required for a light simulation is markedly more computationally intensive. This property means a decoupled approach yields the best

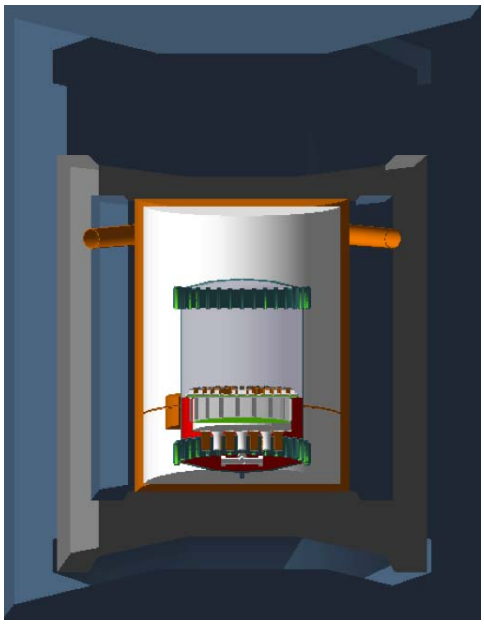

Figure 6.3.1: Visualization of the PandaX-I detector as built in the GEANT4 [81,82] library. The materials and physics simulation capabilities of GEANT4 allow for precise estimates of detector response and radioactive background studies.

result with currently available computation power. If the full detector response needs to be simulated then light propagation can be enabled, but if a knowledge of the location and energy of deposits is all that is desired the photon propagation can be suppressed to allow for a considerable increase in the number of events generated per unit CPU time, O(>1000) factor for high energy events.

The light simulation can be further decoupled into a realistic simulation of the light (S1) and charge (S2) signal, or merely a simplified model which releases a number of photons (linear with the energy deposited) isotropically at the interaction site. The realistic production of photons and ionization electrons is handled by the NEST [68] add-on library for GEANT4, while the default GEANT4 scintillation methods can be used for the production of less physically motivated photons. The additional models in the NEST library allow probing of detailed properties of an interaction in both the time domain and with physical fluctuations of signal quanta to give an overall view of how a detector may respond to impinging radiation. The standard scintillation method provides a precise tool to emit radiation in a known location with a known number of photons to allow for mapping out detector response with-

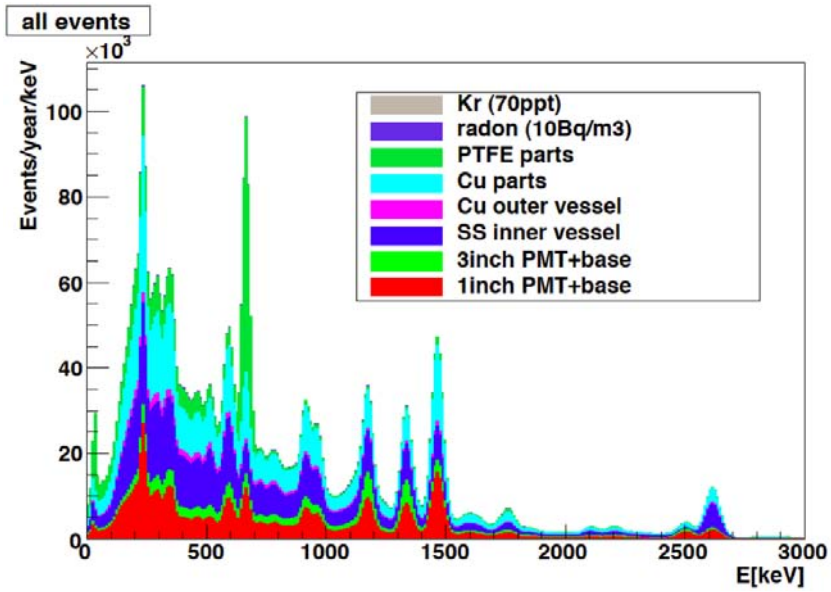

Figure 6.3.2: The simulated background spectrum of the PandaX-I using the GEANT4 [81, 82] library. Component activity measured by the counting station is input into the simulation to assess the spectrum in the fiducial volume. The energy deposition spectrum is smeared with $\sigma = 0.6\sqrt{E}$.

out added physical fluctuation. The standard GEANT4 scintillation removes the physical uncertainty caused by the LXe microphysics, allowing one to probe the intrinsic statistical uncertainty induced by the detector geometry.

6.3.1 Simulated ER Background

Electromagnetic radioactivity is simulated using the GEANT4 library radioactive decay method. Isotopes are placed in their respective volumes and allowed to decay. For instance, if a component has ^{40}K content, a ^{40}K atom is placed in the respective geometric volume, GEANT4 allows the isotope to decay, then the secondary particles are tracked. It is the secondaries that produce events inside the detector, e.g. energy depositions from alphas, betas, or gammas (see Fig. 6.3.2).

Data from the interactions in the sensitive volume caused by radioactive decay are recorded to a ROOT [83] file for later analysis. The data is analyzed using custom ROOT software to

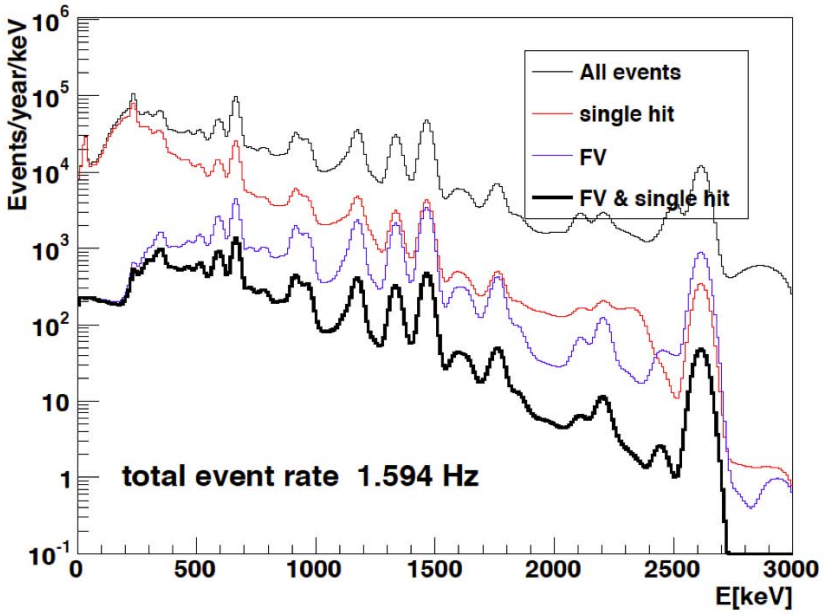

Figure 6.3.3: The simulated background spectrum in PandaX-I before and after analysis cuts. Single hit and fiducial volume cuts are performed and compared with the original smeared spectrum ($\sigma = 0.6\sqrt{E}$).

reveal the interactions which may produce background events in the detector. Interactions which take place in the drift region have their energy depositions clustered through a energy weighted average. Multiscatter events are cut to reveal only the single energy deposits in the target volume (see Fig. 6.3.3 for results of the cuts). A fiducial volume cut is done to remove events which occur in the outer skin of the target volume. A low energy threshold and high energy cutoff are placed on the data to coincide with a DM search energy window. This process gives an estimate for the total background of electromagnetic isotopes in the PandaX-I geometry.

6.3.2 Simulated NR Background

Estimation of the neutron rate consists of two parts. The fast neutrons generated by cosmogenic muons are simulated using a combination of the MUSIC [89] and GEANT4 code libraries. Neutrons resulting from radioactive decays (generally (α, n) reaction) within the vicinity of the laboratory are simulated with SOURCES-4A [90] and then propagated with

GEANT4. This approach probes both the high and moderate energy contributions to the ambient neutron background. Lower energy neutrons originating outside the shield do not need extensive simulation since they are captured readily in the outer polyethylene shield layer.

Muon induced neutrons are simulated using MUSIC software to propagate muons from the mountain surface down to lab. The topological data from the area surrounding CJPL supplies the geometry for muon simulation and the resulting energy and angular spectrum are utilized as input to GEANT4 software. The muon spectra allow generation of muon induced neutrons which may impinge upon the shielded detector. Neutrons that produce NR in the inner detector are tallied and a rate is estimated.

The neutron spectrum from radioactive decays in the surrounding lab and shield is simulated and the resulting neutron energy and angular spectra are fed into the GEANT4 detector simulation to estimate the neutron spectrum after each layer of polyethylene. After the second layer of polyethylene, a final neutron spectrum is used to generate NR events in the detector. The NR events found in the fiducial volume of the detector are analyzed to estimate the overall radioactive background. The estimated NR background rate is dominated by the stainless steel inner vessel and (α, n) in the PTFE (0.24 and 0.66 event/year, respectively). Rock and muon based NR background is less than 0.1 event/year, giving a total estimated NR background rate for PandaX-I of less than 1 event/year.

6.4 Measured Background

The Monte Carlo estimates can be compared to actual data seen in the detector during the PandaX-I live days. During Run5, 17.4 live-days of data was taken with which a background comparison can be made. The full analysis results of Run5 are detailed in Chapter 6.4.2 and the background spectrum from that analysis can be used.

6.4.1 Measured EM Background

The ER band seen in PandaX-I is flat across a large O(50 keV_{ee}) energy window. This result can be compared to the ER results from the background simulation effort. Table

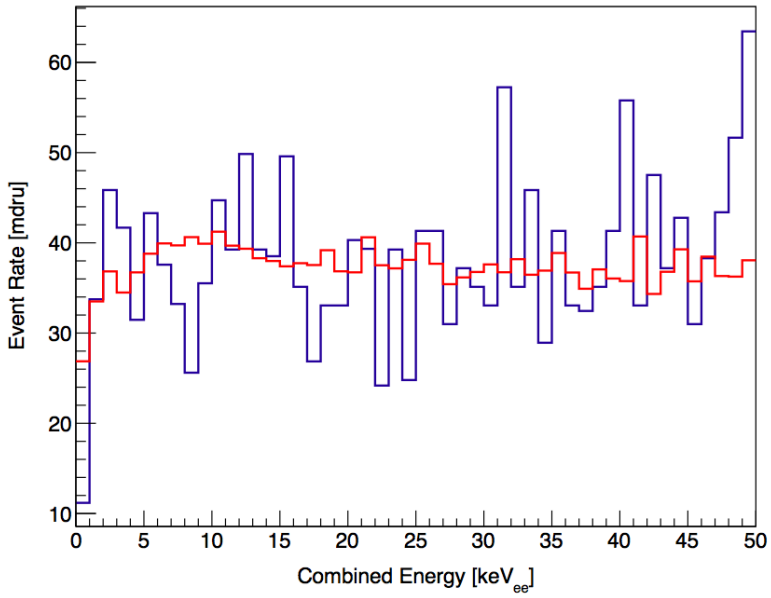

Figure 6.3.4: The remaining background spectrum after cuts in PandaX-I for Run5 (blue) and EM background simulation (red). The spectrum is flat in the energy window and matches well within statistical errors (see Table 6.5).

6.5 shows the contribution from each simulated component, and the aggregate is compared with the measured background. Simulation predicts a background of 43 ± 11 mDRU (event/day/kg/keV$_{ee}$) while PandaX-I saw a background rate of 32 ± 5, showing the two quantities in considerable agreement.

6.4.2 Measured NR Background

During the 17.4 live-days of Run5 there were no neutron-like events which passed all cuts (see Sec. 7.4). This result is consistent with the zero background interpretation for the data. The agreement between simulation and measurement for both ER and NR backgrounds helps confirm that the background is the PandaX-I detector is well understood and gives confidence when extending the reach of PandaX-I with a longer exposure.

Source	background level (mDRU)
Top PMT array	10.9 ± 1.8
Bottom PMT array	4.0 ± 0.6
Inner vessel components	18.5 ± 10.1
TPC components	2.3 ± 0.8
^{85}Kr	< 3.3
^{222}Rn and ^{220}Rn	2.7 ± 2.0
Outer vessel	1.3 ± 0.9
Total expected	43 ± 11
Total observed	32 ± 5

Table 6.5: Tabulated background level for components in the PandaX-I detector. Simulation results are shown and compared with the observed spectrum using 99.7% ER rejection efficiency. Note: 1 mDRU = 0.001 event/day/kg/keV$_{ee}$.

CHAPTER VII

PANDAX I: Data Analysis

The PandaX-I detector operates with the purpose of probing the WIMP-nucleon interaction cross-section. Once collection of a suitable dataset is complete, a full offline analysis must be done to tease the relevant result from the large collection of data. The detector must be fully calibrated in its function as a calorimeter, imager, and event discriminator, and the detector efficiency must be assessed once all selection criteria are chosen. The result of the PandaX-I effort is a substantial probe into the important low mass region of spin-independent WIMP-nucleon parameter space. The calibration, selection techniques, and subsequent results of this dark matter search are outlined in this chapter.

7.1 Calibration

The PandaX-I TPC must be calibrated to allow for reliable event reconstruction. Firstly, the response of the sole physics sensors (photomultiplier tubes) in the experiment must be probed. Then the TPCs ability to function as a calorimeter must be assessed by viewing the response of the detector to calibration sources of ionizing radiation. Additionally, with careful choice of calibration sources the experiment's position sensitivity and ER/NR discrimination ability can be probed.

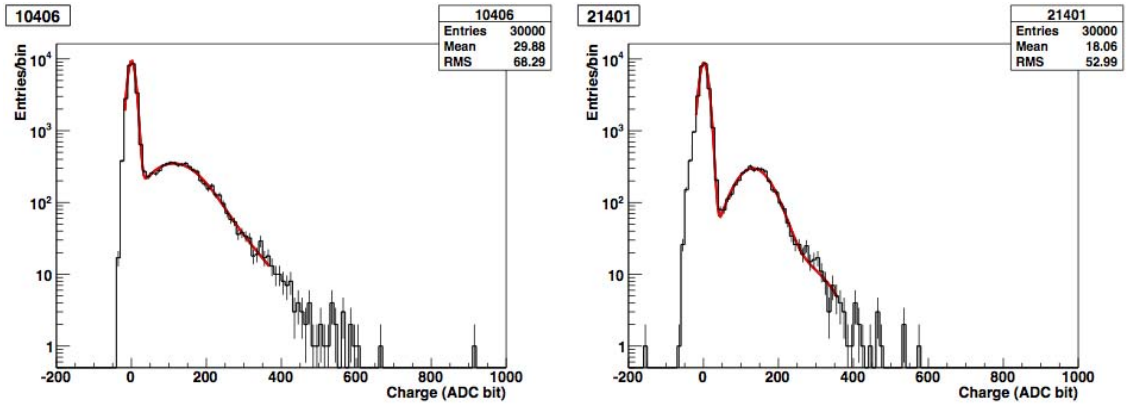

Figure 7.1.1: Left: Area spectrum of integrated LED pulses for a PandaX-I top PMT. Right: Area spectrum for LED pulses in a PandaX-I bottom PMT. Both top and bottom PMTs are calibrated in situ with sparse LED photons emitted from a fiber optic cable. The single photoelectron area and resolution calibration are determined by fitting gaussians to the noise and photoelectron peaks.

7.1.1 PMT Calibration

The photomultiplier tubes are calibrated using a 10 ns pulsed light emitting diode (LED) system coupled to a fiber optic cable which transports the photons into the detector. The fiber optic cable transverses two feedthroughs to pierce the outer vessel and inner vessels and uses a virgin PTFE tube as the light diffusing material on the inner surface of the TPC reflector. The nonuniformity of the illumination pattern is overcome by scanning a several volt range for the LED pulse. This ensures that at least one dataset will include the proper photon statistics for every PMTs. The LED calibration runs use the LED pulse as the trigger signal and less than 5% of the time a single photon will exist in the PMT waveform around the LED pulse time (low occupation), ensuring a good fit of the single photoelectron and noise peaks. A typical single photoelectron (SPE) fit for both a TPMT and BPMT is shown in Fig. 7.1.1. The average area of the SPE peak is used to scale all measured physical signal areas into the photoelectron (PE) unit for each PMT channel.

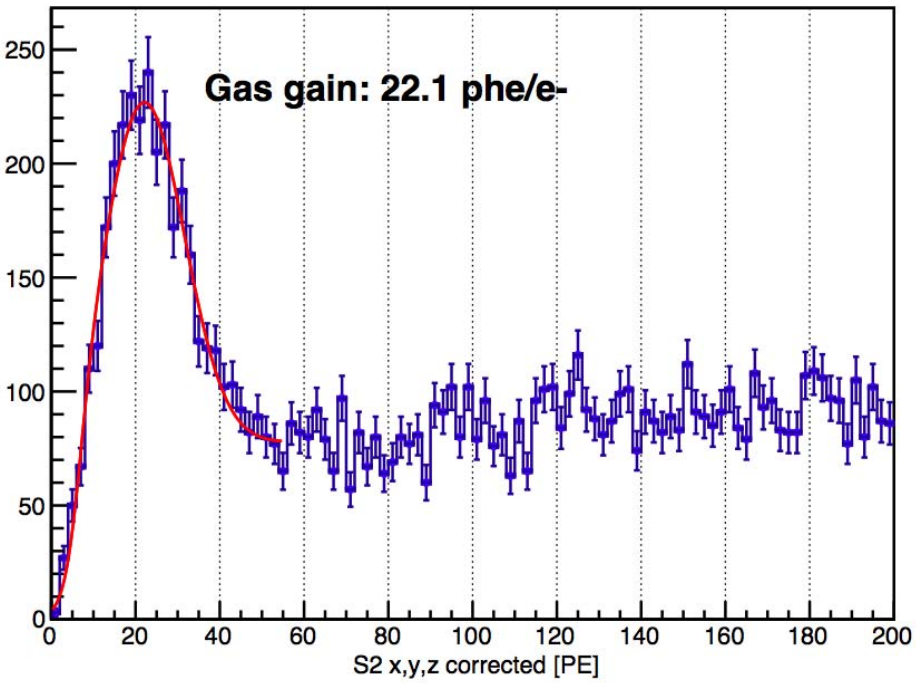

Figure 7.1.2: Single electron area and resolution calibration spectrum. Small S2 signals with a sparse S1-like topology are caused by single electrons being extracted and accelerated in the gas phase. The small S2 signals are identified and the peak at low energy is fit to obtain a gas gap gain of 22.1 PE/e^- with 45% resolution (FWHM).

7.1.2 Single Electron Calibration

Single electrons extracted from the liquid-gas interface undergo amplification in the gas gap region producing the S2 signal, as described in Sec. 3.4.1.3. Individual ionization electrons will produce a mean number of photoelectrons in the detector PMTs and it is possible for single electron S2 signals to be identified and analyzed to determine the mean S2 signal per extracted electron. To identify single S2 electrons, signals which are tightly clustered S1-like pulses are grouped together as a small S2. This analysis yields 22.1 PE/e^- (photoelectrons generated from a single extracted S2 electron). The fit can be seen in Fig. 7.1.2.

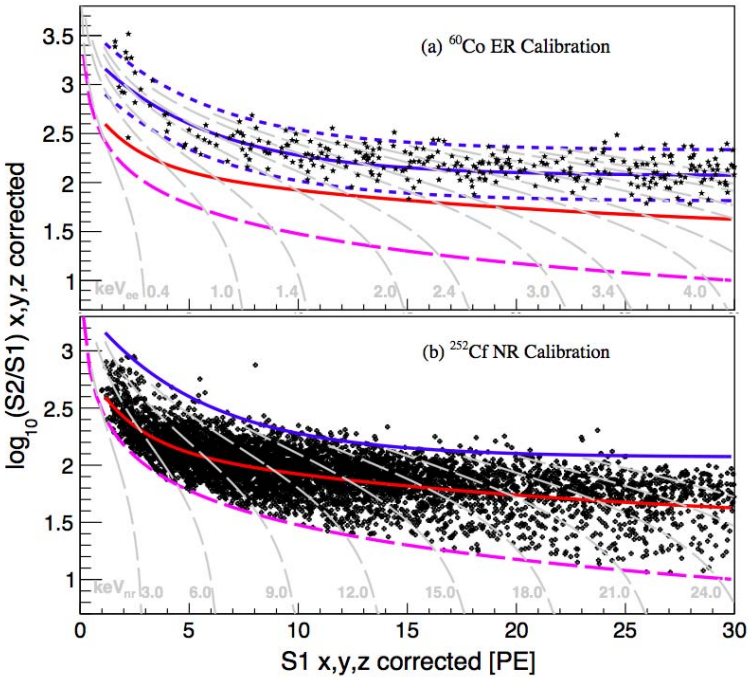

Figure 7.1.3: The $\log_{10}$(S2/S1) versus S1 spectrum for (a) ER and (b) NR calibration data with means (solid blue and red lines, respectively) and $\pm 2\sigma$ ER contours (dashed blue lines). The dashed magenta curve represents the 300 PE S2$_{bottom}$ cut. The gray dashed lines are the constant energy contours using the combined energy scale based on NEST [68, 69] and the measured PDE and EEE (see Sec. 7.2.3). Figure from Ref. [13].

7.1.3 ER Calibration

Both low energy and high energy electromagnetic calibration was undertaken. The high energy calibration was done with both ^{60}Co (662 keV) and ^{137}Cs (662 keV) radioactive sources. The sources are brought close to the detector using a hermetically sealed cable and tubing system. The tubing fed into the outer vessel and was wrapped on the surface of the inner vessel near the middle of the TPC. The light yield was determined by utilizing the ^{137}Cs full absorption events which occurred in the sensitive volume. The absorption peak is fit with a gaussian and monitored over time during brief calibration runs between dark matter data taking.

The low energy calibration relied on low energy scatters from a ^{60}Co source placed in the calibration system. The probability of low energy scatters from this source is very low and

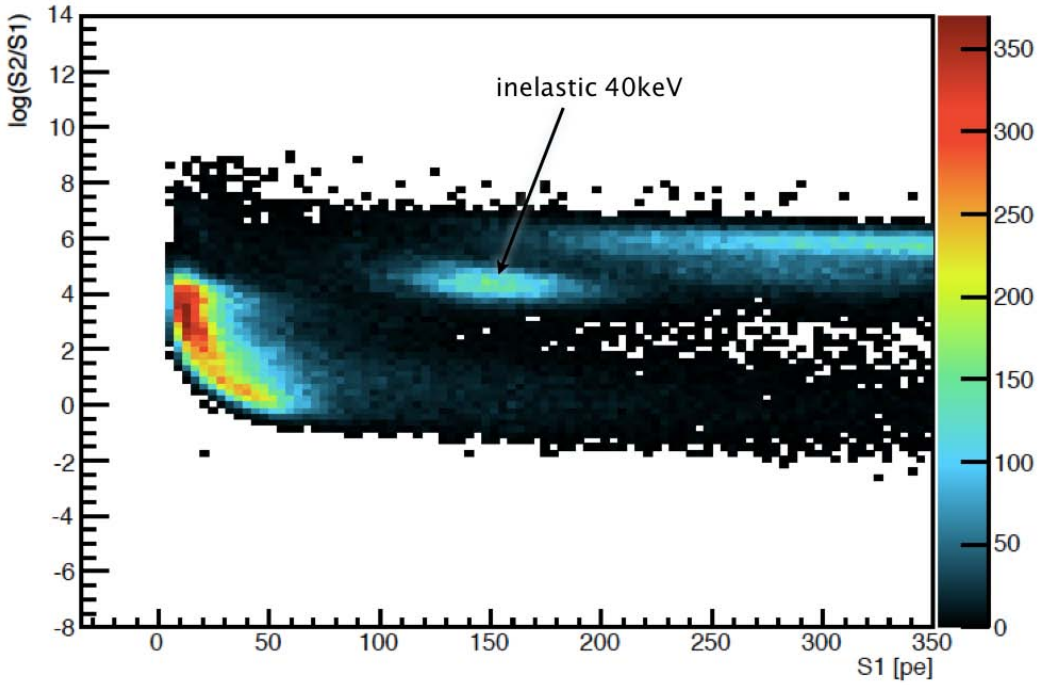

Figure 7.1.4: Neutron calibration $\log_{10}$(S2/S1) spectrum in the PandaX-I detector. A clearly defined inelastic 40 keV_{ee} signature is seen in the data. The inelastic events can be selected and used to calibrate the detector response properties. A spatial correction of S1 and S2 inhomogeneities can be produced as a result.

necessitated considerable data-taking dedicated to ^{60}Co runs, so a live-time of 135.4 hours for ^{60}Co data was taken over the course of the DM search period. Electron recoil events in the sub-100 keV range accumulated over that time span and allowed for estimation of the ER mean and variance across the low energy range.

7.1.4 NR Calibration

Nuclear recoil events must be calibrated with a source that primarily interacts through nuclear, rather than electromagnetic means. An ideal calibration source would provide a smooth single scatter spectrum with a distinct feature or two that is consistent across the detector's sensitive volume. We get the smooth NR spectrum properties with the ^{252}Cf radioactive source, but rely on an inelastic ER+NR peaks as our distinct energy-scale-setting

feature.

The ^{252}Cf ER+NR produces inelastic scatters at both 40 keV and 80 keV in the xenon target due to the metastable ^{129m}Xe and ^{131m}Xe states accessed via neutron scattering. The 40 keV scatter is especially distinguishable in the calibration data, as can be seen in Fig. 7.1.4. The smooth pure NR recoil band can also be seen in Fig. 7.1.4 at low $\log_{10}$(S2/S1). The ^{252}Cf spectrum does contain considerable ER recoil contamination due to impinging gamma rays released by the ^{252}Cf as a radioactive byproduct, but this contamination does not affect the measurement of quantities needed for NR calibration (after cuts are applied).

The smooth NR band is used to calculate the band median and variance to give a measure of the ER/NR discrimination after the measurement is coupled with the ER calibration. The NR band also allows calculation of the trigger and analysis efficiencies at low energy when compared with a Monte Carlo simulation. The ER/NR cut and the efficiency calculation are detailed in Secs. 7.4.1 and 7.3.8, respectively.

7.2 Event Reconstruction

The PandaX-I detector is both an imager and calorimeter of events. The energy reconstruction abilities are provided by the LXe properties for scintillation and ionization which produce quanta in proportion to the amount of energy deposited. The position reconstruction abilities originate from the time projection chamber topology, yielding time separated and patterned S1 and S2 signals which contain the position information. In order to utilize the imaging and calorimetry ability to obtain physically meaningful event quantities, the events must be reconstructed and corrected as is detailed in the following.

7.2.1 Position Reconstruction

Two methods of position reconstruction are employed to estimate the interaction location. A weighted average, or center of gravity (CoG), is used as a first estimate. Additionally, a neural network (NN) estimator is used to provide a more sophisticated machine learning technique which utilizes a Monte Carlo trained NN to estimate event locations in PandaX-I

data. The two methods are compared for consistency to determine if an event has an acceptable reconstruction.

7.2.1.1 Center of Gravity Method

The simplest approach to position reconstruction uses a weighted average of the product of the signal at a given PMT s_i with the PMT position (x_i, y_i) in two dimensions, as in

$$\vec{r}_{xy} = \sum_i s_i x_i \hat{x} + s_i y_i \hat{y}.$$

The center of gravity approach relies on a simple, understandable model which has known shortcomings but reasonable performance in fiducialization. Comparing the CoG reconstruction of the top and bottom arrays separately allows an opportunity for discrimination of undesirable events. A more sophisticated NN machine learning approach was employed to verify the efficacy of the CoG method. The CoG method does tend to systematically stack events near the TPMTs, due to large portions of the signal being absorbed by a single TPMT in a single event, but the error is only a few cm at worst and is deterministic (so it can be removed using Monte Carlo comparison techniques such as a likelihood fit).

7.2.1.2 Neural Network

The neural network machine learning approach was used to provide an estimate for event position based on the signal pattern in the PMT arrays. A back propagating neural network utilizing the FANN [91] library was trained on GEANT4 [81, 82] Monte Carlo generated data. The Monte Carlo data was generated using an optical photon simulation in a software depiction of the PandaX-I detector, modeled using the GEANT4 geometry and materials library. One million events with high photon count were produced and used to train the NN.

7.2.2 Position Dependent Signal Correction

Once the position of the event has been determined the position-based corrections can be applied to the signal. The uniformly distributed ^{252}Cf-induced 40 keV inelastic energy de-

posits are easily identified and can be used to determine the amplitude corrections necessary for both S1 and S2. A large neutron calibration dataset was taken and analyzed to produce the following corrections.

7.2.2.1 S1 Correction

Nonuniformity in S1 response originates from geometric effects, local PMT failures, and local electric field differences. These nonuniformities must be corrected in order to provide the best detector energy resolution. The S1 signals from energy deposits are distributed throughout the LXe target volume, so the interesting events can in principle originate in any position in three-dimensional space. Additionally, the detector response across the detector volume will vary, even at identical energies. This necessitates a three-dimensional correction to the S1 signal. A large number of monoenergetic energy deposits from 40 keV inelastic interactions have their S1 signals selected in analysis then mapped to determine the detector response. The normalization and inversion of this map can then be applied to all signals to provide the S1 correction (see Fig. 7.3.2 for a visualization of the S1 x-y correction).

7.2.2.2 S2 Correction

Nonuniformity in the S2 signal can originate from several sources, such as geometric effects, irregularities in physical structure, or failed local PMTs, and must be corrected to provide the best detector energy resolution.The S2 signal correction can be treated in a similar fashion to the S1 correction mentioned above, but with a slightly more complicated approach since the S2 signal is generated with a different mechanism (in a planar gas gap, after drifting a distance in LXe). The S2 signal is not produced in a three dimensional volume, as is the case with the S1 signal. Additionally, the signal generation region for S2 signals is planar in nature (at the liquid-gas interface), rather than a three dimensional volume as for the S1 signals. This necessitates a two-dimensional correction in x-y to remove nonuniformities from the planar configuration.

There is an additional correction for S2 for the electron lifetime which must be considered (see Sec. 7.3.1). The S2 signal suffers a reduction of amplitude as a function of depth from interaction of the electron cloud with impurities. This effect can be easily corrected after

modeling with an exponential fit. See Figs. 7.3.3 and 7.3.1 for visualization of the S2 x-y and z corrections.

7.2.3 Energy Reconstruction

Reconstruction of event energy can be done using different methods. The most common uses S1 with a linear scaling across all energies but another higher resolution scale, the combined energy scale (CES), has come into use as well. The S1 only scale is well established but has energy resolution shortcoming over a large energy range. The CES is well defined with good resolution at higher energies (> 10 keV$_{ee}$), but it suffers from low S1 resolution in the DM search region O(1 keV$_{ee}$).

7.2.3.1 S1 Energy Scale

The energy reconstruction typically used at low energies in dual phase LXe detectors is based solely on mapping the event's measured S1 to the average energy which corresponds to that S1. The light yield L_y^{122} (units of PE/keV$_{ee}$) is calculated at 122 keV$_{ee}$ and used across the entire energy spectrum to reconstruct ER events using

$$E_{ee} = \frac{L_y^{122}\mathrm{S1}}{S_e}.$$

All events (ER and NR) are reconstructed this way, but the NR event energies will be incorrect due to Lindhard and drift field quenching. To remedy the quenching faced by NR events, one must rescale the E_{ee} quantity into E_{nr} using

$$E_{nr} = \frac{1}{\mathscr{L}_{eff}} \frac{S_e}{S_n} E_{ee}.$$

A detailed outline of the S1 energy reconstruction method with quenching factors is found in Appendix A. Here, we use L_y^{122} as the photoelectron specific constant of proportionality referred to as ϵ in the appendix. The NR reconstruction in PandaX-I is done using the NEST model $\mathscr{L}_{eff}$ [68,69] for the energy-dependent effective Lindhard factor. Both ER and

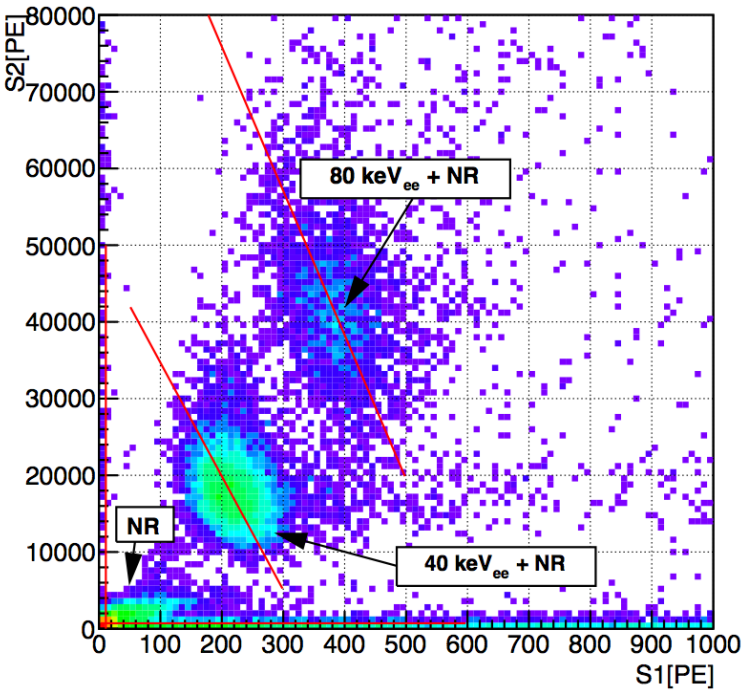

Figure 7.2.1: The S2 versus S1 distribution from ^{252}Cf calibration data. The horizontal and vertical lines close to the axes indicate the average NR contribution that is subtracted from the inelastic peaks when performing the anti-correlation fit. The diagonal lines are the result of a fit to the major axis of the identified peak ellipses. The slope of the line helps determine key detector response parameters (PDE, EEE) using the combined energy scale reconstruction. Figure from Ref. [13].

NR reconstructions use the field quenching factors $S_e = 0.54$ and $S_e = 0.94$ at 667 V/cm, calculated using Ref. [92].

7.2.3.2 Combined Energy Scale

There exists another energy scale which is particularly beneficial for increasing the energy resolution and determining detector response parameters precisely, termed the combined energy scale [93–95]. Reducing the S1 and S2 signals into their elementary quanta is the first step. The S2 is inverted from PE to the elementary unit of ionization electrons N_i to give the number of ionization electrons created in the interaction. The same is done for S1 to give the number of photons (decaying excitons) N_{ex} in the original interaction. The work

function for an ionization electron and exciton can be taken to have the same work function $W = 13.7$ eV (see Sec. 3.5.1), so that

$$E_{dep} = W(N_i + N_{ex}),$$

with E_{dep} as the deposited energy, N_i the number of ionization electrons, and N_{ex} the number of excitons (S1 photons). The quantities N_{ex} and N_i can be factored into

$$N_{ex} = \frac{S1}{\alpha} \text{ and } N_i = \frac{S2}{\beta},$$

where α is the photon detection efficiency (PDE) and β is the product of the electron extraction efficiency (EEE) and the S2 gain (22.1 PE/electron). The coefficients can be estimated by fitting the major axis of the elliptical peak caused by a monoenergetic source. The slope of the fit line is $-\beta/\alpha$, as in

$$\text{S2} = -\frac{\beta}{\alpha}\text{S1} + \frac{\beta E_{dep}}{W}.$$

The peak from 40 keV inelastic neutron collisions was fit to obtain $\alpha = (0.105 \pm 0.004)$ PE/photon and $\beta = (17.6 \pm 1.55)$ PE/ion. This gives a β which corresponds to an EEE of $(79.8 \pm 7.0)\%$.

7.3 Detector Performance

An understanding and characterization of the detector performance must be acquired in order to trust the result of event reconstruction in data analysis. With this in mind, important properties such as the overall light and charge yield, position and energy resolution, and event acceptance are determined through analysis techniques. Inhomogeneities and minor anomalies found in the data can then be categorized and corrected through systematic efforts.

7.3.1 Electron Lifetime

Not every electron from the drifting ionization cloud survives the journey to the xenon liquid/gas interface. The LXe target has a small population of electronegative impurities which may be encountered by a drift electron along its path (see Sec. 3.4.1.2). As a result of the impurities' electron affinity, ionization electrons are captured as they travel through the liquid, diminishing the S2 signal as a function of distance travelled. The survival of electrons as a function of distance follows a decaying exponential, with a characteristic electron drift length of l_e. Since the velocity of the drifting electrons in LXe is constant, this characteristic length can be converted to a lifetime $t_e = \frac{l_e}{v_d}$. The lifetime interpretation is useful since the actual quantity measured in the detector is the time between S1 and S2, i.e. the drift time. The reduction of electrons as a function of drift time can then easily be corrected by inverting the relation

$$S2_{measured} = S2_{actual} e^{-t/t_e}.$$

The quantity t_e can be measured with monoenergetic events that are scattered throughout the detector sensitive volume (see Fig. 7.3.1). The 40 keV inelastic peak from the ^{252}Cf runs is used to measure the electron lifetime as $t_e = 264.4 \pm 3.1$ μs, allowing for a z correction to be applied to the S2 as noted in Sec. 7.2.2. In practice, a linear fit can be used for the correction in offline analysis.

7.3.2 Light Yield

Since PandaX-I operates with an electric field across the drift region, the S1 signal is quenched (see Sec. 3.5.9.1). The quenched property requires that the mean of the S1 absorption peak be measured to determine the quenched light yield (with drift field applied). The unquenched light yield can then be determined by using a quenching model to invert the measured quantity. The total absorption peak from the ^{137}Cs calibration data can be used to monitor the light yield in the outlined way during the run.

To determine the light yield for PandaX-I, the 40 keV inelastic peak induced with by ^{252}Cf source is fit to obtain a result of 5.13 ± 0.2 PE/keV$_{ee}$. Using the NEST [68, 69] model of

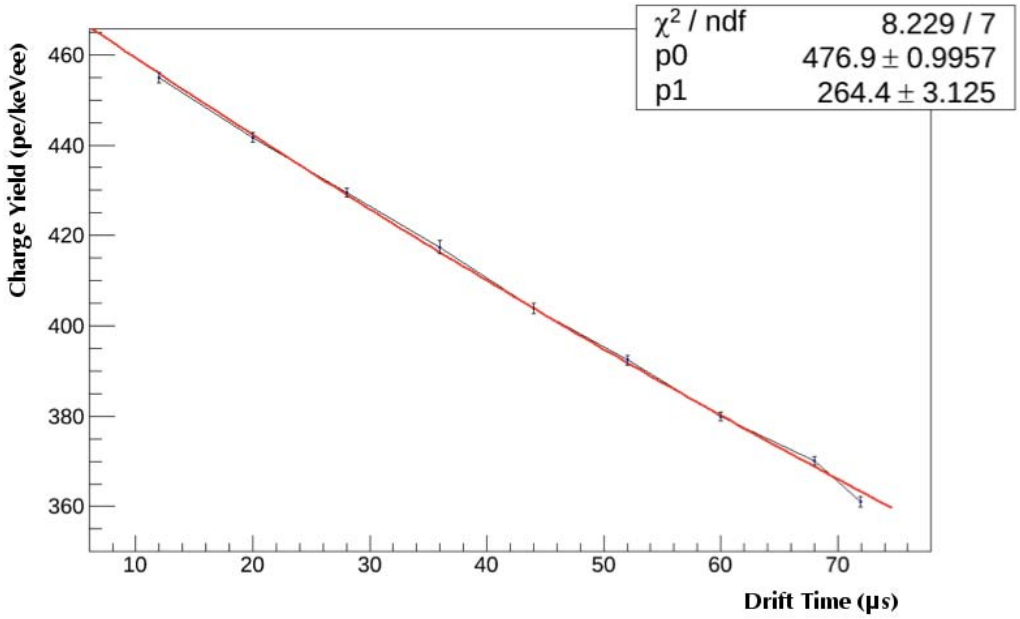

Figure 7.3.1: The charge yield dependence on the depth of the interaction. Deeper interactions will have smaller S2 signal since drifting ionization electrons are captured by impurities in the xenon. The effect can be corrected using a linear fit if the effect is small (exponential if the effect is large).

quenching, the known drift field of 667 V/cm, and the energy dependent correction to map the light yield at 40 keV_{ee} to 122 keV_{ee} (^{57}Co), we obtain a light yield of $\text{L}_y^{122} = 7.3 \pm 0.3$ PE/keV_{ee}. A two dimensional light yield correction map is then generated from the measured average light yield in x-y to correct for position dependence of S1 (see Fig. 7.3.2).

7.3.3 Charge Yield

The charge yield for the PandaX-I experiment can be determined in a similar fashion to that of the light yield. The extracted electron gain was determined in Sec. 7.1.2 and used in this calculation to relate photoelectrons to the actual number of extracted electrons due to ionization. A spectrum of the S2 signal for the ^{252}Cf calibration source has the 40 keV peak fitted to determine the signal mean. Then, a two dimensional charge yield correction is generated in x-y to correct for position dependence of S2 (see Fig. 7.3.3).

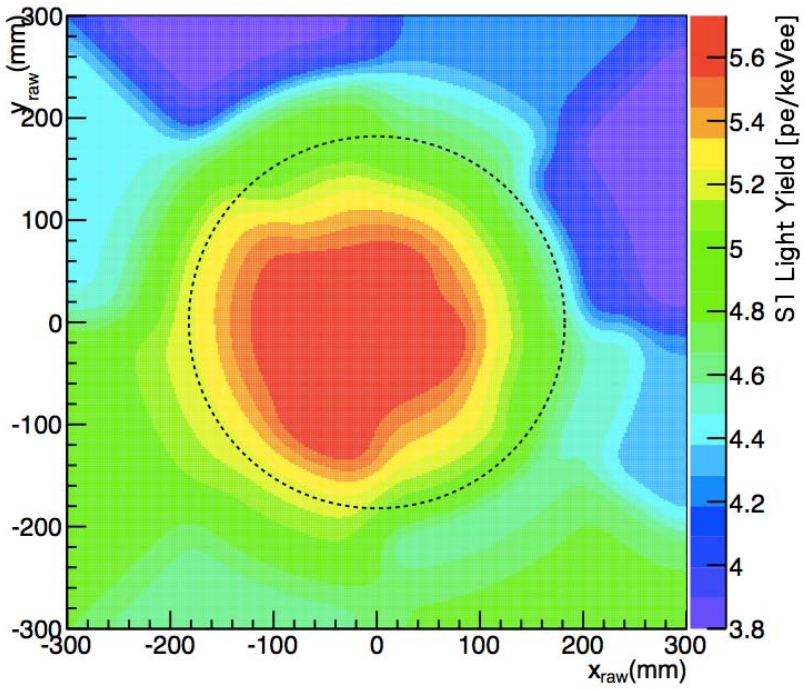

Figure 7.3.2: Light yield of the PandaX-I detector in the x-y plane. The central region tends to have high light collection efficiency since the photons reflect less often before being absorbed in the PMTs. The S1 light yield map can be inverted to correct for S1 position dependence.

7.3.4 Energy Threshold

In a dual phase LXe TPC which uses gas amplification, the energy threshold is set by the lowest determinable light signal (S1), not by the charge signal threshold. Accordingly, the light yield is the quantity which determines the ultimate low energy limit of the detector. In the case of PandaX-I, the very high light yield allows for a signal threshold on ER signal down to 2 PE, corresponding to an energy threshold of 0.5 keV$_{ee}$ (the upper cutoff of 30 PE is at 5.5 keV$_{ee}$). Through the use of the NEST $\mathscr{L}_{eff}$ [68, 69], this energy threshold can be mapped to the nuclear recoil equivalent of 4.1 keV$_{nr}$ (the upper cutoff is at 31.6 keV$_{nr}$), which serves as the ultimate low energy threshold for PandaX-I.

The S2 low energy threshold ($\approx$ 2 keV$_{nr}$) is even lower than the S1 threshold. This is due to the greater number of charge quanta that are released and measured from an interaction in LXe. However, the better energy threshold for charge does not assist in lowering the energy

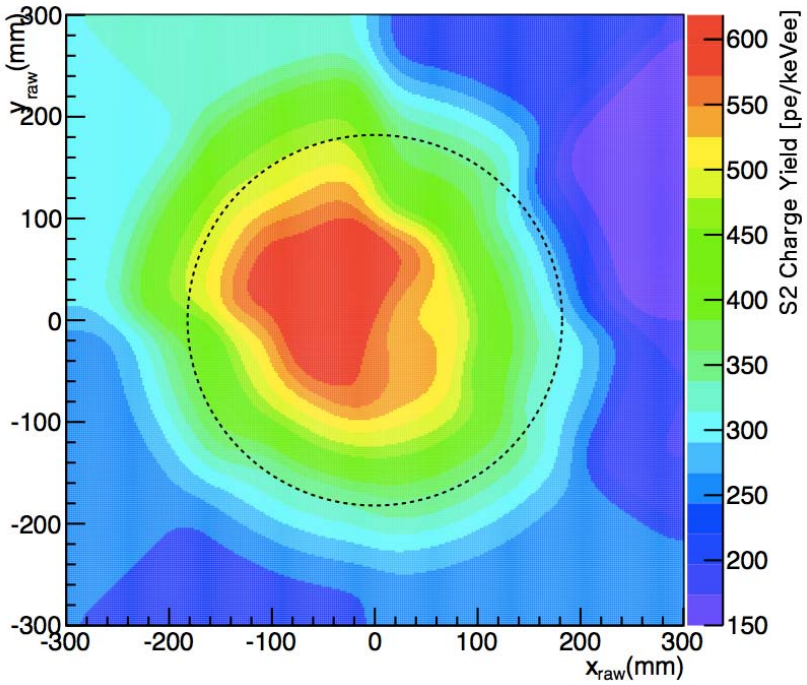

Figure 7.3.3: Charge yield of the PandaX-I detector in the x-y plane. The central region has high light collection efficiency since the S2 photons generated there enjoy a lensing enhancement from xenon's high index of refraction and a shortened path length from reduced reflections. The S2 light yield map can be inverted to correct for S2 position dependence.

threshold for the standard WIMP search since the ER/NR discrimination (using the S2/S1 ratio) becomes unreliable at energies below the S1 threshold. A specialized analysis would have to be performed in that case.

7.3.5 Energy Resolution

To find the ultimate energy resolution of the detector, the combined energy scale must be used. If using the combined energy scale, the ^{252}Cf full absorption peak energy resolution is 8.7% at 40 keV$_{ee}$. At the lower energies of the WIMP dark matter search, the S1 uncertainty from photon collection variance dominates the statistics, worsening the energy resolution.

7.3.6 Position Resolution

The position reconstruction when using solely the center of gravity method (CoG) provides a fairly high position uncertainty. However, when a neural network (NN) based approach is used the combined uncertainty across the fiducial region is below 8 mm. When the CoG and NN position reconstruction algorithms differ by more than 4 cm the event is discarded. Events that have this cut criterion are typically ill-formed S2 signals which do not produce a localized signal in the PMT arrays.

7.3.7 Background Rejection

Rejection of background is done through data quality considerations, an energy window cut, single scatter cut, a fiducial volume selection, and an ER/NR cut. When all criteria are applied, the overall rejection of undesirable events is 99.999% (see Table 7.6 for detailed cutflow quantities). However, the background rejection of a dual phase xenon detector is usually given based on the final ER/NR cut with rejection typically sitting in the high ninetieth percentiles for most detectors. Using the ER and NR band means and variances in the PandaX-I detector, an estimate across the energies of the WIMP search window of 99.7% rejection of ER events was obtained.

7.3.8 Nuclear Recoil Detection Efficiency

The overall event detection efficiency is the combination of cut efficiency ϵ_{cut} and signal acceptance A of the NR signal window. The cut efficiency ϵ_{cut} includes the identification and quality cut efficiencies on both S1 and S2, and the trigger efficiency on S2 signals. The S1 identification and quality cut efficiencies are evaluated using the low-intensity LED data. The S2 quality cut efficiency due to the bottom-to-top-charge-ratio cut is evaluated by selecting events located near the NR band mean and taking the ratio of events with and without the cut. Finally, the S2 trigger efficiency is obtained by fitting the measured S2 NR spectrum while assuming an exponential form for the true energy spectrum (see Fig. 7.3.4). The acceptance of S2 signals does not drive the low energy threshold since 200 PE is well below the S2 equivalent of the 2 PE low energy cutoff chosen for S1.

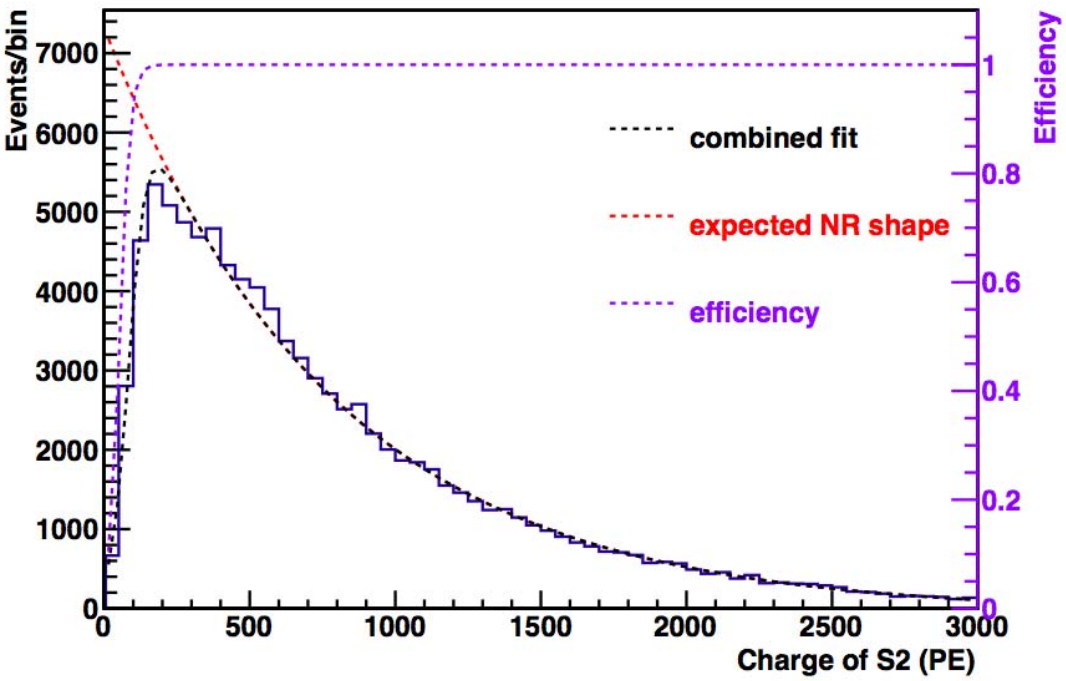

Figure 7.3.4: Low energy S2 spectrum for NR events in the PandaX-I detector. The spectrum follows an exponential form with low energy cutoff. This behavior is fit and the efficiency (purple) is calculated by comparing the fit curve (black) to the expected NR shape (red dashed).

Combining these, ϵ_{cut} is found as a rising function of S1 with a maximum of about 70% at 25 PE, and falling gradually due to the pulse-height-to-area-ratio quality cut on the S1 waveform (see Fig. 7.3.5). Results consistent with the measured cut efficiency are obtained by taking the ratio of the measured NR spectrum to the expected spectrum from the Monte Carlo simulation, including the contribution due to the 300 PE bottom S2 cut.

The corresponding signal acceptance A is defined as the ratio of the number of NR events below the mean (i.e. average) of the NR band to the total, also shown in Fig. 7.3.5 together with the overall efficiency. The change of the acceptance as a function of S1 is due to changing mean separation of the $\log_{10}$(S2/S1) distribution for the ER and NR bands in different S1 slices. The events in the NR band with suppressed S2 may be due to multiple-scattered neutrons that deposit partial energy below the cathode, so called neutron-X events. Using double-scatter neutron events with the second scatter in the very bottom layer of the TPC as

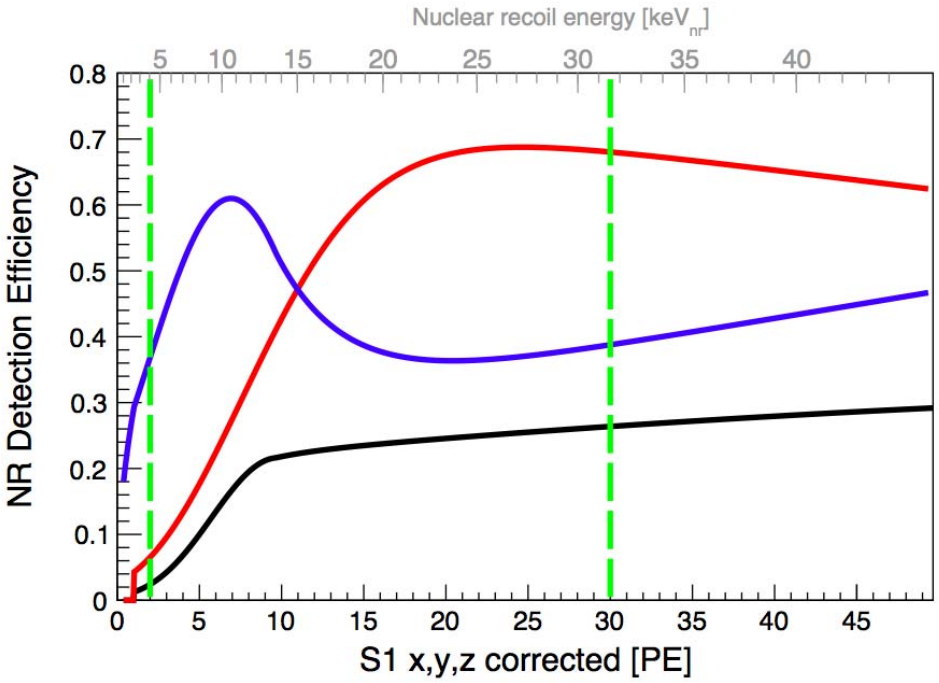

Figure 7.3.5: The acceptance and efficiency curves for the 17.4 live-day analysis in PandaX-I. The blue curve is the NR acceptance below the NR mean, the red curve is the analysis efficiency, and the black represents the total combined acceptance. Vertical dashed lines show the WIMP search energy window. The linear bottom scale is in photoelectrons while the nonlinear top scale is the energy in keV$_{nr}$, mapped using the NEST $\mathscr{L}_{eff}$ [68,69]. Figure from Ref. [13].

a proxy, we estimate that below-cathode events could lead to a maximum fractional reduction of 25% to the overall NR detection efficiency from shifting the mean downward.

7.4 Analysis Results

After detector calibration an analysis of the dark matter run data can be completed. A series of simple cuts are placed on the non-blind data to select events which could be signal. Acceptance of the software cuts is calculated as a function of energy and a comparison is made between the residual events and background prediction. A WIMP-nucleon exclusion curve is calculated from the dark matter search results from PandaX-I operation as reported

in Ref. [13].

7.4.1 Event Selection

During the 17.4 live-day run, over four million events were collected. The vast majority of these events are background or artifacts which must be identified and removed to reveal the signal. A series of cuts are placed on the data which identifies the uninteresting events. First, a data quality cut is enforced which requires all channels to be operating in a normal state before and after the event happens. Also, large noise events are removed by this cut and the event is required to have at least one S1 and S2. A single site cut is then placed on the data which removes events that have more than one identified S2 (multiple scatters).

Event selection	# events	rate [Hz]
all triggers	4,062,609	2.70
quality	1,877,707	1.25
single-site	1,195,119	0.80
S1 range (2-30 PE)	10,268	6.8×10^{-3}
$S2_{bottom}$ range (300-20,000 PE)	7,638	5.1×10^{-3}
fiducial volume	46	3.1×10^{-5}

Table 7.6: The cutflow for the 17.4 live-day PandaX-I analysis. Several cuts are placed on the dataset which result is 46 candidate events, none of which survive the ER/NR cut. Table adapted from Ref. [13].

An energy cut is performed to remove all high energy events and events with sub-threshold S1 signals. The energy window cut removes a large fraction of events since the vast majority of background is of high energy (events with energies from 5 keV_{ee} up to multiple MeV_{ee} are cut). An $S2_{bottom}$ cut is placed on the data to remove events which produce less than 300 PE in the bottom PMT array and a similar cut removes events with more than $20,000$ PE. This selection removes the few events at low energy which have an abnormal asymmetry between the top and bottom PMT S2 signals. A fiducial volume selection of 37 kg xenon mass is made which removes events that occur near the surface of the detector, dropping the total number of events to just 46. A tabulation of the cut flow for the selection process is shown in Table 7.6.

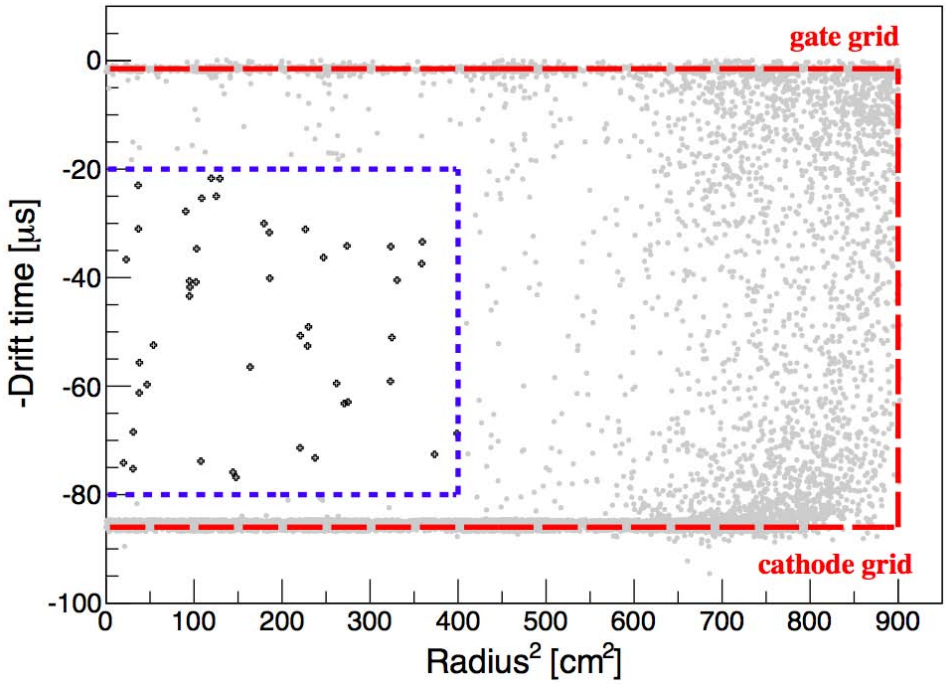

Figure 7.4.1: Event distribution in r^2-z for events in the 17.4 live-days data, prior to the fiducial and ER/NR cuts. The red dashed box shows the sensitive volume boundary. The 37-kg fiducial volume is contained within the blue dashed box, leaving 46 events remaining. None of these events survive the ER rejection cut. Figure from Ref. [13].

A final discriminatory cut is then placed on the data which determines if the event was generated by an electron recoil (i.e. background) or if the event is caused by a nuclear recoil (i.e. signal). The mean of the nuclear recoil band is the curve under which events must fall in order to be labeled as a nuclear recoil signal event. In the PandaX-I 17.4 live-days run data, no events survive the ER/NR rejection cut.

The absence of signal events has two significant interpretations. Firstly, there is not a significant background problem in the PandaX-I detector. A great deal of effort was spent to reduce the background rate to an acceptable level. That performance mark was achieved. Secondly, there is a lack of WIMP signal in the data. The result is not unexpected since the results from XENON100 [96] and LUX [10] were negative at similar exposure levels as PandaX-I. However, the lack of a DM signal allows for the generation of an exclusion curve which can be added to the world landscape for the discovery of dark matter.

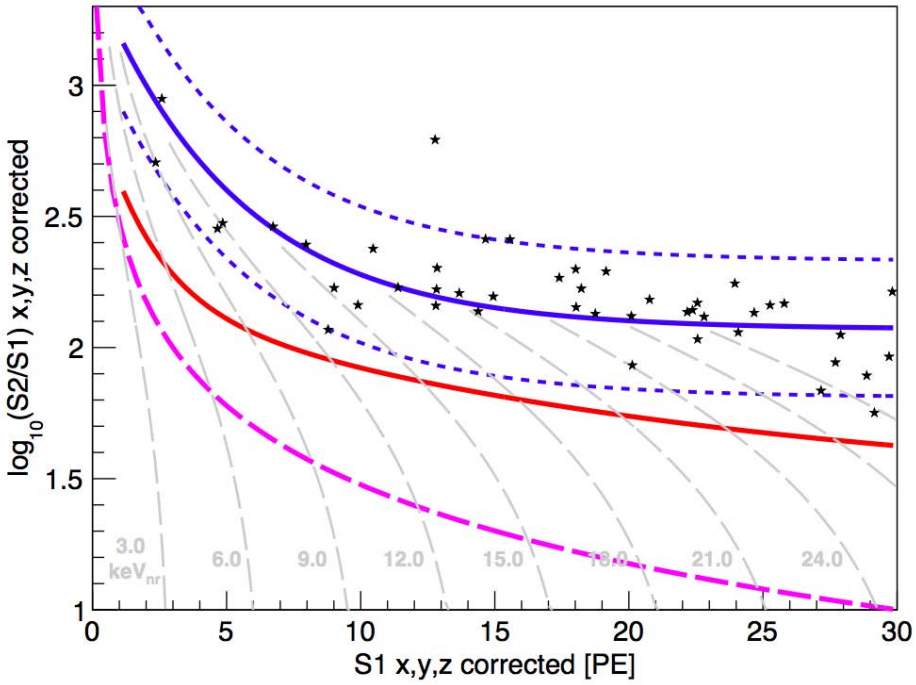

Figure 7.4.2: The $\log_{10}$(S2/S1) versus S1 distribution of events in 644 kg-days of DM search data. No event lies in the signal region after ER/NR cut. The curves are the same as those defined in Fig. 7.1.3. Figure from Ref. [13].

7.4.2 WIMP-Nucleon Spin-Independent Exclusion

7.4.2.1 Sensitivity Consideration

Direct detection of WIMP-nucleus scattering must take into account the general detector properties outlined in Sec. 1.3.1, but there are a number of specific considerations in addition to the general properties. WIMPs can scatter off a nucleus with two canonical interactions: one which depends on the net spin of the nucleus and another which depends on the nucleon count. The interactions are termed spin-dependent (SD) and spin-independent (SI), respectively. The spin-dependent WIMP-nucleon interaction could be studied with the PandaX-I detector since xenon has a significant fraction of naturally occurring isotopes with an overall nuclear spin. However, in this work, the probing of the spin-*independent* WIMP-nucleon cross-section $\sigma^{SI}_{N\chi}$ with the PandaX-I detector is the focus.

Xenon is particularly well suited to the task of detecting WIMPs through the spin-independent

interaction. The target has a very high light and ionization yield, is transparent to its own scintillation light, and can be purified to allow for efficient charge readout. Additionally, the high density of 3 g/cm^3 and intrinsic low radioactivity of the noble gas make it an excellent rare event detector. The large atomic mass of xenon $A_{Xe} = 131.29$ amu is also a boon for WIMP discovery since the spin-independent cross-section has a strong A^2 dependence, making xenon much more attractive than lighter elements.

There are challenges to overcome with the xenon detection medium, however. With the strong A^2 enhancement comes a quantum mechanical decoherence of the interaction associated with the nuclear size. This property is captured in the form factor, a model for the suppression of the WIMP-nucleus interaction as a function of transferred momentum. Due to the form factor effect, xenon detectors must be carefully built to provide high light yield in order to allow for low energy thresholds. The A^2 advantage starts to be lost due to form factor suppression for energies above O(10 keV$_{nr}$), so xenon detectors must strive to have energy thresholds well below this to fully harness their advantage. A more thorough discussion of the sensitivity calculation for Earth-borne detectors is detailed in Ch. 2.

Calculating the sensitivity of a direct detection experiment requires a careful assessment of detector capabilities and properties of dark matter in the local vicinity of the Earth. Detector properties such as the amount of target material, target nuclear mass, energy threshold, detector resolution, and duration of operation factor heavily into the discovery power of the experiment. Additionally, the details of the particle physics interaction play an important role. Finally, the local dark matter properties like density, typical particle velocities, shape of galactic halo, and our location in the halo are key for determining sensitivity to the WIMP-nucleon cross-section.

7.4.2.2 Sensitivity Result

To determine the spin-independent WIMP-nucleon scattering cross-section as a function of WIMP mass, the WIMP event rate is calculated based on the standard isothermal halo model [55, 97] with a DM density of 0.3 GeV/c^2/cm^3, a local circular velocity of 220 km/s, a galactic escape velocity of 544 km/s, and an average earth velocity of 245 km/s. After modeling detection efficiencies, Poisson fluctuation in the S1 signal is applied to smear the

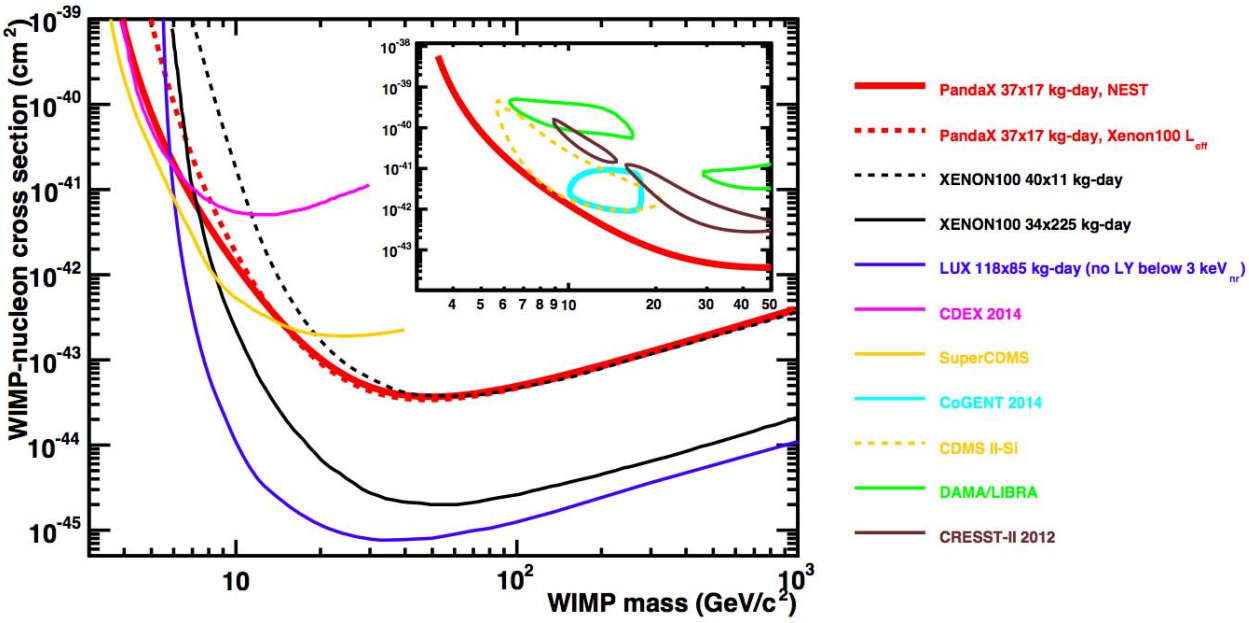

Figure 7.4.3: The 90% C.L. upper limit for spin-independent isoscalar WIMP-nucleon cross-section for the PandaX-I experiment (red curves): PandaX-I using E_{nr} and S1 mapping from NEST [68, 69] (red solid) and using $\mathscr{L}_{eff}$ from Ref. [96] (red dashed). Recent world results are plotted for comparison [1–12, 96]. The inset shows the PandaX-I result plotted with the detection contours, showing the exclusion of all claimed positive reports. Figure from Ref. [13].

S1 acceptance. The 90% C.L. upper limit of the DM signal is calculated from the Feldman-Cousins statistical model [59] for the case of no observed events and an expected ER Gaussian leakage background of 0.15 event. For a more conservative DM limit, we did not add the gamma-X estimate into our expected background. The lowest cross-section obtained is 3.7×10^{-44}cm^2 at a WIMP mass of 49 GeV/c^2.

In Fig. 7.4.3 our results are presented together with recent world direct detection data [1–13, 96]. To quantify the impact of uncertainties in the energy scale on the experimental limit, the calculation is performed using two different $\mathscr{L}_{eff}$ scalings between S1 and E$_{nr}$. The first $\mathscr{L}_{eff}$ is taken from the NEST [68, 69] model using the measured photon detection efficiency (PDE) of 10.5%. The second is the conservative $\mathscr{L}_{eff}$ used by XENON100 [96] but with the PandaX-I measured L_y^{122}. Below 10 GeV/c^2, the latter gives a more conservative limit. Note that our results show a nominally better limit below 6 GeV/c^2 than that from

LUX [10] due to LUX using an energy scale with zero light yield below 3 keV_{nr}, a very conservative approach compared to NEST or other phenomenological models. Our result is comparable in the high WIMP mass region to that of XENON100 with similar exposure but is significantly more constraining in the low-mass region, demonstrating the advantage of the low-energy threshold of the PandaX-I detector. At the 90% C.L., our results do not support the spin-independent WIMP interpretation of the previously reported signals from DAMA, CoGeNT, CRESST and CDMS II-Si [1–8]. In a wide WIMP mass region, our result confirms the power of the LXe dual-phase technique as one of the leading technologies to probe the theoretically-favored DM particles predicted in supersymmetric models.

CHAPTER VIII

Concluding Remarks

Pioneering work dating back to the 1950's gives the basis for the promising detector technology of today. The recent decades have seen rapid development of imaging and calorimetry detectors constructed with crystal and liquid noble targets, giving exciting prospects for dark matter discovery. Large experimental efforts to search for dark matter using the dual phase LXe technique were pioneered by the ZEPLIN [17] and XENON [9, 96] collaborations and likewise for crystal detectors with the CDMS [4, 11, 43] collaboration. Crystal detectors show particular promise in the low energy regime due to their low energy threshold. Background problems associated with the low mass, high surface area-to-mass ratio crystals have been alleviated with recent progress in production of large crystal sizes, reduction of surface contamination, and enhanced phonon detection schemes [11]. Liquid xenon detectors have enjoyed the ease with which liquid scintillator detectors can be economically scaled to both increase target mass and reduce background. LXe's resilient background rejection, three-dimensional position reconstruction, low energy threshold, and large target mass capabilities allowed the LXe experiments to achieve impressive progress in probing the WIMP-nucleon cross-section in just a recent short timespan.

8.1 Current Progress

The current limits in the standard WIMP mass range are placed by a number of experiments, nearly all excluding the positive detections seen at threshold in other detectors. XENON100

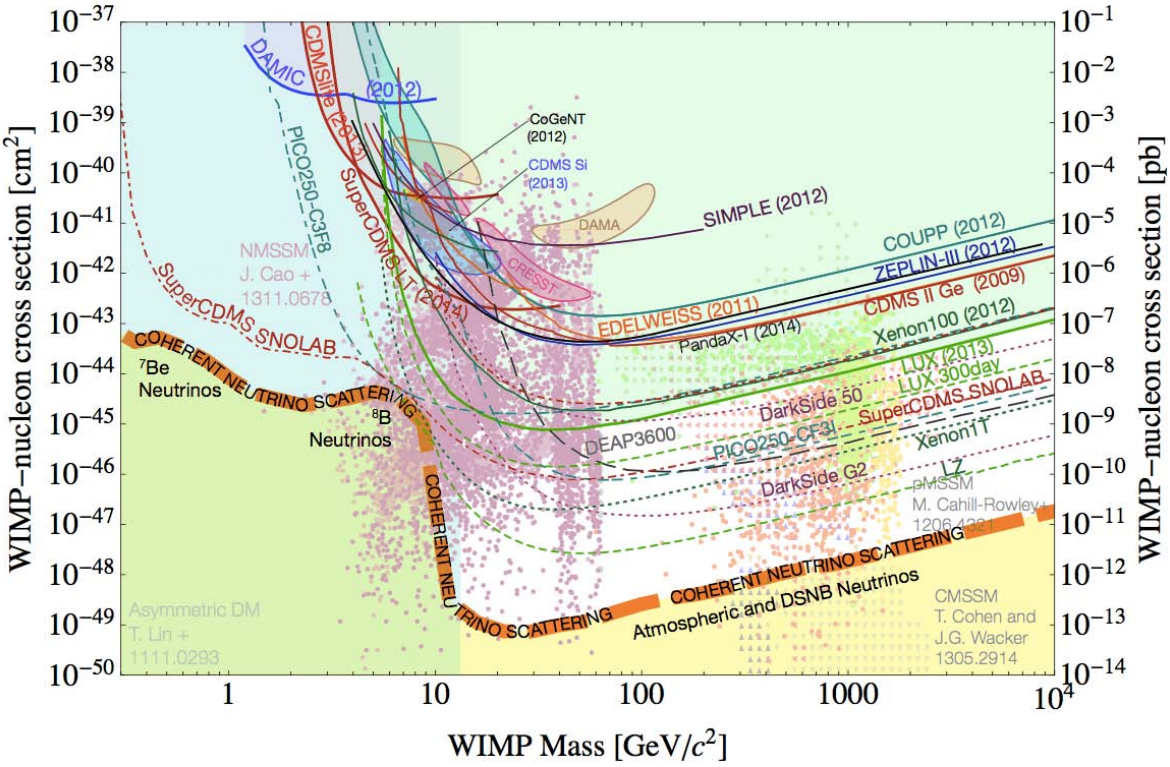

Figure 8.1.1: A collection of exclusions (open solid contours), detections (closed contours), future direct detection sensitivities (open dashed contours), and proposed WIMP models (points) which are of interest in the current search for WIMP dark matter. The claimed detections are in tension with a number of exclusions, casting doubt on the dark matter interpretation of the 'detection' data. A coherent scattering neutrino floor exists well below current limits with a large number of unprobed MSSM models [39–41, 98] in-between. Assembled from Ref. [52] with references therein.

collaboration's first result of 450 kg-days [96] and an improved background run with longer exposure at 7,600 kg-days [9], the LUX collaboration first results [10] after 10,000 kg-days, and SuperCDMS results [11] after 570 kg-days all have results consistent with the null hypothesis.

The PandaX experimental effort joins the DM search by utilizing a high light yield, dual phase LXe detector. PandaX-I is located in the favorable operating environment of China JinPing Laboratory which allows for a large experiment to be constructed quickly with minimal supporting systems (due to the lab's extensive earthen shielding). This allowed

PandaX-I to be developed, deployed, characterized [84], and to achieve science quality data in a short time span. The first PandaX-I result produced an impressive outcome [13] as the initial detector in the PandaX lineage. With 640 kg-days exposure, PandaX-I excludes the previous positive detections from Refs. [1–8] and further probes the WIMP-nucleon cross-section down to 9×10^{-43} cm^2 at 10 GeV/c^2 and 3.7×10^{-44} cm^2 at 49 GeV/c^2.

8.2 The Future

The current and next generation of direct detection experiments bring with them the promise of probing the contents of the WIMP parameter space of low cross-section (10^{-47} to 10^{-48} cm^2) in the MSSM mass regions of interest (10-1,000 GeV/c^2). PandaX looks forward to the result of the 80 live-day PandaX-I analysis (for which data taking has already completed) which will probe nearly an order of magnitude deeper into the WIMP-nucleon cross-section parameter space. Additionally, the scaling to 300 kg fiducial mass with PandaX-II has commenced with operation expected in early 2015.

Other operating dark matter programs will also be announcing results in the coming years. LUX will be reporting a year-scale dataset analysis in 2015-2016 and XENON100 is expected to report on a larger exposure and findings on annual modulation across their years-long datasets. SuperCDMS is expected to provide the world leading crystal detector results in the coming years as well, relying on large mass and a low energy threshold [99].

Ton and multi-ton LXe experiments are also on the near horizon with XENON1T [100] starting operation in late 2015, and both LZ [101] and PandaX-III expected in the next five years. Detection contours, current and future exclusion limits, and theoretical models in Fig. 8.1.1 give context to the landscape of direct detection in the future. In the figure, a coherent neutrino floor can be seen only a few orders of magnitude out of current technology's reach. This floor gives a soft lower bound on direct detection capabilities (experimenters can no longer count on near-zero background statistics). There is no need to despair as the bulk of the Higgs mediated MSSM candidates are between current detector limits and that very floor.

8.3 Final Words

With all of the effort in the search put forth thus far, the dark matter remains enigmatic. We have sound astrophysical and cosmological footing with well-motivated particle dark matter candidates, yet still no convincing direct detection evidence. However, WIMP hunting is entering an exciting age of accelerating sensitivity capabilities with promising regions of parameter space well within reach. For now, we can hone our skills, build bigger-better-cleaner, and hope that the detectors reach out their hairy arms and feel the Chelonian breeze. Now, what will we catch?

APPENDICES

APPENDIX A

Energy Reconstruction Scales

The units for energy reconstruction in a scintillation detector require careful attention to the type of energy deposition taking place. Reconstructed energies that assume the event is electromagnetic in nature are denoted with an *ee* subscript (meaning electron equivalent), such as keV_{ee}. This energy unit is the equivalent of average actual energy for ER events. Likewise, for events reconstructed as nuclear recoils the subscript *nr* is used, as in keV_{nr}. The two units are used either to draw attention to the type of deposition being discussed or to compare events with similar signal magnitudes (but different energy deposition types) on the same scale. As a concrete example, the measured signal (say, photoelectrons from photomultiplier tubes) is converted from signal units into energy units via

$$E_{recon}(S) = S\epsilon,$$

where S is the measured signal and ϵ is the empirical scaling between signal and energy (for the case of photomultipliers, ϵ has units of keV/photoelectron). Note that this is not the actual energy of the event since it cannot be known. The quantity E_{recon} is the energy reconstructed from averaged, measured quantities. In the direct detection world, the quantity of E_{recon} is not used, instead the quantity E_{ee} is utilized (and E_{nr} for nuclear recoils). The difference is only slight, with ϵ now having units of keV_{ee}/photoelectron to give

$$E_{ee}(S) = S\epsilon.$$

For NR events, the relation is slightly more complicated. Generally, the signal from nuclear recoil events are significantly suppressed when compared to electron recoil events of identical energy. This suppression is parametrized by an effective quenching Lindhard factor [67] $\mathscr{L}_{eff}$

$$S_{ee} = \frac{S_{nr}}{\mathscr{L}_{eff}},$$

where S_{ee} is the signal caused by an ER and S_{nr} is the signal caused by NR with identical energy depositions. Typical values for $\mathscr{L}_{eff}$ in liquid xenon are between 0.1-0.2 from low to high energy. The reduced signal for nuclear recoils is a result of the large number of atomic collisions that a recoiling nucleus undergoes during its slow to a stop in the detection medium. Electron recoils do not suffer this same fate so their energy is devoted to producing only electronic excitations, while the nuclear recoils have a large portion of recoil kinetic energy lost to heat. This quenching causes experimenters to use a new energy reconstruction scale utilizing the units of keV$_{nr}$, written as

$$E_{nr}(S) = \frac{S\epsilon}{\mathscr{L}_{eff}}.$$

One can see that a relation between both ER and NR energy reconstruction scales exists

$$E_{ee} = \mathscr{L}_{eff} E_{nr}.$$

However, notice the complementarity between the signal equation $S_{ee} = S_{nr}/\mathscr{L}_{eff}$ where the role of the Lindhard factor is inverted. With these tools, the task of energy reconstruction is reduced to identifying the type of interaction and applying the proper scaling equation. There is a slight modification to the equation when using a drift field in a dual phase LXe detector, as discussed below.

In the case of a dual phase liquid xenon detector, the signal traditionally used to reconstruct the energy is the light signal (S1) which for ER is significantly quenched under the application of a drift electric field. This field quenching is very different from the Lindhard quenching and originates from the dual channel nature of the detector as discussed in Sec. 3.5.9.1. Suffice to say that ER recoils have an S1 signal which is substantially reduced when a field is applied but NR recoils are barely quenched at all. The varied response must be corrected so that the above equations can be utilized.

The parameters which encapsulate the electric field quenching are S_e for ER and S_n NR events (see Fig. 3.5.3 for quenching values at various electric fields). The effect of this

quenching must be 'undone' when using energy reconstruction scales that are deduced at zero electric field (e.g. $\epsilon = \mathrm{L}_y^{122}$). This means the equations from above are adjusted to become

$$E_{ee}(S) = \frac{S\epsilon}{S_e},$$

$$E_{nr}(S) = \frac{S\epsilon}{S_n \mathscr{L}_{eff}},$$

$$E_{nr} = \frac{1}{\mathscr{L}_{eff}} \frac{S_e}{S_n} E_{ee},$$

where ϵ is the keV_{ee}/signal scaling at zero electric field. These relations can then be used to fully reconstruct the quenched signal emerging from a dual phase detector into an energy representative of the underlying interaction. The above definitions allow one to convert between the two types of deposition, allowing meaningful signal comparison on the S1 energy reconstruction scale.

APPENDIX B

PandaX-I Contribution

I have worked on several aspects of the PandaX-I effort as a graduate student, including simulation, analysis, and hardware projects. My contribution is only a small part of the many man-hours contributed to the design, construction, and implementation of PandaX-I by a dedicated group of professors, research scientists, postdocs, graduate students, undergraduates, engineers, and technicians. I list the projects in which I was directly involved.

Simulation, calculation, and analysis work was spread across several areas in PandaX-I. I worked on early electromagnetic background simulations with GEANT4 with Xiang Liu and electric field simulations which investigated new field shaping ring configurations and grid design in cylindrical geometry. I developed a PMT gain balancing technique in commissioning Run3 with the absence of an LED calibration source and later worked with Mengjiao Xiao on absolute PMT gain calibration in runs with LED capability. I worked to identify the inelastic calibration peaks in the neutron calibration for use in light yield and uniformity corrections and, with Xun Chen and Shaoli, I worked on shaping the data structures, data handling software, and overall analysis design and implementation in ROOT. With Kaixuan Ni, Qing Lin, Xiang Xiao I worked on calculating spin-independent WIMP-nucleon sensitivity projections for PandaX-I, II, and III. With Mengjiao Xiao and Andi Tan, we identified calibration schemes which provide effective detector characterization. Simulations of detector response of PandaX-I (and LXe detectors in general) with the NEST library addition to GEANT4 were carried out with assistance from Fei Gao.

I spent much time on hardware and operation of PandaX-I on-site at CJPL. I operated detector subsystems (cryogenics, TPC, DAQ, calibration, slow control, PMTs) during commissioning and science runs with Jianglai Liu, Kaixuan Ni, Xiang Liu, Zhao Li, Mengjiao Xiao, Xiang Xiao, Andi Tan, Shaoli Li, XiangXiang Ren, and others. We spent several months together during 2013-2014 at CJPL in the process of achieving full operation of

PandaX-I. During commissioning runs I worked alongside Mengjiao Xiao and XiangXiang Ren to troubleshoot, reconfigure, and operate the PMTs and signal pathways to the DAQ. Many fun times were had with Michael Schubnell extending the capabilities of the slow control during runs as well, with correlated parameter plotting, remote gas valve control, radon detector logging, and more added. With Xiang Xiao, we spent intense mid-run days tuning the PID setting of the Lakeshore to establish the observed tight temperature control. With Zhao Li, Andi Tan, Mengjiao Xiao, and Xiang Xiao, we worked on several occasions to optimize the large scale xenon liquefaction and filling process. With Andi Tan, Xiang Xiao, and others from the cryogenics group, we analyzed gas problems in the commissioning runs and optimized detector thermodynamic parameters. I debugged electronic noise originating from external feedthrough cathode discharge and reduced noise on the PMT cabling with Mengjiao Xiao and Guodong Guo. With Kaixuan Ni and Xiang Xiao, we established safe limits and procedures for effectively operating the TPC high voltage system and witnessed both the first S1 and S2 signals in PandaX-I.

Much work was conducted off-site as well to garner the knowledge necessary to operate LXe detectors. At both SJTU (with Jianglai Liu) and Michigan, I identified helium contamination of xenon through purity assays. With Wolfgang Lorenzon, Greg Tarle, Tim Chupp, Tom Schwarz, Michael Schubnell, Richard Raymond, Curtis Weaverdyck, Jon Ameel, and a dozen undergraduates, we developed a high light yield, position sensitive, small-scale dual phase detector. I lead the efforts of the MiX program at Michigan and, with MiX, we were able to characterize the PMTs used in PandaX-I and perform base testing. Additionally, we modified the PMT bases and designed custom TPMT voltage dividers, an analog time-over-threshold trigger circuit, and completed extensive high voltage feedthrough design. We also operated the detector in a topology identical to PandaX-I. The largest impact felt from MiX was the deep understanding it imbued in us all of just how intricate the operation of a dual-phase LXe TPC can be, and this knowledge we could contribute to PandaX-I. We developed techniques to troubleshoot the operation of LXe detector systems and explored the feasible thermodynamic operating range of LXe with PMTs. Extensive in-house development, testing, and deployment of the slow control system was done almost entirely by Michael Schubnell, but of which I did have a small part. Using this experience, we could help establish best practices for LXe detector operation and actively contribute to LXe subsystem design and operation on PandaX-I.

BIBLIOGRAPHY

Bibliography

[1] C.E. Aalseth et al. Results from a Search for Light-Mass Dark Matter with a P-type Point Contact Germanium Detector. *Phys.Rev.Lett.*, 106:131301, 2011.

[2] C.E. Aalseth et al. CoGeNT: A Search for Low-Mass Dark Matter using p-type Point Contact Germanium Detectors. *Phys.Rev.*, D88(1):012002, 2013.

[3] C.E. Aalseth, P.S. Barbeau, J. Colaresi, J. Diaz Leon, J.E. Fast, et al. Maximum Likelihood Signal Extraction Method Applied to 3.4 years of CoGeNT Data. 2014.

[4] R. Agnese et al. Silicon Detector Dark Matter Results from the Final Exposure of CDMS II. *Phys.Rev.Lett.*, 111:251301, 2013.

[5] R. Bernabei et al. First results from DAMA/LIBRA and the combined results with DAMA/NaI. *Eur.Phys.J.*, C56:333–355, 2008.

[6] R. Bernabei et al. New results from DAMA/LIBRA. *Eur.Phys.J.*, C67:39–49, 2010.

[7] R. Bernabei, P. Belli, F. Cappella, V. Caracciolo, S. Castellano, et al. Final model independent result of DAMA/LIBRA-phase1. *Eur.Phys.J.*, C73(12):2648, 2013.

[8] G. Angloher, M. Bauer, I. Bavykina, A. Bento, C. Bucci, et al. Results from 730 kg days of the CRESST-II Dark Matter Search. *Eur.Phys.J.*, C72:1971, 2012.

[9] E. Aprile et al. Dark Matter Results from 225 Live Days of XENON100 Data. *Phys.Rev.Lett.*, 109:181301, 2012.

[10] D.S. Akerib et al. First results from the LUX dark matter experiment at the Sanford Underground Research Facility. *Phys.Rev.Lett.*, 112(9):091303, 2014.

[11] R. Agnese et al. Search for Low-Mass Weakly Interacting Massive Particles Using Voltage-Assisted Calorimetric Ionization Detection in the SuperCDMS Experiment. *Phys.Rev.Lett.*, 112(4):041302, 2014.

[12] Q. Yue et al. Limits on light WIMPs from the CDEX-1 experiment with a p-type point-contact germanium detector at the China Jingping Underground Laboratory. *Phys.Rev.*, D90(9):091701, 2014.

[13] Mengjiao Xiao et al. First dark matter search results from the PandaX-I experiment. *Sci.China Phys.Mech.Astron.*, 57:2024–2030, 2014.

[14] Gianfranco Bertone, Dan Hooper, and Joseph Silk. Particle dark matter: Evidence, candidates and constraints. *Phys.Rept.*, 405:279–390, 2005.

[15] Gianfranco Bertone, editor. *Particle Dark Matter*. Cambridge University Press, 2010. Cambridge Books Online.

[16] S.J. Asztalos et al. A SQUID-based microwave cavity search for dark-matter axions. *Phys.Rev.Lett.*, 104:041301, 2010.

[17] Henrique Araujo. Results from the second science run of ZEPLIN-III. *AIP Conf.Proc.*, 1441:506–508, 2012.

[18] N. Suzuki et al. The Hubble Space Telescope Cluster Supernova Survey. V. Improving the Dark-energy Constraints above z $>$ 1 and Building an Early-type-hosted Supernova Sample. *Ap.J.*, 746:85, February 2012.

[19] F. Zwicky. Die Rotverschiebung von extragalaktischen Nebeln. *Helv.Phys.Acta*, 6:110–127, 1933.

[20] V.C. Rubin, N. Thonnard, and Jr. Ford, W.K. Rotational properties of 21 SC galaxies with a large range of luminosities and radii, from NGC 4605 /R = 4kpc/ to UGC 2885 /R = 122 kpc/. *Ap.J.*, 238:471, 1980.

[21] K.G. Begeman, A.H. Broeils, and R.H. Sanders. Extended rotation curves of spiral galaxies: Dark haloes and modified dynamics. *Mon.Not.Roy.Astron.Soc.*, 249:523, 1991.

[22] Max Tegmark et al. Cosmological parameters from SDSS and WMAP. *Phys.Rev.*, D69:103501, 2004.

[23] P.A.R. Ade et al. Planck 2013 results. I. Overview of products and scientific results. *Astron.Astrophys.*, 571:A1, 2014.

[24] J. Dunkley et al. Five-Year Wilkinson Microwave Anisotropy Probe (WMAP) Observations: Likelihoods and Parameters from the WMAP data. *Astrophys.J.Suppl.*, 180:306–329, 2009.

[25] E. Komatsu et al. Five-Year Wilkinson Microwave Anisotropy Probe (WMAP) Observations: Cosmological Interpretation. *Astrophys.J.Suppl.*, 180:330–376, 2009.

[26] M. Markevitch, A.H. Gonzalez, L. David, A. Vikhlinin, S. Murray, et al. A Textbook example of a bow shock in the merging galaxy cluster 1E0657-56. *Astrophys.J.*, 567:L27, 2002.

[27] Volker Springel, Simon D.M. White, Adrian Jenkins, Carlos S. Frenk, Naoki Yoshida, et al. Simulating the joint evolution of quasars, galaxies and their large-scale distribution. *Nature*, 435:629–636, 2005.

[28] Barbara Ryden. *Introduction to Cosmology*. Benjamin Cummings, October 2002.

[29] J. P. Ostriker, P. J. E. Peebles, and A. Yahil. The size and mass of galaxies, and the mass of the universe. *Ap.J.*, 193:L1–L4, October 1974.

[30] Jonathan L. Sievers et al. The Atacama Cosmology Telescope: Cosmological parameters from three seasons of data. *JCAP*, 1310:060, 2013.

[31] R. Keisler, C.L. Reichardt, K.A. Aird, B.A. Benson, L.E. Bleem, et al. A Measurement of the Damping Tail of the Cosmic Microwave Background Power Spectrum with the South Pole Telescope. *Astrophys.J.*, 743:28, 2011.

[32] NASA, N. Benitez, T. Broadhurst, H. Ford, M. Clampin, G. Hartig, G. Illingworth, ACS Science Team, and ESA. Galaxy Abell 1689's "Gravitational Lens" Magnifies Light of Distant Galaxies, 2003.
[33] Maxim Markevitch. Chandra observation of the most interesting cluster in the universe. *ESA Spec.Publ.*, 604:723, 2006.
[34] Gerard Jungman, Marc Kamionkowski, and Kim Griest. Supersymmetric dark matter. *Phys.Rept.*, 267:195–373, 1996.
[35] R.D. Peccei and Helen R. Quinn. CP Conservation in the Presence of Instantons. *Phys.Rev.Lett.*, 38:1440–1443, 1977.
[36] Jonathan L. Feng. Dark Matter Candidates from Particle Physics and Methods of Detection. *Ann.Rev.Astron.Astrophys.*, 48:495–545, 2010.
[37] Stephen P. Martin. A Supersymmetry primer. *Adv.Ser.Direct.High Energy Phys.*, 21:1–153, 2010.
[38] Mark Goodman and Edward Witten. Detectability of certain dark-matter candidates. *Phys. Rev. D*, 31:3059–3063, Jun 1985.
[39] Timothy Cohen and Jay G. Wacker. Here be Dragons: The Unexplored Continents of the CMSSM. *JHEP*, 1309:061, 2013.
[40] Junjie Cao, Chengcheng Han, Lei Wu, Peiwen Wu, and Jin Min Yang. A light SUSY dark matter after CDMS-II, LUX and LHC Higgs data. *JHEP*, 1405:056, 2014.
[41] Matthew W. Cahill-Rowley, JoAnne L. Hewett, Stefan Hoeche, Ahmed Ismail, and Thomas G. Rizzo. The New Look pMSSM with Neutralino and Gravitino LSPs. *Eur.Phys.J.*, C72:2156, 2012.
[42] J.L. Feng, S. Ritz, J.J. Beatty, J. Buckley, D.F. Cowen, et al. Planning the Future of U.S. Particle Physics (Snowmass 2013): Chapter 4: Cosmic Frontier. 2014.
[43] R.J. Gaitskell. Direct detection of dark matter. *Ann.Rev.Nucl.Part.Sci.*, 54:315–359, 2004.
[44] Kaixuan Ni. *Development of a Liquid Xenon Time Projection Chamber for the XENON Dark Matter Search*. PhD thesis, Columbia University, 2006.
[45] Georges Aad et al. Search for dark matter in events with heavy quarks and missing transverse momentum in *pp* collisions with the ATLAS detector. 2014.
[46] Kathryn Zurek. Hunt For Dark Matter: Direct, Indirect and LHC Complementarity. In *Michigan Dark Matter Workshop*, 2014.
[47] Jalal Abdallah, Adi Ashkenazi, Antonio Boveia, Giorgio Busoni, Andrea De Simone, et al. Simplified Models for Dark Matter and Missing Energy Searches at the LHC. 2014.
[48] F. Aharonian et al. Observations of the Sagittarius Dwarf galaxy by the H.E.S.S. experiment and search for a Dark Matter signal. *Astropart.Phys.*, 29:55–62, 2008.
[49] M. Doro et al. Dark Matter and Fundamental Physics with the Cherenkov Telescope Array. *Astropart.Phys.*, 43:189–214, 2013.

[50] Torsten Bringmann, Xiaoyuan Huang, Alejandro Ibarra, Stefan Vogl, and Christoph Weniger. Fermi LAT Search for Internal Bremsstrahlung Signatures from Dark Matter Annihilation. *JCAP*, 1207:054, 2012.

[51] S.P. Ahlen and G. Tarle. Secondary Production as the Origin for the Cosmic Ray Positron Excess. 2014.

[52] Enectali Figueroa-Feliciano. Upcoming CDMS searches. In *Sackler Debates, Harvard*, 2014.

[53] J.D. Lewin and P.F. Smith. Review of mathematics, numerical factors, and corrections for dark matter experiments based on elastic nuclear recoil. *Astropart.Phys.*, 6:87–112, 1996.

[54] R.W. Schnee. Introduction to dark matter experiments. 2011.

[55] Christopher Savage, Katherine Freese, and Paolo Gondolo. Annual Modulation of Dark Matter in the Presence of Streams. *Phys.Rev.*, D74:043531, 2006.

[56] Michael Kuhlen, Neal Weiner, Jurg Diemand, Piero Madau, Ben Moore, et al. Dark Matter Direct Detection with Non-Maxwellian Velocity Structure. *JCAP*, 1002:030, 2010.

[57] A.K. Drukier, K. Freese, and D.N. Spergel. Detecting Cold Dark Matter Candidates. *Phys.Rev.*, D33:3495–3508, 1986.

[58] U. Fano. Ionization Yield of Radiations. 2. The Fluctuations of the Number of Ions. *Phys.Rev.*, 72:26–29, 1947.

[59] Gary J. Feldman and Robert D. Cousins. A Unified approach to the classical statistical analysis of small signals. *Phys.Rev.*, D57:3873–3889, 1998.

[60] E. Aprile and T. Doke. Liquid Xenon Detectors for Particle Physics and Astrophysics. *Rev.Mod.Phys.*, 82:2053–2097, 2010.

[61] J. Seguinot, T. Ypsilantis, G. Passardi, and J. Tischhauser. Liquid xenon ionization and scintillation: Studies for a totally active vector electromagnetic calorimeter. *Nucl.Instrum.Meth.*, A323:583–600, 1992.

[62] K. Abe, K. Hieda, K. Hiraide, S. Hirano, Y. Kishimoto, et al. XMASS detector. *Nucl.Instrum.Meth.*, A716:78–85, 2013.

[63] G.J. Alner et al. First limits on nuclear recoil events from the ZEPLIN I galactic dark matter detector. *Astropart.Phys.*, 23:444–462, 2005.

[64] W. Shockley. Hot Electrons in Germanium and Ohm's Law. *Bell System Tech. J.*, 30:990, 1951.

[65] L. Miller, S. Howe, and W. Spear. Charge transport in solid and liquid ar, kr, and xe. *Phys. Rev.*, 166:871–878, Feb 1968.

[66] G. Bakale et al. Effects of an Electric Field on Electron Attachment to SF_6, N_2O and O_2 in Liquid Argon and Xenon. *J.Phys.Chem.*, 80:2556, 1976.

[67] J. Lindhard, M. Scharff, and H.E. Schiott. Range concepts and heavy ion ranges. *Mat. Fys. Medd. Dan. Vid. Selsk.*, 33(14):1–42, 1963.

[68] Matthew Szydagis, Adalyn Fyhrie, Daniel Thorngren, and Mani Tripathi. Enhancement of NEST Capabilities for Simulating Low-Energy Recoils in Liquid Xenon. *JINST*, 8:C10003, 2013.

[69] M. Szydagis, N. Barry, K. Kazkaz, J. Mock, D. Stolp, et al. NEST: A Comprehensive Model for Scintillation Yield in Liquid Xenon. *JINST*, 6:P10002, 2011.

[70] Eric Dahl. *The Physics of Background Discrimination in Liquid Xenon, and First Results from Xenon10 in the Hunt for WIMP Dark Matter*. PhD thesis, Princeton University, 2009.

[71] A. Hitachi. Properties of liquid xenon scintillation for dark matter searches. *Astropart.Phys.*, 24:247–256, 2005.

[72] Tadayoshi Doke, Akira Hitachi, Jun Kikuchi, Kimiaki Masuda, Hiroyuki Okada, and Eido Shibamura. Absolute scintillation yields in liquid argon and xenon for various particles. *Japanese Journal of Applied Physics*, 41(3R):1538, 2002.

[73] K. Ozone. *Liquid Xenon Scintillation Detector for the New $\mu \to e\gamma$ Search Experiment*. PhD thesis, University of Tokyo, Japan, 2005.

[74] S. Kubota, A. Nakamoto, T. Takahashi, T. Hamada, E. Shibamura, et al. Recombination luminescence in liquid argon and in liquid xenon. *Phys.Rev.*, B17(6):2762–2765, 1978.

[75] E. Conti et al. Correlated fluctuations between luminescence and ionization in liquid xenon. *Phys.Rev.*, B68:054201, 2003.

[76] G.D. Alkhazov. Ionization fluctuations in gases. *Sov.Phys.Tech.Phys.*, 16:1540, 1972.

[77] H. Ichinose et al. *Nucl.Instrum.Methods*, A332:216, 1992.

[78] G.F. Knoll. *Radiation Detection and Measurement*. Wiley, 2000.

[79] M. Yamashita, T. Doke, K. Kawasaki, J. Kikuchi, and S. Suzuki. Scintillation response of liquid Xe surrounded by PTFE reflector for gamma rays. *Nucl.Instrum.Meth.*, A535(3):692–698, 2004.

[80] H. Gong, K.L. Giboni, X. Ji, A. Tan, and L. Zhao. The Cryogenic System for the Panda-X Dark Matter Search Experiment. *JINST*, 8:P01002, 2013.

[81] S. Agostinelli et al. GEANT4: A Simulation toolkit. *Nucl.Instrum.Meth.*, A506:250–303, 2003.

[82] John Allison, K. Amako, J. Apostolakis, H. Araujo, P.A. Dubois, et al. Geant4 developments and applications. *IEEE Trans.Nucl.Sci.*, 53:270, 2006.

[83] R. Brun and F. Rademakers. ROOT: An object oriented data analysis framework. *Nucl.Instrum.Meth.*, A389:81–86, 1997.

[84] XiGuang Cao, Xun Chen, YunHua Chen, XiangYi Cui, DeQing Fang, et al. PandaX: A Liquid Xenon Dark Matter Experiment at CJPL. *Sci.China Phys.Mech.Astron.*, 57:1476–1494, 2014.

[85] Jie Hu, Hao-Wei Gong, Qing Lin, Kai-Xuan Ni, An-Di Tan, et al. Development of the Liquid Level Meters for the PandaX Dark Matter Detector. *Chin.Phys.*, C38(5):056002, 2014.

[86] Ko Abe et al. The XMASS experiment. *J.Phys.Conf.Ser.*, 120:042022, 2008.
[87] Qing Lin, Yuehuan Wei, Jie Bao, Jie Hu, X. Li, et al. High Resolution Gamma Ray Detection in a Dual Phase Xenon Time Projection Chamber. *JINST*, 9:P04014, 2014.
[88] R.J. Gaitskell, P.D. Barnes, A. Da Silva, B. Sadoulet, and T. Shutt. The statistics of background rejection in direct detection experiments for dark matter. *Nucl.Phys.Proc.Suppl.*, 51B:279–283, 1996.
[89] P. Antonioli, C. Ghetti, E.V. Korolkova, V.A. Kudryavtsev, and G. Sartorelli. A Three-dimensional code for muon propagation through the rock: Music. *Astropart.Phys.*, 7:357–368, 1997.
[90] D.G. Madland, E.D. Arthur, G.P. Estes, J.E. Stewart, M. Bozoian, R.T. Perry, T.A. Parish, T.H. Brown, T.R. England, W.B. Wilson, and et al. *SOURCES 4A: A Code for Calculating (alpha,n), Spontaneous Fission, and Delayed Neutron Sources and Spectra*. Sep 1999.
[91] S. Nissen. Implementation of a Fast Artificial Neural Network Library (fann). Technical report, Department of Computer Science University of Copenhagen (DIKU), 2003. http://fann.sf.net.
[92] E. Aprile, C.E. Dahl, L. DeViveiros, R. Gaitskell, K.L. Giboni, et al. Simultaneous measurement of ionization and scintillation from nuclear recoils in liquid xenon as target for a dark matter experiment. *Phys.Rev.Lett.*, 97:081302, 2006.
[93] T. Shutt, Carl E. Dahl, J. Kwong, A. Bolozdynya, and P. Brusov. Performance and Fundamental Processes at Low Energy in a Two-Phase Liquid Xenon Dark Matter Detector. *Nucl.Instrum.Meth.*, A579:451–453, 2007.
[94] K. Ni, E. Aprile, K.L. Giboni, P. Majewski, and M. Yamashita. Gamma Ray Spectroscopy with Scintillation Light in Liquid Xenon. *JINST*, 1:P09004, 2006.
[95] Peter Sorensen and Carl Eric Dahl. Nuclear recoil energy scale in liquid xenon with application to the direct detection of dark matter. *Phys.Rev.*, D83:063501, 2011.
[96] E. Aprile et al. First Dark Matter Results from the XENON100 Experiment. *Phys.Rev.Lett.*, 105:131302, 2010.
[97] Martin C. Smith, G.R. Ruchti, A. Helmi, R.F.G. Wyse, J.P. Fulbright, et al. The RAVE Survey: Constraining the Local Galactic Escape Speed. *Mon.Not.Roy.Astron.Soc.*, 379:755–772, 2007.
[98] Tongyan Lin, Hai-Bo Yu, and Kathryn M. Zurek. On Symmetric and Asymmetric Light Dark Matter. *Phys.Rev.*, D85:063503, 2012.
[99] Wolfgang Rau. CDMS and SuperCDMS. *J.Phys.Conf.Ser.*, 375:012005, 2012.
[100] Elena Aprile. The XENON1T Dark Matter Search Experiment. *Springer Proc.Phys.*, C12-02-22:93–96, 2013.
[101] D.C. Malling, D.S. Akerib, H.M. Araujo, X. Bai, S. Bedikian, et al. After LUX: The LZ Program. 2011.